Origin of porewater sulfate in an Ordovician aquiclude of the Michigan Basin, Ontario: Insights from stable isotopes.

Jing Zhang

Thesis submitted to the

Faculty of Graduate and Postdoctoral Studies

In partial fulfillment of the requirements

For the MSc degree in the Chemical and Environmental Toxicology Program

Department of Earth Sciences

Faculty of Science

University of Ottawa

Abstract

Low-permeability Ordovician shale and limestone formations of the Michigan Basin are a target of interest for a deep geological repository for the long-term isolation of low and intermediate-level radioactive waste. Porewater studies contribute to an understanding of the age and evolution of paleofluids as part of ongoing research. Sulfur and oxygen isotope data presented here add to the characterization of these formations. For this work, a method was developed and used to extract porewater sulfate from low permeability rocks for the analysis of sulfate concentration and its $\delta^{34}S$ and $\delta^{18}O$ values, using an elemental analyzer interfaced with an isotope ratio mass spectrometer (EA-IRMS). Porewater sulfate concentrations were very low, varying from 0.02 to 228.88 mmol/ kgw. Values for $\delta^{34}S$ were all near or below those for Ordovician seawater. The earlier work examined the $\delta^{34}S$ and the morphology of framboidal pyrite in the Ordovician formations provides strong evidence for diagenetic sulfate reduction (Jautzy et al. in prep.). The lack of enrichment for $\delta^{34}S$ and $\delta^{18}O$ in porewater sulfate suggests that diagenetic sulfate reduction was quantitative and that the porewater sulfate measured in these samples is not residual sulfate remaining from that time. The distribution of sulfur isotope values between that of Silurian seawater and those of the framboidal pyrite suggests an origin from the infiltration of Silurian brines with contributions from pyrite oxidation. The $\delta^{18}O$ values are consistent with this, showing mixtures between Silurian seawater sulfate and sulfide oxidation without the involvement of atmospheric oxygen. This evidence for anoxic sulfide oxidation indicates that inadvertent exposure to atmospheric O_2 during porewater leaching in the laboratory is unlikely and that *in-situ* oxidation involving electron acceptors with lower electromotive potential took place, possibly over geological time. The combination of sulfate mass and the stable isotopes of porewater sulfate, along with the presence of Fe (III) and Mn

(IV) bearing minerals indicate potential evidence of *in-situ* sulfide oxidation in one third of twenty-six core samples. The relative timing of events is not clear as to whether sulfide oxidation could have occurred during the Ordovician and/or after the infiltration of evaporated Silurian seawater into the Ordovician strata. This study adds a new understanding of the redox evolution within this sedimentary system with implications for contaminant transport.

\

Acknowledgements

I would like to extend my gratitude to Dr. Ian D. Clark and Dr. Josué J. Jautzy for their continued patience, guidance and expertise throughout this research project. My thanks to examiners Dr. Tom Al and Dr. Tim Patterson for lending their expertise. I would also like to thank the members of the Ján Veizer Stable Isotope Laboratory at the University of Ottawa for being flexible and providing exceptional quality data. Additionally, I would like to thank Dr. Duane Petts for his expertise as he guided me through the petrographical section of my project. My thesis would not have been possible without the valuable effort and support of everyone.

Table of Contents

List of Tables

List of Figures

List of Key Acronyms

BSR: Bacterial sulfate reduction

DGR: Deep geological repository

DI: Deionized

EA-IRMS: Elemental analyzer- isotope ratio mass spectrometer

mBGS: Meters below ground surface

MP-AES: Microwave Plasma-Atomic Emission Spectrometer

SIMS: Secondary ion mass spectrometry

SRB: Sulfate reducing bacteria

STD: Standard deviation

VCDT: Vienna-Canyon Diablo Troilite

VSMOW: Vienna Standard Mean Ocean Water

1. Introduction

Sulfur is essential to all living organisms as it is metabolized by microorganisms, plants, and animals for the construction of biological molecules (Fike et al., 2015). Moreover, it is also a major element present in seawater and marine sediments (Clark and Fritz, 1997). Sulfur isotopes along with oxygen isotopes have been used to obtain insights into the evolutionary history of the sulfur cycle on Earth (Deusner et al., 2014) was recorded by marine sedimentary rocks. In such sedimentary formations, the $\delta^{34}S$ and $\delta^{18}O$ signatures of the porewater sulfate, can help us understand the origin and redox evolution of sulfate and sulfide minerals.

Deep geological repositories (DGR) are regarded as the preferred method for the long-term storage of long-lived nuclear waste (International Atomic Energy Agency, 1990). Canada's solution for long-term sequestration of low and intermediate level nuclear waste focuses on the ancient low-permeability sedimentary formations on the eastern flank of the Michigan Basin and located in the municipality of Kincardine, Ontario. This site has been extensively characterized for over ten years in order to understand its ability to confine low and intermediate level nuclear waste. The mobility of the waste within these layers and its circulation to the surface depend on the hydrogeology of the area, the local geology, geochemistry and geochemical composition of porefluids, it has been extensively characterized by many studies and technical reports published over the years (Raven et al., 2011; Clark et al., 2013, 2015; Al et al., 2015; Murseli et al. 2017). More specifically, the Ordovician aquiclude located 680 m below the surface within the argillaceous limestone has been chosen to host the proposed DGR due to the uniformity of the bedrocks, high salinity (Clark et al., 2013) and fluid transport is diffusion dominated with a diffusion coefficient of $10^{-12}m^2/s$ or lower (Al et al., 2015). Moreover, a zone of biogenic methanogenesis has been identified within the sequence of barrier shale formations, which has

been the focus of research to identify the range of redox reactions and implications for transport and waste isolation (Jautzy et al., 2018).

The aim of this research is to gain a better understanding of the evolution of sulfur within this sedimentary system in order to further characterize the confinement in these layers in terms of the sulfur system. This is done by examining the sulfur and oxygen isotopes of the porewater sulfate to identify the possible evidence for microbial sulfate reduction and sulfide oxidation in these layers. In the context of the sulfur cycle, this will help conceptualize the timing of the sulfur cycle and define its role within the geochemical history of the sedimentary system. In addition, in an attempt to identify whether these reactions are abiotic or biotic, this may provide important information regarding potential future implications on the DGR.

This study also provides a reliable method for porewater extraction and isotopic analysis for low permeability rocks where low sulfate concentrations remains a challenge. There are many methods established for porewater extraction including *in-situ* direct sampling, diffusive sampling, squeezing and many others (Koroleva et al., 2009; Celejewski et al., 2014). *In-situ* sampling along with diffusive-exchange method has been utilized in several other sites in the world with clays and shales. However, in those systems, the reported porewater salinity was much lower than modern seawater previously examined by Koroleva et al., (2009), and even lower than the salinity measured in the Ordovician porewaters in the Michigan Basin at the Bruce site (i.e., ten times more saline than modern seawater) (Clark et al., 2013). The high salinity makes it challenging for diffusive sampling, as ionic strength of the porewater is very high. Moreover, due to the low porosity and permeability of this Paleozoic sequence, squeezing tests are not possible for these samples (Koroleva et al., 2009; Celejewski et al., 2014). Finally, during the crush-and-leach technique, it is possible to create chemical artefacts created as a result

of mineral dissolution and precipitation reactions during alteration of chemical composition (Celejewski et al., 2014). While, crush-and leach might have some limitations, it remains as the most favored method for porewater extraction from previous studies (Koroleva et al., 2009; Hobbs et al., 2011; Raven et al., 2011; Clark et al., 2013; Murseli et al., 2017).

In this study, a full anoxic crush-and-leach method is adapted and performed in order to mitigate and monitor possible chemical artefacts. The anoxic characteristics of this method prevents the oxidation of sulfide minerals, which contribute to the elevated porewater sulfate concentrations and the isotopic composition of porewater sulfate. We monitored the principal anions and cations in the leachate to evaluate possible mineral dissolution. Finally, the isotopic abundances were acquired on a large-capacity elemental analyzer-isotope ratio mass spectrometer (EA-IRMS) allowing combustion of the precipitated $BaSO_4$ along with the filter to maximize sample transfer and yields to adapt to the low porewater sulfate concentration present in these formations.

2. Literature Review

2.1 *Geology of the Michigan Basin*

The Ordovician shale and limestone within the Michigan Basin has been selected as the host rock for potential radioactive waste isolation due to its tectonic stability, horizontal predictability, low-permeability, and low economic interest within the local area (International Atomic Energy Agency, 2009; Raven et al., 2011). The strategic sedimentary sequence located below the Bruce Nuclear site is summarized in Figure 2.1, which consists of Cambrian sandstones to Devonian dolostones. The targeted area of interest is situated within the Ordovician formation, which are mainly composed of argillaceous limestone and shale from a depth of approximately 450 to 850 m below ground surface (mBGS). More specifically, the

proposed DGR is located at around 680 mBGS within the argillaceous limestones of the Ordovician Cobourg Formation. The dominant fluid transport within the shales and limestones is diffusion (Al et al., 2015) and the groundwater system present in the shales and limestone is ancient, saline, stagnant, and stable (Raven et al., 2011), which is essential for waste isolation (International Atomic Energy Agency, 1990).

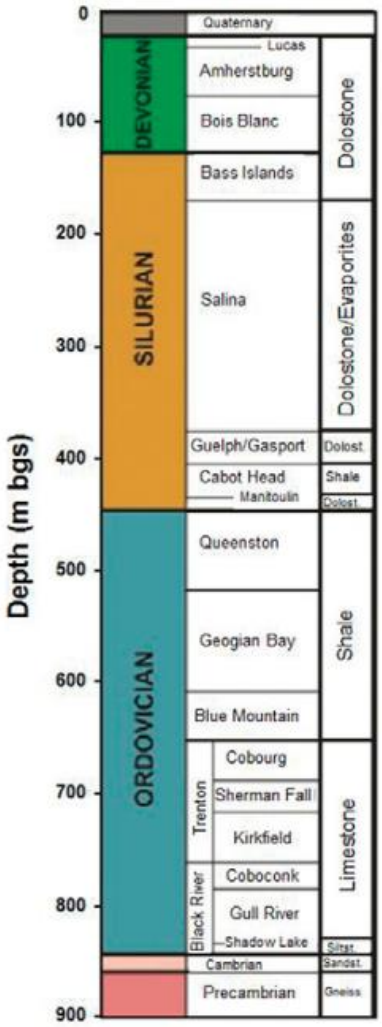

Figure 2. 1: The sedimentary sequence of the Michigan Basin
Modified from (Clark et al., 2013), the sedimentary sequence below ground consisting of argillaceous limestones and shale.

Seven boreholes (DGR-1-6, 8) were drilled to recover 75 mm-diameter cores. DGR-5 and 6 were drilled at an incline, therefore requiring depth correction when interpreting true depth.

Porewater characterization experiments determined the wet bulk density to be 2.65 and 2.69 g/cm^3 for Ordovician shales and Ordovician limestones (Raven et al., 2011). The brine saturation ranges from 60 to 100% in the Ordovician shales and limestone with the concentrations of Cl^- ranging from 4000 to 6000 mmol/kgw in Figure 2.2 (Raven et al., 2011; Clark et al., 2013). In comparison, modern seawater is about 693.9 mmol/kgw in terms of salinity (Cullum et al., 2016).

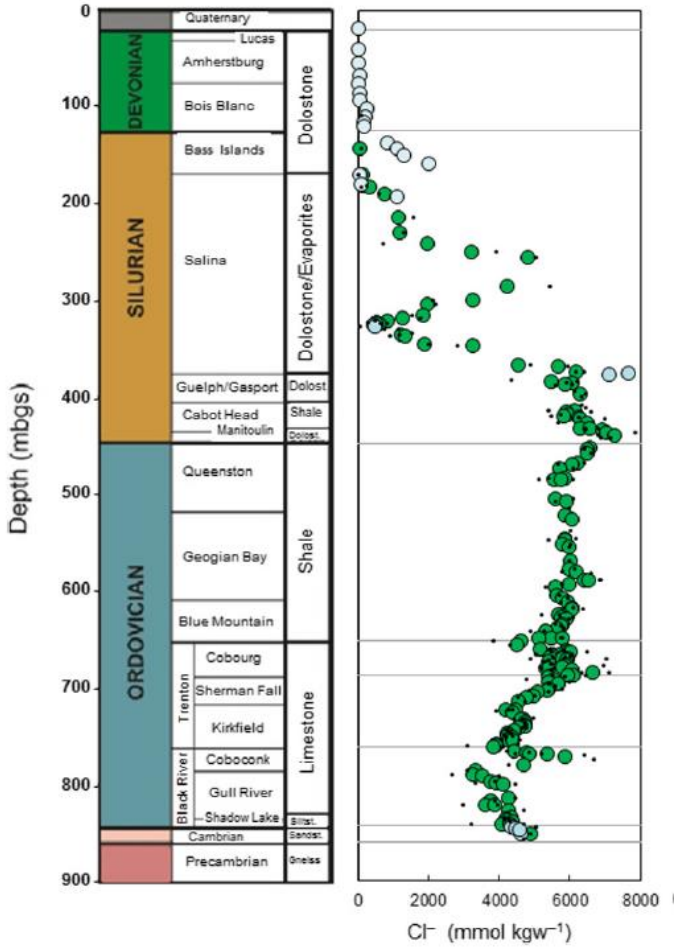

Figure 2. 2: Chloride concentration profile at the Bruce Site
Modified from (Clark et al., 2013). The light blue circles represent groundwater chloride concentration. Green circles are three point running averages of chloride concentration in porewaters.

Previous diffusion experiments used numerical simulations to determine the D_e to be 10^{-12}m^2/s or lower in these layers (Al et al., 2015), indicating the principle solute transport process

is dominated by diffusion. In addition, porosity is reported to be 0.084 (450 to 660 mBGS), 0.013 (660 to 840 mBGS) and 0.14 (840 to 860 mBGS) according to Al et al., (2015).

Based on the solute concentrations and isotopes of water, it was determined that the Ordovician aquiclude hosts a saline brine (39% total dissolved solid), which originated from infiltration of evaporated Silurian seawater. The secondary mineralization of halite further reduced the permeability from the Queenston to the Cobourg formations. The preservation of these brines suggests that fluid migration since the Silurian has been minimal. The calculated rate of accumulation of *in-situ* radiogenic helium in the Ordovician aquiclude indicates that the helium has been accumulating and isolated from the underlying allochthonous enriched helium for more than 260 million years. Therefore, the helium data further supports the evidence of the fluid isolation and immobility since Paleozoic time (Clark et al., 2013).

Previous microbial studies examined the presence of microbes within the Michigan Basin (Ilin, 2011; Slater et al., 2013; Clark et al., 2015). To investigate modern microbial activity, Ilin, (2011) obtained environmental DNA from the core samples, which were amplified using 16S rRNA bacterial primers in addition to archaeal 16S rRNA and methanogen-specific (mcrA) primers. While, amplification was not successful for archaeal DNA, trace bacterial DNA was identified for several extremophiles including SRB, with no apparent activity due to the high salinity (Clark et al., 2015). Four distinctive phylogenetic group of *Proteobacteria, Actinobacteria, Cyanobacteria, and Firmicutes* were found. Most species were uncultured extremophilic heterotrophs, while some of these were also able to survive the highly saline conditions. On the other hand, *Proteobacteria* was the most dominant phyla found at all depths, which included heterotrophic, lithotrophic, acidophilic, radiotolerant, and sulfate-reducing species of bacteria (Ilin, 2011, Clark e al. 2015).

Furthermore, in an additional study, trace amounts of phospholipid-derived fatty acids (PFLA) were recovered from core samples. PLFAs were a target of interest because PLFAs are used as chemotaxonomic biomarkers for bacteria species, as phospholipids are the main components of cellular membranes. The study compared amounts of PLFAs in drilling liquid and rock core samples to determine if the source of PLFAs were from contamination during drilling or if they are indigenous to the subsurface environment. The study concluded that the trace amounts of PFLAs either originated from long-term preservation in these layers, or from spores extracted during drilling (Slater et al., 2013). These subsequent studies demonstrate the possibility that this finding is consistent with the hypothesis that biogenic activities once occurred in these layers during the Ordovician prior to Silurian seawater filtration.

In addition to the possibility of Paleozoic microbial activities, the isotopes of methane and CO_2 associated with methane production suggest that the methane in these layers is a result of microbial activity along with the presence of framboidal pyrite. It is likely that methane was produced prior to the infiltration of the hypersaline Silurian seawater; as the salinity reported in these layers are much higher concentrations than salinity tolerance of many microbial species (Oren, 2006, 2011; Clark et al., 2015).

2.2 *Overview of stable sulfur and oxygen isotopes*

The naturally occurring sulfur consists of four stable isotopes: ^{32}S (95.02% abundance), ^{33}S (0.75% abundance), ^{34}S (4.21% abundance), and ^{36}S (0.02 abundance). The isotopic ratio is expressed as a ‰ value relative to Vienna Canyon Diablo Troilite (VCDT) international standard (Krouse and Coplen, 1997; Kendall and Snyder, 2004).

$$\delta^{34}S = \frac{(\frac{^{34}S}{^{32}S})sample - (\frac{^{34}S}{^{32}S})standard}{(\frac{^{34}S}{^{32}S})standard} \times 1000 \qquad [1]$$

On the other hand, the naturally occurring oxygen consists of three stable isotopes: ^{16}O (99.63% abundance), ^{17}O (0.0375% abundance) and ^{18}O (0.1995% abundance). The isotopic ratio is also expressed as ‰ is normalized to Vienna Standard Mean Ocean Water (VSMOW) international standard (Kendall et al., 2004).

2.3 *The sulfur cycle*

The source of sulfate in the ocean is affected by sulfate reduction, sulfide oxidation, dissolution of Ca-sulfate mineral, and the precipitation of marine evaporites (Turchyn and Schrag, 2004). These sources include the inflow of rivers, the weathering of sulfur-bearing minerals, hydrothermal and volcanic sources (Fike et al., 2015).

The sulfur cycle is heavily affected by a range of biogeochemical reactions. These can be facilitated by a variety of microbial metabolic processes such as dissimilatory sulfate reduction, and sulfide oxidation (Fike et al., 2015). About 75 to 90% of the sulfide produced by sulfate reduction is generally re-oxidized back into sulfate via sulfide oxidation (Canfield, 2001; Turchyn and Schrag, 2004; Müller et al., 2013b; Fike et al., 2015). On the other hand, sulfate can also be removed from the seawater by the mineralization of marine evaporites (anhydrite and gypsum), carbonate-associated sulfate, sulfate bound to carbonate mineral lattice or formation of barite (Strauss, 2004; Fike et al., 2015). Most of these reactions impose negligible sulfur isotope fractionation effects. For example, the formation of evaporites from seawater only has a small fractionation effect of $+1.65 \pm 0.12$ ‰ (Thode and Monster, 1965; Strauss, 2004), and the fractionation factor of sulfur isotopes associated with sulfide oxidation ranges from +0.4 to −1.3‰ (Balci et al., 2007; Pisapia et al., 2007).

The reductive portion of the sulfur cycle has the greatest influence on the $\delta^{34}S$ composition of seawater sulfate, while sulfide oxidation has the greatest influence on the ^{18}O composition of sulfate.

Bacterial sulfate reduction requires anaerobic conditions and therefore occurs in anoxic systems such as below the sediment-water interface, or at the anoxic portion of the water column. The oxygen is consumed in the top few millimeters or centimeters of the sediment by aerobic reactions, creating a sharp transition from an oxic to an anoxic system. Sulfate is reduced to sulfide generally with the help of sulfate reducing bacteria.

In an open system, a continuous supply of sulfate is replenished from overlying seawater by diffusion and bioturbation. The pyrite formed in an open system via sulfate reduction will always be depleted in ^{34}S with respect to the seawater sulfate pool. This is because sulfate reduction is preferentially selective towards the lighter $^{32}S_{SO4}$ over heavier $^{34}S_{SO4}$ (Jørgensen,1978; Bottrell and Raiswell, 2000; Antler et al., 2013, 2014).

In most cases, sulfate reduction begins in open systems, which will progressively become closed due to burial. As the sulfate pool becomes more and more isolated from the original source, the pyrite produced via sulfate reduction will differ in isotopic composition compared the pyrite formed from the original seawater. The isotopically light sulfate will be consumed first in a closed system, while residual sulfate pool becomes progressively enriched in isotopically heavy sulfate (Bottrell and Raiswell, 2000). In addition, the source of sulfate may come from a diffusive supply of dissolved sulfate from the surrounding area in late stages of diagenesis. This could originate from overlaying seawater infiltration or from the dissolution of marine evaporate minerals within the sedimentary system. As a result, the isotopic composition of the original

seawater sulfate pool would be altered and the subsquent pyrite fromed from sulfate reduction (Sassano and Schrijver, 1989).

The other part of the sulfur cycle consists of the abiotic and/or biotic oxidization of sulfide minerals through uplift and weathering, which exposes pyritic shales and the biological oxidization (phototrophic and non-phototrophic) of H_2S or S^0. The oxidation of sulfide minerals can also occur in the absence of oxygen where Fe(III) and Mn (IV) are dissolved in solution (Schippers and Jorgensen, 2001). However, ^{34}S fractionation associated with sulfide oxidation is generally considered negligible in these processes (Bottrell and Raiswell, 2000; Canfield, 2001; Fike et al., 2015), but has a more substantial effect in terms of oxygen isotope fractionation (Taylor et al., 1984; Balci et al., 2007; Thurston et al., 2010). This will be further explored in a later section.

2.3.1 *Sedimentary pyrite formation*

Generally, pyrite is formed within the water column or below the sediment-water interface in the presence of dissolved sulfate, organic materials, detrital iron minerals, and H_2S (Berner, 1984; Fike et al., 2015). Sulfate reducing bacteria (SRB) present in these environments uses organic matter as a reducing agent and an energy source, which produces H_2S to react with the detrital iron mineral to form pyrite (Berner, 1984; Tuttle and Goldhaber, 1993; Fike et al., 2015; Markovic et al., 2016). In normal marine environments, the rate of pyrite formation is controlled by the amount of fresh organic matter and reactive iron minerals present in the sediments. However, when organic materials are limited under euxinic conditions, the amount of pyrite formed is more dependent on the amount and the reactivity of detrital iron minerals (Berner, 1984).

In addition, in a natural population of sulfate reducing bacteria, lower rates of sulfate reduction is associated with large ^{34}S depletion in sulfides while higher rates of sulfate reduction are associated with lower ^{34}S depletion in sulfides within natural sediments (Kaplan and Rittenberg, 1964; Habicht and Canfield, 1997).

While there are many forms of pyrite, framboidal and euhedral pyrite are the dominant morphologies that are present in depositional marine environments (Goldhaber, 2003). It is known that framboidal pyrite is generally formed rapidly in supersaturated waters while euhedral pyrite is formed at a slower rate in low saturation waters in sedimentary environments (Raiswell, 1982). The formation process of these minerals will be explained in detail in a later section.

2.3.2 *Bacterial sulfate reduction*

BSR can be coupled with oxidation of H_2 or organic compounds such as acetate, lactate, malate, succinate, fumarate, glucose, fructose or fatty acids. Some sulfate reducers are complete oxidizers or can be incomplete oxidizers. In complete oxidation, the organic compound is oxidized to CO_2. On the other hand, incomplete oxidizers produce short chain organic acids. Nevertheless, most sulfate reducers are incomplete oxidizers (Fike et al., 2015).

The biochemical process of sulfate reduction is relatively well understood. Sulfur isotope fractionation occurs at two different steps within the sulfur reduction process before the end product has been produced (Rees, 1973; Antler et al., 2013). As mentioned above, bacterial sulfate reduction is preferentially selective towards sulfate with lighter isotope ^{32}S due to kinetic isotope effect (Kaplan and Rittenberg, 1964; Sweeney and Kaplan, 1980; Habicht and Canfield, 1997, 2001; Whiticar, 1999; Antler et al., 2014; Fike et al., 2015). The lighter isotope ^{32}S is metabolized rapidly first, and as a result, the sulfate pool becomes enriched in ^{34}S (Antler and

Pellerin, 2018). In the case of a closed system, this can be described by a Rayleigh distillation model.

Studies have reported that the average fractionation factor (ε_s) in pure cultures range between +10 to +45 ‰ (Chambers et al., 1975; Habicht and Canfield, 1997; Canfield, 2001; Turchyn et al., 2006; Fike et al., 2015; Pellerin et al., 2015) and +18 to +45 ‰ in natural populations in modern sediments (Strauss, 2004). Fractionation as high as from +50 and up to +70 ‰ have also been reported (Canfield and Teske, 1996; Habicht and Canfield, 2001; Wortmann et al., 2001). The magnitude of fractionation is not only affected by microbial metabolism, the carbon source, and the amount of dissolved sulfate available (Berner, 1984; Wang and Morse, 1996; Antler et al., 2013), but also the degree of isolation from the sulfate source that determines whether it is an open system or a closed system.

Salinity tolerance of bacterial species is another important characteristic that needs to be considered due to the hypersaline conditions within the Michigan Basin initiated by the infiltration of evaporated Silurian seawater. Microbial activity was likely to be halted following the infiltration of the evaporated Silurian hypersaline seawater because microbial metabolism in highly saline environments is energetically expensive as the cell needs to maintain an osmotic balance between the cytoplasm and the surrounding environment (Oren, 2006). In general, dissimilatory sulfate reduction associated with incomplete oxidizers can tolerate up to 300g/L of NaCl, whereas methanogens can tolerate up to 150g/L of NaCl (Oren, 2011).

At the study site, the salinity (as Cl^- concentration) were reported to be up to 350.64 g/ L of NaCl or 35% salinity from 440 to 700 mBGS (Clark et al., 2015), in contrast to modern oceans with salinity of 3.5% or 35g/ L of NaCl (Cullum et al., 2016). Thus, according to the current literature, it would be unlikely for microbial activity to occur past the establishment of

these highly saline conditions following infiltration of the evaporated Silurian seawater. Furthermore, since the sedimentary system has been isolated for a long time, it is likely to be an energy-starved environment in these layers as electron acceptors have been depleted over time.

2.4 *Sulfate-reducing bacteria's link to methanogenesis*

The previous study conducted by Clark et al. 2015 on isotopic analysis of methane and CO_2 provided evidence of *in-situ* biogenic methane production within the upper Ordovician strata. The isotope data along with the presence of framboidal pyrite initiated the sparked interest of the sulfur cycle since methanogenesis and sulfate reduction are often closely linked in the environment.

Microbes use a sequence of electron acceptors during remineralization of organic matter in the environment. They are depleted from the most thermodynamically favorable to the least; first, it is oxygen, nitrate, iron and manganese oxides, sulfate and finally methane (Turchyn et al., 2006; Mitterer, 2010; Antler et al., 2013). Therefore, in most cases, methanogenesis is heavily restricted in the water column or below the sediment interface that contain a rich supply of sulfate (greater than 200μM) as sulfate-reducing bacteria successfully outcompetes methanogenesis by competitive substrates (acetate, formate). Once all the available sulfate is consumed, SRBs become inactive and methanogenesis proceeds (Whiticar, 1999; Mitterer, 2010).

Depending on the substrate used for methane production, there are various types of methanogens including hydrogenotrophic (H_2/CO_2), acetoclastic (acetate) and methylotrophic (methylated compounds such as methylamine and methyl sulfides) (Vanwonterghem et al., 2016). Similar to the sulfur system, there is a preferential removal of ^{12}C from the residual carbon pool, which shifts the residual substrate towards the ^{13}C enrichment (Whiticar, 1999). In

general, most of the methane produced by methanogenesis in marine sediments is oxidized by anaerobic sulfate reduction (Antler et al., 2013; Antler and Pellerin, 2018). A concurrent ^{13}C-enrichment in CO_2 and ^{13}C-depletion in methane was observed along with the presence of framboidal pyrite. This segment is referred to as the "paleo-bioreactor" at the depth of 525 to 675 mBGS within the Ordovician sequence (Clark et al., 2015; Jautzy et al., 2018).

In most cases, SRB and methanogenic archaea cannot coexist in the same community because; 1) both species compete for the same substrate for used metabolism, and 2) bacterial sulfate reduction is more thermodynamically favorable compared to methanogenesis. However, the possibility of microenvironments could allow these species to coexist at the same time within the layers (Colquhoun, 1991). In the case of methylotrophic methanogenesis, this would be the only scenario where SRBs would coexist within the same community due to the absence of competitive substrate (Mitterer, 2010).

2.5 Pyrite morphology

Various morphologies of pyrite have been reported in a wide collection of studies. This includes: cubic (Shen et al., 2007; Soliman and El Goresy, 2012), octahedral(Schallreuter, 1984; Soliman and El Goresy, 2012), pyritohedral (Alonso-Azcárate et al., 2001; Prol-Ledesma et al., 2010), framboidal (Schallreuter, 1984; Soliman and El Goresy, 2012), euhedral (Zhang et al., 2014; Gallego-Torres et al., 2015), globular (Prol-Ledesma et al., 2010), tubular (Zhang et al., 2014), filamentous (Bonev et al., 2005) and colloform (Gao et al., 2017).

In marine sediments, framboidal pyrite is generally the most common morphology encountered, which also can be accompanied by disseminated euhedral pyrites (Goldhaber, 2003). Framboidal pyrite is rapidly formed first within the water column or below the sediment-water interface, in a solution saturated in sulfate, organic matter and/or detrital iron. As the

solution becomes desaturated with increased burial, euhedral pyrite forms as part of a slower process (Raiswell, 1982). Framboid is derived from the word framboise, the French word for raspberry. Rust, (1935) was the first to use this term to describe its raspberry-like appearance. More specifically, framboid is a spherical aggregate of microcrystals consisting of polyhedral (cubic, octahedral, pyritohedral or spherical) pyrites (Wang and Morse, 1996; Wilkin and Barnes, 1997). While very large framboids (up to 250 μm) have been reported (Sweeney and Kaplan, 1973) and framboids smaller than 1 μm have also been reported, the average size ranges between 5 to 25 μm (Wang and Morse, 1996). In addition to marine environments, framboidal pyrite can also be found in lacustrine, salt marshes (Lord and Church, 1983), preserved in ancient sedimentary rocks (Sassano and Schrijver, 1989; Clark et al., 2015), hydrothermal veins, ore deposits (England and Ostwald, 1993) and coals (Kortenski and Kostova, 1996).

However, the formation process of these authigenic minerals is not well constrained (Wang and Morse, 1996; Ohfuji and Rickard, 2005), as mechanisms of pyrite framboids formation has either been reported as natural biogenic process from pyritic fossilization of bacterial colonies or from the replacement of globules of organic matter or gas vacuoles (Kalliokoski and Cathles, 1969; Rickard, 1970). Inorganic laboratory synthesis is also possible over a wide range of temperatures via the formation of gregites above 250 °C (Murowchick and Barnes, 1987; Graham and Ohmoto, 1994) or under 100 °C (Berner, 1969; Sweeney and Kaplan, 1973, 1980; Wang and Morse, 1996) at either slightly acidic or neutral pH (Ohfuji and Rickard, 2005). Interestingly, framboids have not been produced successfully in any experimental study below temperatures of 23 °C (Ohfuji and Rickard, 2005). All experiments conducted under ambient temperatures have resulted in the formation of pseudo-framboids (Wang and Morse, 1996), which are spherulites consisting of different surface textures (Ohfuji and Rickard, 2005).

2.5.1 Isotopic analysis of pyrite

When the S-isotopic signature of the sulfate sources are known, the investigation of the sulfur isotope composition of authigenic iron sulfides can provide more insight into their formation process. For example, low/ negative $\delta^{34}S$ values in pyrite can suggest potential SRB activity in the past, while positive $\delta^{34}S$ values for pyrite can indicate non-biological origins (Kohn et al., 1998) or late stages in a closed system. In a study by Kohn et al., (1998), they reported $\delta^{34}S$ values ranging from −41 to −5 ‰. Rather, each pyrite grain is not homogenous in terms of $\delta^{34}S$ signatures. To investigate this, they used secondary ion mass spectrometry (SIMS) on pyrite grains showing heterogeneity of $\delta^{34}S$ signatures within each grain. An observable increase in $\delta^{34}S$ can be seen from core to rim in various pyrite (Wang and Morse, 1996; Kohn et al., 1998), which is consistent with the Rayleigh distillation model (Kohn et al., 1998; Wotte et al., 2012). However, depending on the degree of isolation of the sulfate pool, the $\delta^{34}S$ signature of pyrite can range from depleted $\delta^{34}S$ to enriched $\delta^{34}S$ signature. In early diagenesis, the sulfate pool is replenished by the seawater. As a result, the pyrite produced will have depleted $\delta^{34}S$ signatures. As progressive burial occurs, the sulfate pool becomes increasingly isolated from the source, and sulfate reduction continues with the source of sulfate being more and more ^{34}S-enriched. This, consequently induces a formation of a more and more ^{34}S-enriched pyrite as the sulfate sources evolve towards ^{34}S-enrichment as well.

2.6 *Evolution of Paleozoic fluids*

To understand the evolution of the porewater sulfate isotopic composition, we must have a good constraint on the initial $\delta^{34}S$ signatures of the Paleozoic seawater sulfate as the composition of the seawater reflects the original composition of the porewater. Mineral proxies such as barite, gypsum and anhydrite are often used to illustrate the past isotopic composition of

the seawater (Veizer et al., 1997). Barite ($BaSO_4$) is widely formed in various environments such as in the water column, the sediments, and hydrothermal settings. Although barite is a reliable proxy for marine $\delta^{34}S_{SO4}$ record (Strauss, 2004), its isotopic analysis requires meticulous amount of screening (sequential mineral separation by leaching, x-ray diffraction and scanning electron microscopy) (Paytan et al., 2002; Fike et al., 2015; Markovic et al., 2016).

In addition to barite, marine evaporite minerals such as anhydrite and gypsum are also used as a proxy for marine seawater $\delta^{34}S$ signatures. However, this proxy has spatial restrictions and is not consistent with time because it is prone to alteration due to its solubility (Fike et al., 2015). In fact, marine evaporites are deposited in basins that have limited connection to the open ocean limiting their global spatial distribution and potentially representing fluids that have been altered chemically from the open marine waters (Claypool et al., 1980; Marenco et al., 2008; Fike et al., 2015). The typical marine sulfate values of ^{34}S and ^{18}O are presented in Figure 2.3 below. In general, higher variations are associated with $\delta^{18}O$ in marine sulfates.

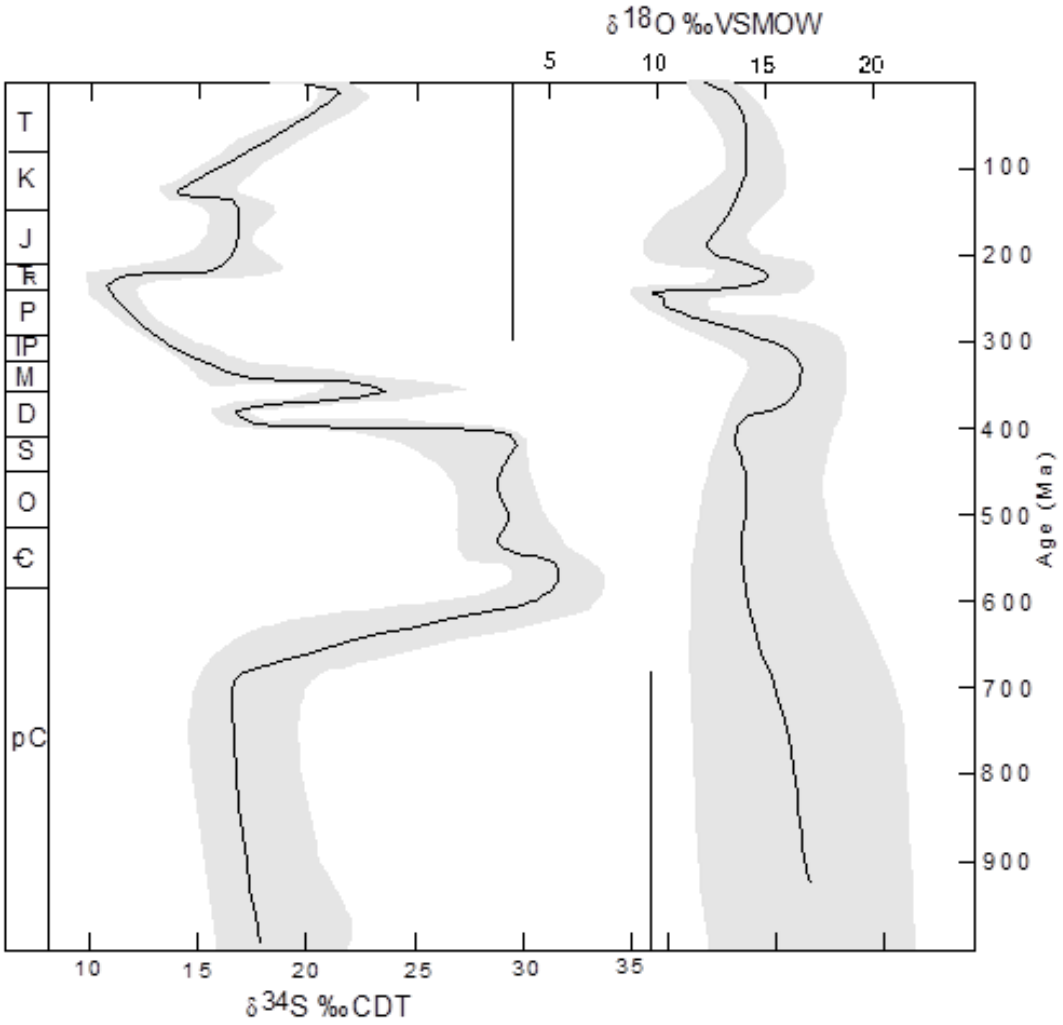

Figure 2. 3: $\delta^{34}S$ and $\delta^{18}O$ marine sulfate through the geological timeline.
Modified from (Clark and Fritz, 1997).

2.7 *Oxygen isotopes in relation to sulfur isotopes*

Oxygen isotopes were proven to be a useful tool for providing additional information that cannot be explained with sulfur isotopes alone. The analysis of oxygen allows us to better understand sulfur cycling in various environments such as deep subsurface, sediment-water interface, soils, aquifers, and acid mine drainage (Deusner et al., 2014). This is because oxygen is continuously incorporated into the sulfate cycle through sulfate reduction and sulfide oxidation, causing fractionation in the oxygen isotopic composition (Bottrell and Raiswell, 2000; Turchyn and Schrag, 2004). Under oceanic conditions (pH above 3 and temperatures below

30°C), the oxygen in sulfate undergoes extremely slow isotopic exchange with the ^{18}O of water (Turchyn and Schrag, 2004;). Lloyd (1968) predicted that it would take over 20 million years for sulfate and water to isotopically equilibrate at the current pH of the oceans.

2.7.1 Oxygen isotope during microbial sulfate reduction

Recently, studies have shown that the $\delta^{18}O$ of sulfate approaches a constant value while $\delta^{34}S$ continues to increase with time during sulfate reduction. This is largely due to kinetic and equilibrium isotope effects (Wortmann et al., 2007) and also due to the oxygen isotope exchange that occurs between water and the intermediate species of bacterial sulfate reduction (Fritz et al., 1989; Brunner et al., 2005). During microbial sulfate reduction, the preferential selection of sulfate with lighter oxygen isotopes is coupled with the enzymatic reaction that encourages the oxygen isotopic exchange between sulfate and water (Antler et al., 2013; Fike et al., 2015). This leaves the residual sulfate pool to be isotopically enriched in ^{18}O and produces a $\delta^{18}O$ enrichment of +8 to +12 ‰ in the sulfate relative to water (Bottrell and Raiswell, 2000; Böttcher et al., 2001; Turchyn and Schrag, 2004; Turchyn et al., 2006).

Since microbial sulfate reduction promotes oxygen exchange between the sulfate and water, the resulting sulfate pool is strongly affected by the isotopic composition of the water (Fritz et al., 1989; Brunner et al., 2005; Turchyn et al., 2006, 2010, Antler et al., 2013, 2014; Müller et al., 2013a). Fritz et al., (1989) used sulfate with differing $\delta^{18}O$ signature to grow sulfate-reducing bacteria. As a result, the $\delta^{18}O$ of the sulfate pool plateaued at around +20 ‰ regardless of the initial $\delta^{18}O_{SO4}$ signatures of the sulfate pool. On the other hand, Brunner et al., (2005), incubated SRBs in waters with varying $\delta^{18}O_{H2O}$ signatures, which ranged from −20 to + 80 ‰ and showed the $\delta^{18}O_{SO4}$ was affected by the $\delta^{18}O$ of water as it varied. In addition, in environments with high sulfate reduction rates, the $\delta^{18}O_{SO4}$ increases more slowly relative to

$\delta^{34}S_{SO4}$, while environments with lower sulfate reduction rates, the $\delta^{18}O_{SO4}$ of sulfate increased more quickly with respect to $\delta^{34}S_{SO4}$ (Antler et al., 2013).

2.7.2. Oxygen isotope during sulfide oxidation

Although sulfide oxidation does not have a big impact when it comes to the $\delta^{34}S$ composition of sulfate (Balci et al., 2007; Fike et al., 2015), it plays a vital role in terms of understanding the oxygen isotopic composition of sulfate. This is because sulfide oxidation plays a vital role in the sulfur cycle as it is linked to the carbon and oxygen cycle, which can give us insights into microbial activity and geochemical processes (Kohl, 2010) within the Michigan Basin. There has been a significant amount of research on the sulfide oxidation due to its association with acid mine drainage (Moses et al., 1987; Balci et al., 2007; Pisapia et al., 2007; Tichomirowa and Junghans, 2009). Despite a large amount of research on sulfide oxidation, there is still much uncertainty associated with various topics on sulfide oxidation (Toran and Harris, 1989; Kohl and Bao, 2011). Topics such as; 1) variability in the amount of oxygen within water that participate in the oxidative reaction; 2) the roles of intermediate species formed during different condition; and 3) distinguishing the difference between abiotic or microbial sulfide oxidation in terms of oxygen isotope signatures are all still the subject of continuous research effort.

In the article by Van Stempvoort and Krouse (1994), they outlined the major factors that may affect $\delta^{18}O$ signatures of sulfate summarized by (Kohl, 2010):

1) The different pathway of sulfide oxidation, which the sulfate is formed from as sulfide oxidization is a multi-step reaction involving the formation of various intermediate species.

2) The source(s) of oxygen that incorporated into sulfate during sulfide oxidation (atmospheric, dissolved O_2, water).
3) The $\delta^{18}O$ of these oxygen sources.
4) The different oxidizing agents, catalysts or enzymes involved in sulfide oxidation (O_2, Fe (III), Mn (IV), NO_3^-), which could be either biotic or abiotic.
5) Physicochemical conditions such as pH, P_{O2} and temperature.
6) Isotope enrichment factors associated with incorporation of oxygen during sulfide oxidation reaction.

Despite much uncertainty, what is known so far is that the oxidation of pyrite to sulfate can occur in the presence or absence of O_2. When O_2 is absent, sulfide oxidation can proceed with dissolved O_2, Fe (III), Mn (IV), and NO_3^- (Schippers and Jorgensen, 2001). Sulfide oxidation can occur not only at low pH (Nordstrom et al., 2007; Heidel et al., 2009; Heidel and Tichomirowa, 2011), but also under circumneutral to alkaline conditions (Moses and Herman, 1991; Kohl and Bao, 2011). Moreover, it can occur simultaneously via different pathways in nature and laboratory experiments, which makes it difficult to characterize isotopic values originating from either biotic or abiotic processes (Toran and Harris, 1989). Also, the presence or absence of the various oxidants can affect oxygen isotope composition as these are the parameters that control the competition between the rate of sulfite oxidation and rate of oxygen isotope exchange with the surrounding water (Müller et al., 2013b). These reactions can also be facilitated with the help of microorganisms (Taylor et al., 1984).

2.7.2.1 Role of Fe (III) in sulfide oxidation

Sulfide oxidation can proceed with or without O_2 in the presence of dissolved Fe (III) (Taylor et al., 1984). This is because Fe (III) is the main component responsible for the oxidation

of pyrite regardless of pH conditions (Moses and Herman, 1991; Reedy et al., 1991). Dissolved O_2 however, does help sulfide oxidation by converting Fe (II) to Fe (III) (Taylor et al., 1984; Van Stempvoort and Krouse, 1994). The solubility of Fe (III) tends to decrease with an increase in pH due to the formation of iron hydroxide species at high pH (Gleisner and Herbert, 2002). Even at low concentrations, Fe (III) is still able to oxidize sulfide minerals without dissolved oxygen (Moses et al., 1987).

The oxidation reaction of pyrite (FeS_2) by Fe (III) to SO_4^{2-} requires the transfer of seven moles of electrons per mole of sulfur. During the formation of intermediate species, only one or two electrons can be transferred per step (Kohl and Bao, 2011). Intermediate species typically include thiosulfate, sulfite, and elemental sulfur, while most of the isotope fractionation occurs during the oxygen isotope exchange of sulfite with water (Brunner et al., 2005). Therefore, the reaction below is a simplification of a multistep pyrite oxidation reaction.

$$FeS_2 + 14\ Fe^{3+} + 8\ H_2O \rightarrow 15\ Fe^{2+}\ 2\ SO_4^{2-} + 16\ H^+ \qquad [2]$$

In an experiment conducted by Reedy et al., (1991) to better understand the role of dissolved O_2 and water, they tested abiotic oxidation of pyrite with and without the addition of Fe (III) at pH of 1 to 7, and temperatures below 70°C. By measuring isotopic isomers of sulfate, they found that 90 to 100% of the oxygen came from water, and the percentage of oxygen that contributed from water was increased when Fe (III) was added. The pathways within the oxidation of sulfide could also vary in terms of pH conditions (Heidel et al., 2009; Kohl and Bao, 2011). Based on aerated oxygen labeled experiments, it is suggested that the intermediate species produced during pyrite oxidation is dependent on the pH. At low pH (<3), tetrathionate is a product of thiosulfate oxidation by Fe (III) whereas in alkaline solutions the intermediate species are mainly thiosulfate and sulfite (Kohl and Bao, 2011). Moreover, Van Stempvoort and Krouse,

(1994) quoted the thesis by Qureshi, (1986) which suggested, as the pH increased, the $\delta^{18}O$ of sulfate tended to become more depleted. He also concluded that pH caused variation in the different oxidation reaction pathways. Where at higher pH, more thiosulfate and polythionates is formed and as the rate of sulfite-water oxygen decreases, a depleted value can be seen for $\delta^{18}O$ of sulfate where less sulfite-water oxygen exchange is occurring. Regardless of the reaction pathway for sulfide oxidation, the product before the final sulfate is either sulfite or bisulfite (Kohl and Bao, 2011).

2.7.2.2 Role of Mn (IV) in sulfide oxidation

Much research has been done on the role of Fe (III) during sulfide oxidation, while little is known about the role of Mn (IV) during anaerobic sulfide oxidation until Schippers and Jorgensen, (2001) were the first to conduct oxidation experiments with pyrite and iron sulfide at pH of 8. They found MnO_2 was able to oxidize pyrite in the absence of other oxidizing agents such as Fe (III) and NO_3^- and the overall reaction can be summarized by the equation:

$$FeS_2 + 7.5\ MnO_2 + 11\ H^+ \rightarrow Fe(OH)_3 + 2\ SO_4^{2-} + 7.5\ Mn^{2+} + 4\ H_2O \qquad [2.5]$$

They reported that pyrite was oxidized to sulfate along with other sulfur intermediates such as thiosulfate, trithionate, tetrathionate and pentathionate over 35 days. In addition, pyrite oxidation by MnO_2 resulted in rates of 1.02 and 1.12 nmol $m^{-2}\ s^{-1}$ while Fe (III) reported oxidation rates of between 1.1 to 39 nmol $m^{-2}\ s^{-1}$ from previous studies summarized by Peiffer and Stubert, (1999). The reason why the MnO_2 rates are lower than Fe (III) rates may be because oxidation reaction by MnO_2 inherently produces iron hydroxide thus Fe (III) will always be present within the system. Therefore, Fe (III) still remains to be the dominant oxidizing agent in the presence of MnO_2 and at circumneutral pH. Its role is to indirectly oxidize pyrite by re-oxidizing Fe (II) to Fe (III) at the iron sulfide surface when Fe (III) is present in the system.

Thus, Fe (II)/Fe (III) electron shuttle is present at the mineral surface (Van Stempvoort and Krouse, 1994; Schippers and Jorgensen, 2001).

Although Schippers and Jorgensen 2001 demonstrated that iron sulfides can also be oxidized by MnO_2 in the absence of Fe (III), its application towards the Michigan Basin must be carefully considered. First, MnO_2 and FeS_2 are highly insoluble, thus in their study they have suggested that a tight contact of the mineral surfaces may be required for the reaction to occur. Secondly, high MnO_2 content along with strong bioturbation that enables continuous mixing is required for the chemical reaction to proceed. These conditions are not met in the case of the Michigan Basin, as low MnO_2 content along with the lack of mixing within the porefluid.

2.7.2.3 Oxygen isotope fractionation associated with sulfide oxidation

Oxygen from water is continuously incorporated into sulfate during sulfide oxidation, altering the isotopic composition of sulfate. Figure 2.4 illustrates the oxygen isotopic composition of sulfate according to the percent of oxygen in the water that participates during sulfide oxidation. Schwarcz and Cortecci, (1974) were the first to demonstrate that the resulting sulfate from pyrite oxidation contains at least half of the oxygen derived from the water molecule. Despite the large amount of efforts made by researchers in order to characterize the percent of oxygen from water that participate in sulfide oxidation, the range varies considerably between the studies: 23 to 100% (Taylor et al., 1984), 87% (Balci et al., 2007), 91% (Heidel and Tichomirowa, 2010) and 71 to 79% (Kohl and Bao, 2011). While Van Everdingen and Krouse, (1985) found about 29 to 100 % of the sulfate contained oxygen derived from water in laboratory experiments and 35 to 90 % were found in field studies. In addition, reaction kinetics also affect the isotopic composition of oxygen in sulfate as Reedy et al., (1991) demonstrated that the longer the experiments were run, the more oxygen from water was found in the resulting sulfate.

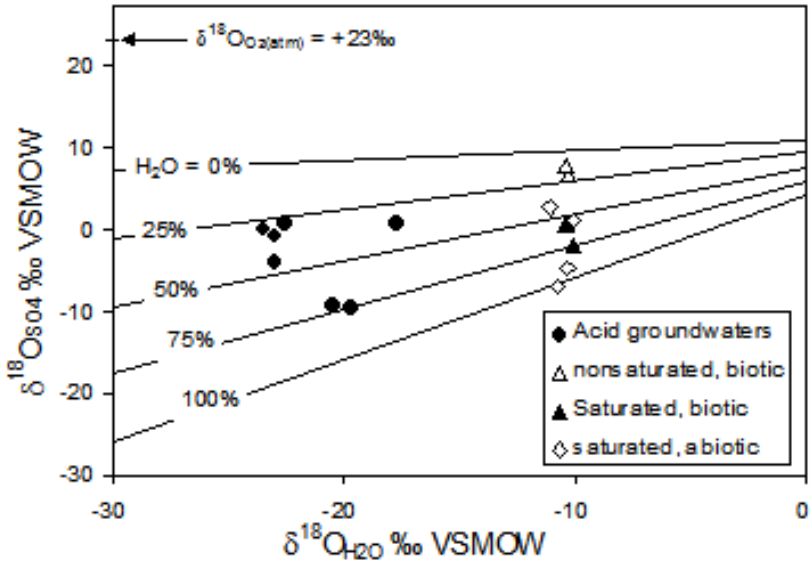

Figure 2. 4: The $\delta^{18}O_{H2O}$ and $\delta^{18}O_{SO4}$ associated with a range of H_2O-derived oxygen fraction participating in sulfide oxidation
Based on the known values of $\delta^{18}O_{H2O}$ and $\delta^{18}O_{SO4}$, we can predict how much the surrounding water contributes to the oxygen isotopic composition of sulfate. (From Clark and Fritz, 1997, modified from Taylor et al., 1984).

Moreover, the $\delta^{18}O_{SO4}$ signatures depend on a considerable range of isotope effects linked to the fraction of oxygen from water contributing to pyrite oxidation. The oxygen isotopic fractionation between sulfate and water ($\varepsilon^{18}O_{SO4\text{-}H2O}$) has been reported to be between +2.3 and +8.2 ‰ in the presence of Fe (III). While the oxygen isotopic fractionation between sulfate and O_2 is reported to be between −4.3 and −11.4 ‰ (Müller et al., 2013b). Table 2.1 below summarizes the ranges of oxygen fractionation factors obtained from literature. By using those values, a mass balance of $\delta^{18}O$ of porewater sulfate values from sulfide oxidation can be calculated from the equation obtained from Van Everdingen and Krouse, (1985):

$$\delta^{18}O_{SO4} = Y\,(\delta^{18}O_{water} + \varepsilon_w) + (1\text{-}Y)\,[0.875(\delta^{18}O_{air} + \varepsilon_{air}) + 0.125(\delta^{18}O_{water} + \varepsilon_w)] \quad [3]$$

Therefore, we can use the $\delta^{18}O$ composition of sulfate to roughly differentiate between sulfate that are altered by sulfate reduction and sulfate that have been produced by sulfide oxidation by comparing experimental values to values found in literature.

Table 2. 1 Summary of oxygen isotope fractionation during oxidation of sulfide minerals

Mineral	Biotic/ Abiotic	Presence of Fe (III)	Aerobic/ Anaerobic	pH Range	Oxygen Isotope Fractionation		Reference
					$\varepsilon_{SO4\text{-}O2}$	$\varepsilon_{SO4\text{-}H2O}$	
Pyrite	Biotic	-	Aerobic	2.0	−11.4		(Taylor et al., 1984)
Pyrite	Abiotic	Fe (III)	Anerobic	2.0		+4.1	(Taylor et al., 1984)
Pyrite	Abiotic	-	Aerobic	2.0	−4.3	0.0	(Taylor et al., 1984)
Pyrite	Abiotic	Fe (III)	Aerobic			+5.0	(Taylor et al., 1984)
Pyrite	Abiotic	-	Aerobic	2.2-2.7	−9.8	+2.8	(Balci et al., 2007)
Pyrite	Biotic	-	Aerobic	2.2-2.7	−10.8	+3.5	(Balci et al., 2007)
Pyrite	Biotic	-	Aerobic			+2.0	(Brunner et al., 2008)
Pyrite	Abiotic	Fe (III)				+2.6	(Van Everdingen and Krouse, 1985)
Pyrite	Abiotic	Fe (III)	Anaerobic	1.4-2.0		+2.3	(Heidel and Tichomirowa, 2011)
Chalcopyrite	Abiotic/ Biotic	Fe (III)	Anaerobic	1.8-2.2		+3.8	(Thurston et al., 2010)
Chalcopyrite	Biotic	-	Aerobic	1.8-2.2		+6.4	(Thurston et al., 2010)

2.7.2.4 Oxygen isotope during microbial sulfide oxidation

Generally, the rate of sulfide oxidation is significantly increased in the environment with the help of bacteria (Taylor et al., 1984). At low pH (3 to 5) *T. ferrooxidans* greatly enhances the rate of pyrite oxidation while the effect was minimized at pH of around 6 (Van Stempvoort and Krouse, 1994). Some microbes attach themselves on to sulfide mineral surfaces and use enzymatic electron transport mechanisms (Kelly, 1982) to oxidize the sulfur atoms directly while others microbes generates Fe (III) from Fe (II) to oxidize sulfide indirectly (Van Stempvoort and Krouse, 1994). There are also a considerable amount of uncertainties surrounding biotic sulfide oxidation as it is believed that microbes can participate in one or more step(s) during the sulfide oxidation process while abiotic processes can dominate other steps. Therefore, it is difficult to

distinguish whether the sulfate was produced by abiotic or biotic reactions solely based on isotopic data (Van Stempvoort and Krouse, 1994).

Generally, under anaerobic conditions, all of the oxygen in sulfate is derived from water (Balci et al., 2007). As a result, the $\delta^{18}O_{SO4}$ is below +5 ‰ and it can be as low as −20 ‰ (Van Stempvoort and Krouse, 1994; Balci et al., 2007).

2.7.3 Other factors affecting the $\delta^{18}O$ of sulfate

There are two potential processes that may also affect the $\delta^{18}O$ signature of sulfate. First, the precipitation of sulfate minerals such as anhydrite and gypsum causes a depletion in $\delta^{18}O$ of sulfate due to fractionation of oxygen between dissolved and mineral sulfate by an order of 2 ‰. The second process is the lack of mixing in an evaporating basin, where the sulfate that are dissolved may not be homogeneous, thus causing a variation in $\delta^{18}O$ signature of sulfate (Van Stempvoort and Krouse, 1994).

In addition to the two potential processes above, Heidel et al., (2009) tested sulfide oxidation on different grain sizes of pyrite under aerobic, acidic conditions to see if there is any influence on the final $\delta^{18}O$ of sulfate. They speculated that grain size of 63 to 100, 100 to 140, and 140 to180 μm all indicate similar oxidation mechanism. While ultrafine grain size <63 μm resulted in higher $\delta^{18}O$ values for sulfate.

2.8 *Porewater extraction methods for low permeability rocks*

A method of extracting representative samples of *in-situ* porewaters developed by Celejewski et al., (2014) utilizes hydrophilic cellulosic membrane by absorption. Solute concentrations are calculated from the independent mass measurement of the solutes by Inductively-Coupled-Plasma Mass Spectrometry (ICP-MS) and water content was quantified by

Near-Infrared Spectrometry (NIR). Sorption experiments resulted in no preferential sorption of the solutes (Na^{2+}, Cl^{-}, Mg^{2+}, Ca^{2+}, K^{+}, Sr and Br^{-}) onto the cellulosic membrane. This method successfully avoids the creation of chemical artefacts from mineral dissolution and ion exchange and also allows the extraction of very saline porewaters that are in equilibrium with soluble minerals (Celejewski et al., 2014).

However, this method is not suitable for porewater sulfate isotopic characterization due to very low concentrations of sulfate present in the porewaters. For the isotopic analysis of sulfur on the EA-IRMS, about 0.400 mg of $BaSO_4$ or 50 µg of sulfur is required according to the Ján Veizer Stable Isotope Laboratory guidelines. Celejewski et al., (2014) reported 0.10 to 0.15 mg of sulfate from one cellulosic sheet. This would require the leaching of multiple sheets for one core sample to collect enough sulfate. Additionally, a controlled environment must be constructed to prevent the evaporation of porewaters when the core is cleaved. This is because the anaerobic chamber has low humidity, which promotes high evaporation rates. Small amounts of porewater present in the cores, which is likely to evaporate as soon as it is exposed to the drier air, implying that the cellulosic sheets will not be able to absorb the porewater unless a controlled humid environment is created.

3. Methodology

3.1 *Rock core preparation*

The removal of the external layer (approximately 1 cm) of the rock core segment was performed to minimize potential contamination of the outer layer by drilling fluids or handling. The core segment was covered in aluminum foil and labeled. All surfaces and tools were cleaned with deionized water (DI), methanol (MeOH) and dichloromethane (DCM).

3.1.1 *Granular rock crushing*

The core segment was transferred to the anaerobic chamber for crush-and-leach to prevent the oxidation of sulfide-bearing minerals such as pyrite. All surfaces were cleaned with MeOH and DCM. Then the cores were wrapped in pre-cleaned aluminum foil and crushed with a hammer that was wrapped in pre-cleaned aluminum foil. The rock core pieces were further crushed into smaller grains with a stainless steel pre-cleaned-mortar and pestle. The crushed sample was stored in pre-cleaned amber glass jars inside the chamber. All the surfaces were cleaned, while nitrile gloves and aluminum foil surface lining were changed after every sample to avoid cross-contamination.

3.1.2 *Powdered rock milling*

Powdered core segment was prepared by anaerobic ball-milling technique. The granular sample was loaded into an air-tight ball mill cell in the anaerobic chamber. The cells were cleaned with DI water, MeOH and DCM prior to usage. The loaded cells were then taken to the Ján Veizer Stable Isotope Laboratory to be milled. The ball mill ran for two minutes at the highest frequency. After the samples became powdered, the cells were transferred back into the anaerobic chamber where the powdered samples were stored in pre-cleaned amber glass jars.

3.2 Previous method for filtration, precipitation of $BaSO_4$ filtration and analysis

The general method for $BaSO_4$ precipitation was obtained from the Ján Veizer Stable Isotope Laboratory. The methodology is used for liquid samples ranges from 250 to 500 mL per sample. Whereas samples in this study yielded 20 to 50 mL of porewater leachates.

First, pre-filtration was done to remove any particulates in solution and then the solution was acidified to a pH of 3 to 4 with 5% HCl solution. Next, 10 mL of 0.25M $BaCl_2$ solution was added to the acidified solution so barium can form $BaSO_4$ with the dissolved sulfate within the

sample. Once the precipitation has completed after 24 hours, the precipitate was filtered through a vacuum filtering apparatus lined with nitrocellulose filters. The $BaSO_4$ precipitate that was captured on the filter is then dried in an oven at 50 to 60°C overnight. Finally, the dried precipitate was scraped off the filter and transferred into a microcentrifuge tube for storage. Typically, samples processed by this methodology yielded about 200 mg of $BaSO_4$ or more.

For the analysis on the EA-IRMS, about 0.450 mg of dried $BaSO_4$ is transferred into a 5 X 2 tin capsule along with ~1 mg of WO_3. The capsule was squeezed into a ball to make sure there was no oxygen trapped in the capsule during analysis.

3.3 Filter testing for Elemental Analyzer- Isotope Ratio Mass Spectrometer

The sulfur and oxygen isotopic signatures were analyzed by EA-IRMS. Due to low concentrations of sulfate obtained from porewater samples, a new method had to be developed to analyze small amounts of $BaSO_4$ deposited onto a filter after filtration.

To test the whole filter combustion method, a lab standard of $BaSO_4$ was obtained from the Ján Veizer Stable Isotope Laboratory and was homogenized with a mortar and pestle before the analysis on the EA-IRMS. Ten replicates of $BaSO_4$ were analyzed to obtain the $\delta^{34}S$ value of the laboratory standard. Five different blank filters composed of nylon, nitrocellulose, silver, glass and quartz filters were analyzed in the EA-IRMS. All filters had a 25 mm diameter; nitrocellulose filter and silver filter had 0.45µm pore-size, glass filter had a GF/F grade. The laboratory standard of $BaSO_4$ was re-suspended in DI water and then deposited onto the different filters via filtration. Once the precipitate was dried in the oven, the whole filter along with $BaSO_4$ was folded into a 10 x 10 tin capsule. 1 to 2 mg of 1:1 glucose and quartz mixture was added to the tin capsule to help with the combustion of the samples in the elemental analyzer.

Each type of filter was analyzed five times as methodological replicates in order to verify if the filter would alter $\delta^{34}S$ signature during analysis in the EA-IRMS.

3.4 *24-hour anaerobic porewater leaching*

To prepare the water for leaching, DI water obtained from the tap of ARC216 at the University of Ottawa was flushed with nitrogen gas for at least 3 hours prior to use. This was done to prevent the presence of dissolved oxygen from oxidizing the sulfide minerals during leaching. Most samples required 30 g or more of granular rock sample or powdered rock sample. Mass of the empty falcon tube was obtained prior to weighing out the sample. Mass of the falcon tube plus dry rock was weighed after the rock was transferred into a labeled 50 mL falcon tube. The deoxygenated deionized water was used to fill the tube until 50 mL waterline. After the cap was fixed on, the tube was inverted three times to ensure the sample is well mixed with the water, and additional DI water was added if the watermark did not reach 50 mL after it was homogenized. The mass of the falcon tube containing the rock and water was obtained. Finally, the seam between the cap and the tube was taped with electrical tape to prevent exposure to oxygen during centrifuge in the next step.

After the samples were leached for 24 hours, the sample tube was inverted three times to allow homogenization of the solution and was centrifuged outside of the anaerobic chamber for five mins at 4200 rpm. While the samples were spun, 25 mm nitrocellulose filters were placed in the filter holders. Beakers, syringes and new 50 mL falcon tubes were labeled in otder to maintain organization. After the centrifugation was complete, all the materials and samples were brought into the anaerobic chamber. While the syringe filtering apparatus was held directly above the clean falcon tube, the leachate was carefully poured into the syringe and was filtered through.

3.4.1 *Precipitation and filtration of $BaSO_4$ for sulfur isotope analysis*

Anoxic porewater leachate samples were submitted to the University of Ottawa Geochemistry laboratory for sulfate concentration analysis. Based on the concentration of sulfate, the amount of leachate needed for 70 µg of S for sulfur isotopic analysis was calculated. The amount of leachate required (with additional 5-10 mL to account for loss during filtration) was pipetted into a new 50 mL falcon tube. The samples were acidified until it reached a pH of 3 to 4 with dilute HCl to prevent precipitation of $BaCO_4$. A 0.25 M $BaCl_2$ stock solution was prepared in an amber glass jar and 2 mL of $BaCl_2$ was added after acidification. The samples were left to precipitate for 24-hours.

Prior to filtration, the masses of blank 25 mm diameter nitrocellulose filters were obtained, then stored in two overlaying aluminum weigh boats to prevent additional dust particles from settling onto the filters. The filters were weighed to measure the mass of precipitate captured onto the filter after filtration and drying.

After the 24-hour precipitation, the sample tubes are sonicated for ten minutes to ensure all the precipitates were suspended in solution. Filtering apparatus was set up by using a 50 mL all-plastic syringe with the luer-lock tip attached to the filter holder holding a pre-weighed 25 mm nitrocellulose filter. The plastic syringe was washed with DI water prior to use to remove plastic fibers. While the syringe was attached to the filter holder, the falcon tube was rinsed three times into the plastic syringe to ensure all of the precipitates has been rinsed.

Next, the same falcon tube was filled to the 50 mL mark with DI water and sonicated for another five minutes to suspend residual precipitate that may still have been attached to the walls of the plastic falcon tube. The falcon tube was rinsed three times into the filtering apparatus once again before the filter was dried in the oven.

The addition of two sonication steps and rinsing has increased percent recovery from 65% to 84%. This was tested by re-suspending and filtering 27 methodological replicates of laboratory standards with either $CaSO_4 \cdot 2H_2O$ or Na_2SO_4. This is critical because the actual concentration of sulfate within the porewater samples is very low and having enough samples for isotopic analysis is crucial.

3.4.2 Analysis of $\delta^{34}S$ of porewater sulfate on the EA-IRMS

Filters that contained excess precipitate were cut into corresponding portions based on the mass obtained by subtracting the empty filter from the mass of the filter and the precipitate. The scissors were cleaned prior and after cutting samples with kimwipe. Samples (~0.460 mg) of $BaSO_4$ along with nitrocellulose filter were folded into a 10 x10 tin capsule and flash combusted in the elemental analyzer (Elementar Isotope Cube) furnace at 1800℃ where $BaSO_4$ was converted into SO_2 gas under a helium atmosphere. In order to help the sample combustion, extra oxygen was added to account for the excess carbon from the nitrocellulose filters. The released gases were cleaned and separated using a combination of traps and chromatographic column then directed to the Thermo Conflo IV where it is diluted to accommodate ionization and S-isotope analysis with a Thermo Delta Plus XP. The analytical precision is +/−0.2 ‰. The $\delta^{34}S$ of sulfate were measured at the Ján Veizer Stable Isotope Laboratory at the University of Ottawa. The data was normalized to three sulfate standards; IAEA-NBS-127 (+20.3 ‰), T-123 (−0.22 ‰) and HAS-1 (+24.4 ‰). A linearity correction based on a range of different weights using T-123 standard was applied to the samples. Three barite bypasses along with two blanks were run before the three standards to ensure the equipment was running at optimal settings.

3.4.3 *The effect of grain size during leaching on the $\delta^{34}S$ of porewater sulfate*

In addition to testing full filter combustion, the effect of grain size on the $\delta^{34}S$ signature of porewater sulfate was tested. In previous studies, for the crush-and-leach method, grain size ranged from 2 to 4 mm were used for leaching. Samples were traditionally crushed aerobically by a rock crushing machine. Since crushing core samples manually within an anaerobic chamber was time-consuming and required a large amount of physical force, crushed core samples were limited in quantity. Therefore, the effect of grain size on the $\delta^{34}S$ signature was tested to see if different grain leach contributed to the changes in the $\delta^{34}S$ signature. Grain sizes that was tested ranged from: powder, less than 2 mm, less than 4 mm, 2 to 4 mm and greater than 4 mm. Samples with 2 to 4 mm grain size were sieved with two sieves stacked on top of each other in the anaerobic chamber. A sheet of clean aluminum foil was placed underneath to catch the remaining samples. After mechanical separation, the sieves were scrubbed with soap and rinsed with DI water. Then the standard anaerobic leaching, precipitation, filtration and analysis steps followed.

3.5 *Sulfate-bearing mineral analysis*

The presence of gypsum and anhydrite was identified on intact core samples by testing the hardness and using the acid test to distinguish from visually similar; calcite, dolomite and halite. Powdered gypsum and anhydrite samples were obtained by using a Dremel tool. The powdered samples were collected onto a weighing paper and transferred into a labeled plastic vial. Each vein was drilled at different spots to check for homogeneity. The powdered samples were weighed into a 5 x 2 tin capsule with approximately 1 mg of sucrose and quartz (1:1) mixture in order to help with the combustion of the sample during the analysis on the EA-IRMS.

Core samples were taken from DGR-3, 4, 5 and 6 boreholes. DGR-5 and DGR-6 samples required depth correction as these two cores were inclined during drilling (Raven et al., 2011). Corrected depth was obtained from previous studies. Since the sample DGR-6-790.32 did not have a corresponding corrected depth from previous studies, degree of inclination was calculated by:

$$\frac{corrected\ depth\ (m)}{measured\ depth\ (m)} = degree\ of\ inclination \quad [4]$$

Where the averages of the degree of inclination were taken from five random samples in DGR-6. The degree of inclination is 0.8681.

$$790.32\ m\ \times 0.8681\ = 686.11\ m$$

3.7 *Precipitation of $BaSO_4$ for oxygen isotope analysis*

About 60 to 80 g of granular or powdered rock samples were leached in two separate 50 mL falcon tubes. The full vertical profile was created with a total of 27 samples. The same 24-hour leaching and filtering protocol as above was followed. The mass of water used for leaching, the mass of leachate and the mass of the wet rock was obtained for concentration calculation. During filtration, the same syringe was used to filter the same sample. The two aliquots of filtered leachate are homogenized by shaking the tube briefly for three seconds. Then about 2 mL of porewater leachate was used for geochemical concentration analysis. The rest of the leachate was used for $BaSO_4$ precipitation. Scintillation vials were labeled and placed on metal rack prior to precipitation.

After 24-hourprecipitation, the 50 mL falcon tube was sonicated for five minutes in the ultrasonic bath and then spun in a centrifuge at the 4200 rpm for a minimum of five minutes. After centrifugation, the supernatant was removed by pipetting the liquid carefully out with a 10

mL pipet. Once most of the liquid was removed from the falcon tube, the precipitate was mixed into a slurry with a clean scoopula. The scoopula was first rinsed into the scintillation vial with DI water and then the slurry was transferred into the vial. Finally, the falcon tube was rinsed with a little bit of DI water into the vial to capture the rest of the precipitate.

The vials were placed on a metal test tube rack. The samples are dried in an oven set at 60°C. Once the precipitate had settled onto the bottom, the excess water was carefully pipetted out with a 2000 µL pipet, then it is left to dry for at least 24 hours. Once the solid samples have dried, any samples with NaCl formed between the $BaSO_4$ powder on the bottom of the vial was rinsed again with DI water and was re-dried.

Once the samples were completely dried and free of NaCl, they were capped to prevent CO_2 exchange with the atmosphere. The oxygen isotopic ratio was determined at the Ján Veizer Stable Isotope Laboratory at the University of Ottawa. About 0.380 mg of $BaSO_4$ was weighed into a silver capsule for the pyrolysis in the TC/EA-IRMS. The zero blank carousels was purged with helium to replace the oxygen that is present. The sample was converted to CO, H_2 and N_2 at temperatures of 1450°C. The gas that was cleaned and then separated by a 5A GC column at 90°C. Then the CO gas was diluted in by the Thermo Conflo IV to accommodate the Thermo Delta Plus XP to analyze for oxygen isotope ratio. The analytical precision is +/−0.2 ‰. Standards IAEA-601 (+23.14 ‰) IAEA-NBS-127 (+9.23 ‰) and IAEA-SO-6 (−11.0 ‰) was used to normalize the results. T-123 was used for linearity check. Three barite bypasses along with two blanks were run before the three standards to check for optimal analytical conditions and to check for potential contamination.

3.8 *Sample preparation for porewater geochemistry analysis*

For anion (SO_4^{2-} and Cl^-) concentration analysis, 1 mL of porewater leachate was pipetted into a clean 15 mL falcon tube and was diluted with 9 mL of DI water. The masses were recorded for dilution calculation. For cation (Ca^{2+}, Sr^{2+}, Total Fe, Total Mn) analysis, 1 mL of leachate was diluted with 9 mL of 1.1% HNO_3 for 10X dilution. For Na^+ and Ca^{2+} concentration analysis, 100X dilution solution was prepared with the 1 mL of 10X diluted HNO_3 solution and 10X dilution porewater from the previous step. The porewater was further diluted to accommodate for high Ca^{2+} and Na^+ concentrations present in these porewaters (Raven et al., 2011; Clark et al., 2013).

3.8.*1 Porewater geochemistry*

Ion chromatography DIONEX ICS-2100 was used for anion concentration analysis. The machine was degassed and then cleaned for an hour prior to use. The calibration range is set at 10 ppm for samples with ionic concentrations ranging from 0.1 to 20 ppm. Standards were prepared from Ultrascientific analytical solution at 1000 mg/mL dissolved in low total organic carbon (TOC) water. Calibration standards at 0.625, 1.25, 2, 5, 5 and 10 ppm were run for a calibration curve. 1.25 ppm check standards are run between every ten samples to check for system stability.

Agilent Technologies 4200 Microwave Plasma-Atomic Emission Spectrometer (MP-AES) was used for cation analysis. Blanks along with DI blanks were run prior to samples to check for contamination, and 1.25 ppm check standards are run between every ten samples to check for system stability.

3.9 *Anaerobic chamber breach*

Prior to oxygen analysis (third round of leaching), the anaerobic chamber was breached by another user in the laboratory. The hydrogen tank was turned off for a week, which allowed some dioxygen gas to diffuse into the chamber. As a result, the oxygen indicator solution in the chamber was replaced and the oxygen-scrubbing palladium catalyst was regenerated by heating it to 160 °C for two hours. Contamination from oxygen may be minimal since the crushed core samples were stored in an amber glass jar fitted with a lid, which was placed in a cabinet inside the anaerobic chamber. In order to test to see if samples were oxidized after the incident, samples DGR-4-501.76, DGR-4-667.66, DGR-4-787.78 and DGR-4-819.24 were analyzed for sulfur isotope composition. The results were compared to the previously obtained data prior to the incident for the same samples. As a result, the samples were unaffected by this incident as the obtained $\delta^{34}S$ values obtained were within similar range of previously recorded values.

3.10 Petrography of *sulfur-bearing minerals*

Images of the thin sections were taken at the University of Ottawa microprobe laboratory. Thin sections that contained anhydrite and celestine were viewed under the petrographical microscope under 2.5 and 5X magnification in cross polarized light.

Also, digital images of pyrite were captured using a JEOL 6610LV scanning electron microscope (SEM) on a backscattered electron detector (BSE) at low vacuum for uncoated samples. A brief description of pyrite morphology was recorded for each thin section. The images were captured at the 10 to 100 µm scale.

4. Results

4.1 Oxic porewater samples

Porewater leachates produced from the oxic crush-and-leach method were obtained from previous studies. Following the standard methods for the precipitation of $BaSO_4$ and whole filter combustion, the porewater sulfate samples were analyzed for $\delta^{34}S$ values are summarized below in Figure 4.1. The bulk sulfide values obtained from the analysis of pyrite was obtained from Jautzy et al., (in prep.).

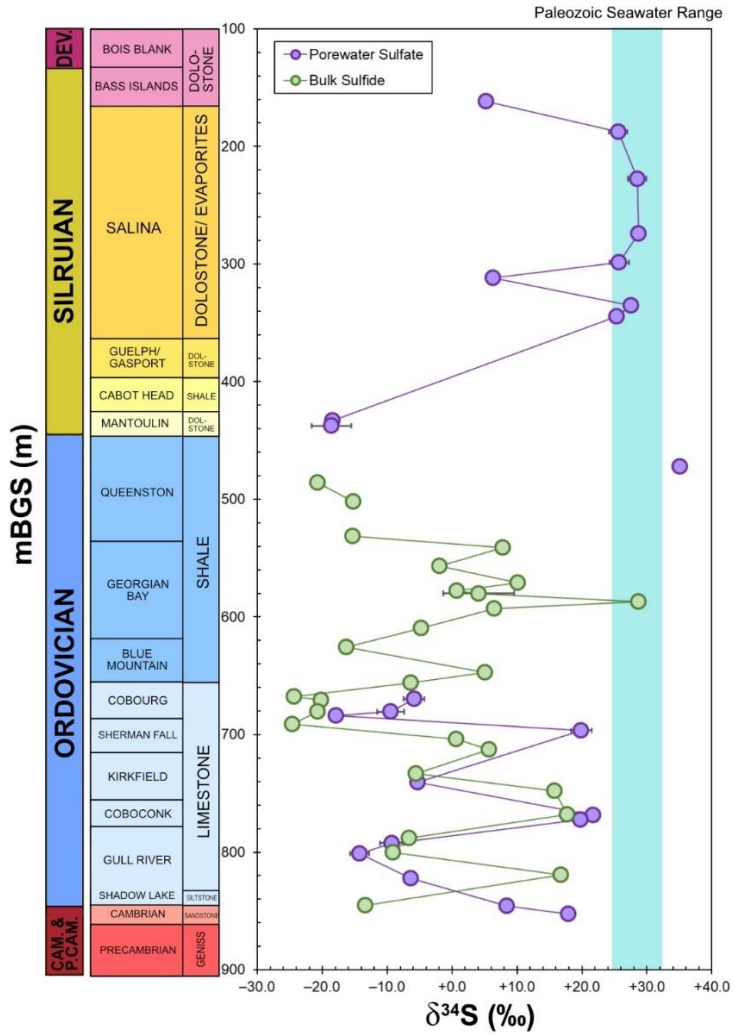

Figure 4. 1: $\delta^{34}S$ of oxic porewater sulfate versus bulk pyrite
$\delta^{34}S$ oxic porewater sulfate obtained from previous studies were compared to $\delta^{34}S$ bulk sulfide signatures as a function of depth (Jautzy et al. in prep) to illustrate the effect of sulfide oxidization. The Paleozoic seawater range is indicated by the blue bar where values range from +24 to +31 ‰ (Claypool et al., 1980; Clark and Fritz, 1997; Strauss, 2004).

The $\delta^{34}S$ porewater sulfate curves presented in Figure 4.1 were shown to generally mimic the curves of the $\delta^{34}S$ sulfide with the exception of the Gull River samples in the Cambrian sandstones. The $\delta^{34}S$ porewater sulfate values in the Silurian dolostones fell within the range of Paleozoic seawater while the two values (DGR-3-161.67 and DGR-3-311.79) had $\delta^{34}S$ values closer to +5 ‰.

4.2 Filter testing for EA-IRMS

Five different types of 25 mm diameter filters (nitrocellulose, quartz, glass, silver and nylon) were tested to see if they would induce any fractionations or blank contributions when combusted in the EA-IRMS along with a laboratory standard of $BaSO_4$. The variation in $\delta^{34}S$ values are illustrated below in Figure 4.2. Ten methodological replicates of powdered $BaSO_4$ lab standard, five replicates of each blank filters, along with the same types of filters with the $BaSO_4$ standard were analyzed. The $BaSO_4$ laboratory standard had a mean $\delta^{34}S$ value of +15.9 ‰. None of the blank filters contained any sulfur.

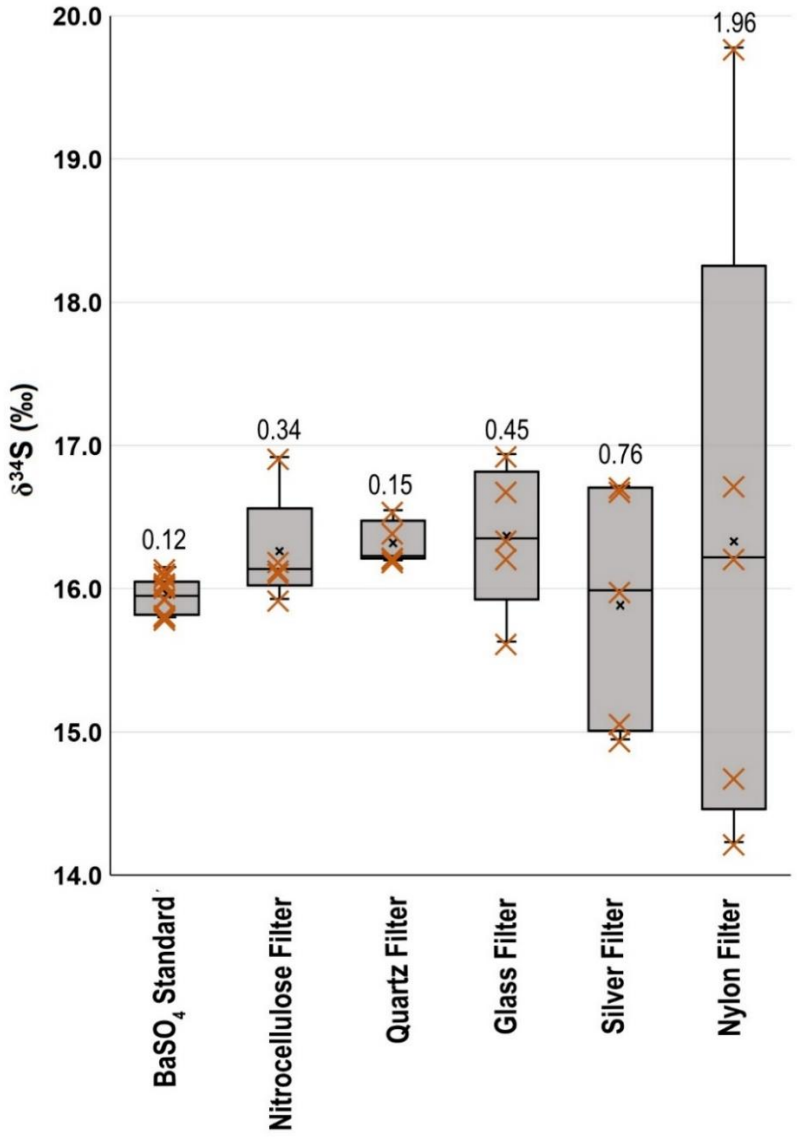

Figure 4. 2: Variation in $\delta^{34}S$ values for the different types of filter combusted along with $BaSO_4$ standard
The orange cross indicates individual $\delta^{34}S$ values for each type of filter that was combusted with the $BaSO_4$ standard on the left. The line in the middle of the histogram is the average value obtained, the black dot represents the median and the standard deviation is indicated by the values above each histogram.

The $BaSO_4$ laboratory standard had a standard deviation (STD) of 0.12. The nylon filter had the highest STD of 2.0 while quartz filter had the lowest STD of 0.2 when combusted with the $BaSO_4$ lab standard in the EA-IRMS.

4.3 The effect of grain size during leaching on the $\delta^{34}S$ signatures

Due to the limited supply of dry crushed rock samples, the potential effect of grain size on the isotopic signature of sulfur during leaching was tested. The $\delta^{34}S$ signatures obtained from leaching the same sample using a different range of grain sizes are illustrated in Figure 4.3. Each point on the graph represents a separate aliquot of porewater leachate produced by a separate portion of the granular rock that was used during leaching.

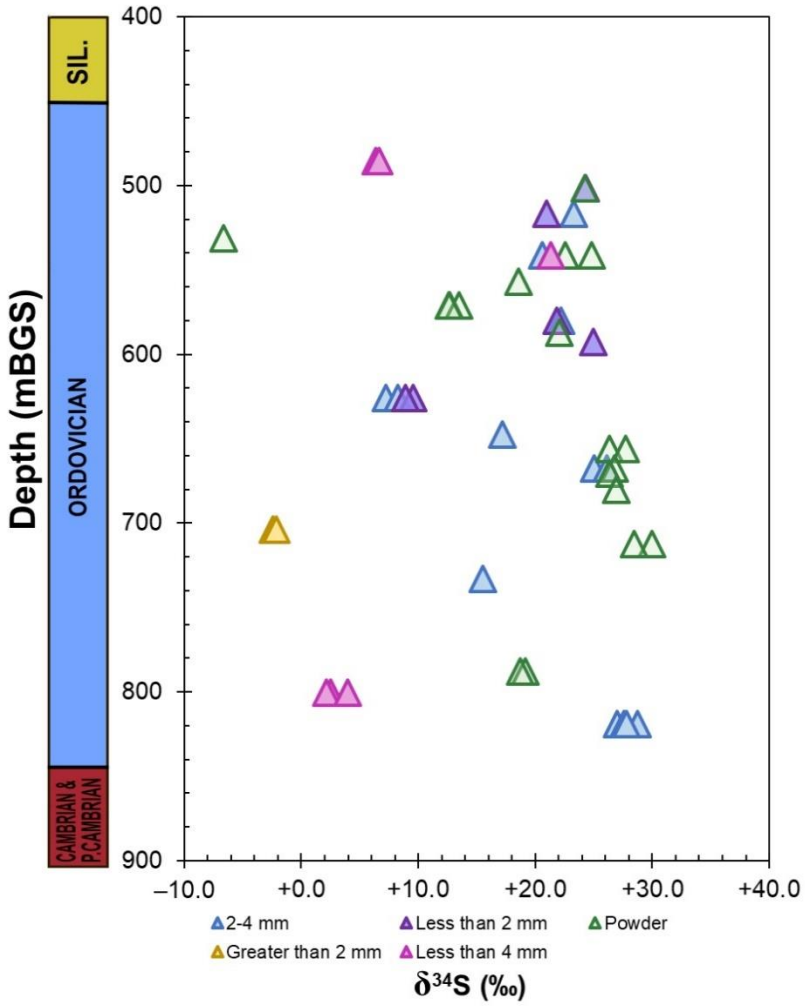

Figure 4. 3: Comparing $\delta^{34}S$ values to varying grain size during leaching
$\delta^{34}S$ signature of $BaSO_4$ as a function of depth. These are precipitated from leachates produced from varying grain sizes.

The samples DGR-4-501.76, DGR-4-541.12, DGR-4-580.04 and DGR-4-625.62 reported a STD of (0.03, 1.82, 0.2 and 1.0), which were within the normal range of STD of $\delta^{34}S$ values

that were associated with the heterogeneity of the core samples. Replicate samples with the same grain size (DGR-4-819.24 and DGR-4-800.42) resulted in an STD of 0.7 and 1.0 respectively.

4.4 Petrography of sulfur-bearing minerals

To visualize the stratigraphic distribution of sulfur-containing minerals within the Michigan Basin, the petrography of these minerals were examined. Major sulfur-containing minerals such as anhydrite, gypsum, celestine and pyrite were identified with optical and scanning electron microscope. Thin sections obtained from a previous study conducted by Petts et al., (2017) were observed under a petrographic microscope at 2.5X and 5X magnification. The occurrence of anhydrite was seen in Figure 4.4. In addition, the same thin sections were viewed on the SEM to characterize pyrite morphology. The various pyrite morphologies that are present within the Michigan Basin were summarized in Figure 4.4.1.

In terms of the distribution of the sulfur-bearing minerals within the study site, gypsum was present in Queenston, Georgian Bay, Sherman Fall and Coboconk Formations. While anhydrite was present in all formations except for Blue Mountain, Upper Cobourg, and Kirkfield Formation. Finally, pyrite was present throughout all formations. The soluble Ca-sulfate minerals were estimated to be in minor or trace quantities of less than 10% within these layers (Raven et al., 2011).

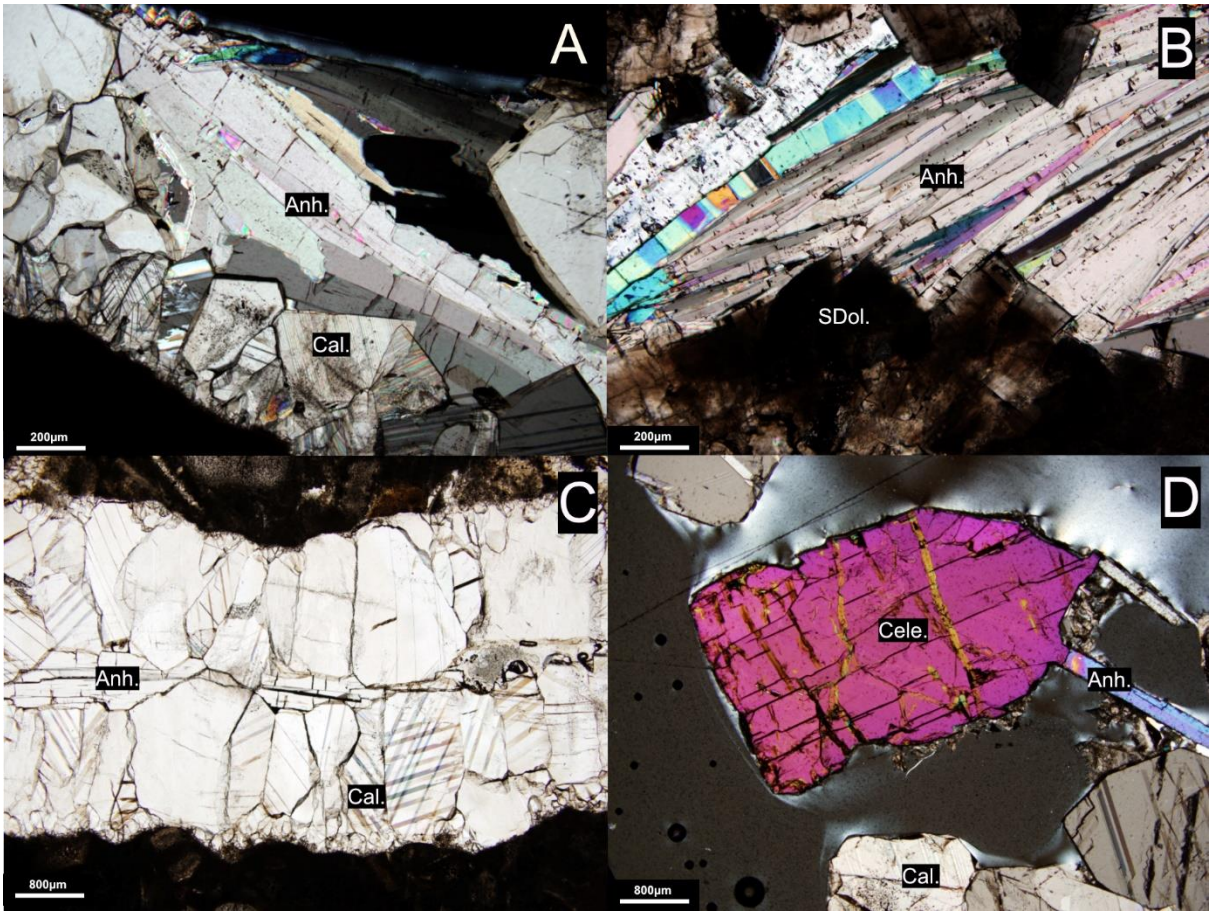

Figure 4. 4: Petrography of anhydrite and celestine
5X and 2.5X magnification viewed under a petrographic microscope. A: anhydrite infilling the calcite vein in the Ordovician shales (DGR-8-663.81); B: the growth of anhydrite associated with saddle dolomite in the Ordovician limestones (DGR-5-688.06); C: calcite vein infilled with anhydrite in the Ordovician argillaceous limestone (DGR-5-704.44); D: celestine can be seen associated with anhydrite in the Cambrian sandstones (DGR-6-864.60)

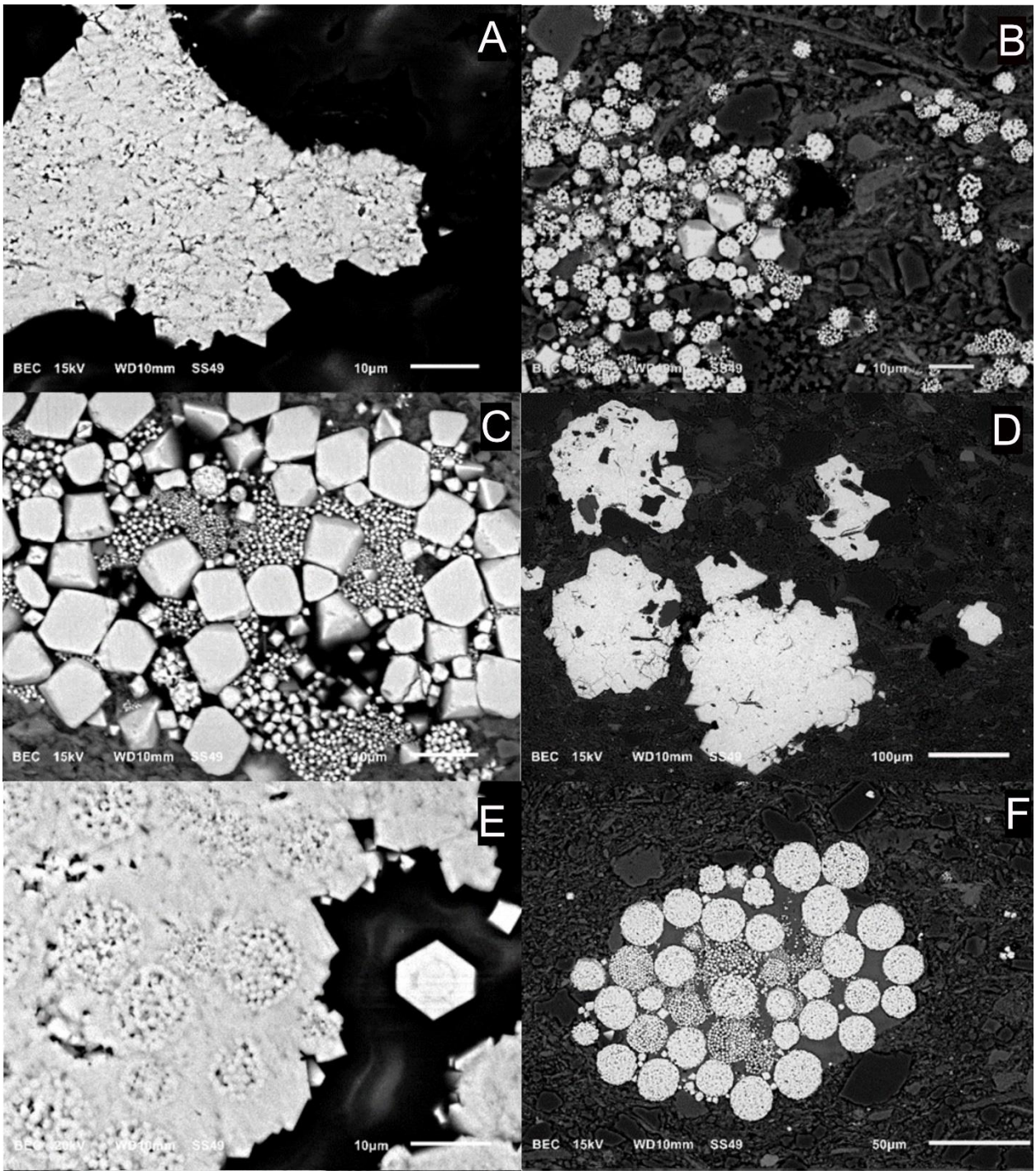
A
BEC 15kV WD10mm SS49 10µm
B
10µm
C
BEC 15kV WD10mm SS49
D
BEC 15kV WD10mm SS49 100µm
E
10µm
F
BEC 15kV WD10mm SS49 50µm

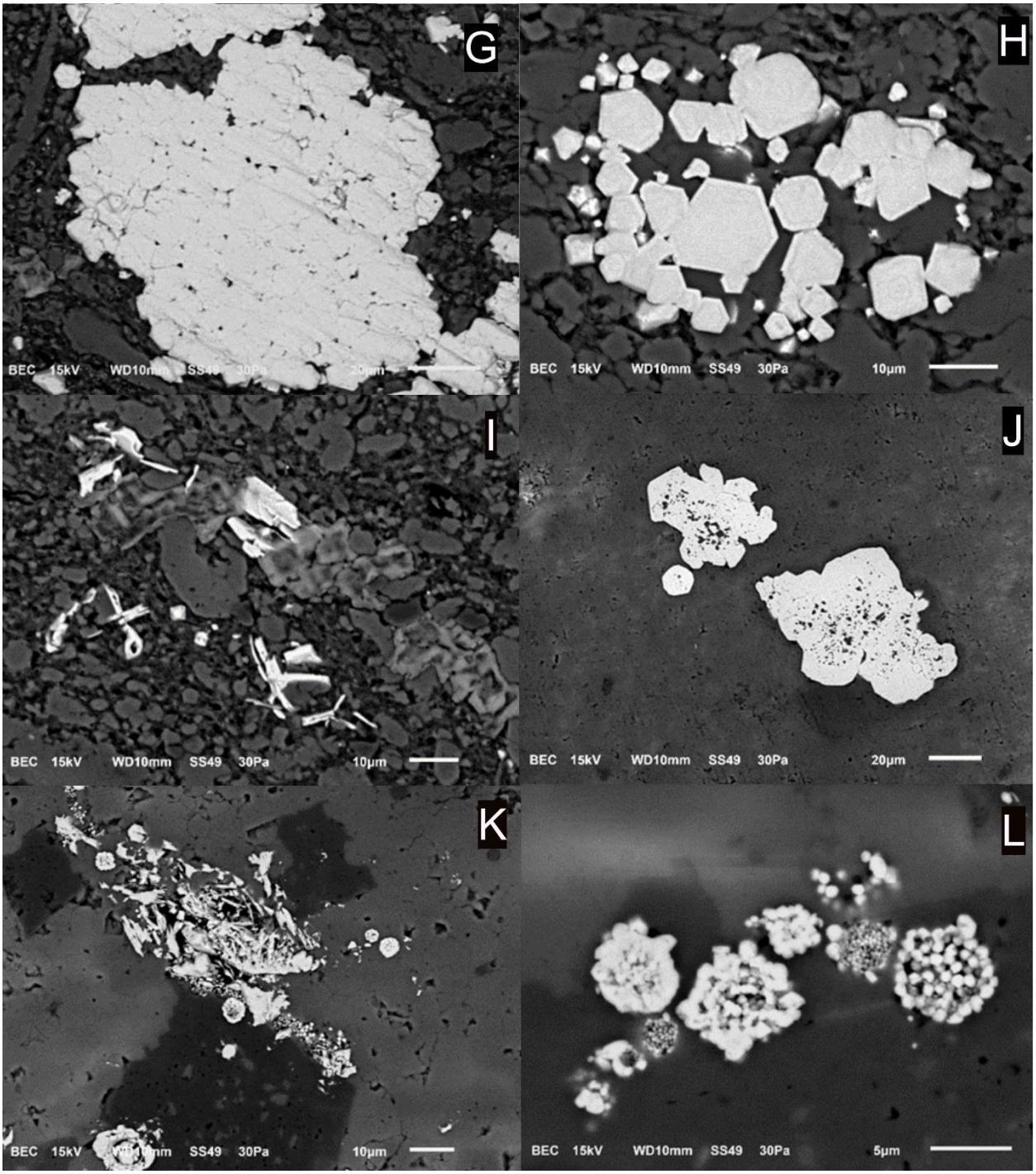

Figure 4.4. 1: SEM images of various pyrite morphologies observed
A: cemented massive cluster of pyrite with a framboidal core. and B: clusters of fine-grained framboidal pyrite mixed with fine to ultra-fine-grained euhedral pyrites (DGR-4-531.19); C: a cluster of fine to ultra-fine-grained pyrite mixed with some framboids with varying grain size and D: massive pyrite with irregular boundaries (DGR-4-541); E: massive cemented framboidal pyrite with euhedral overgrowth, F: a cluster of framboidal pyrite with varying grain sizes mixed with some fine-grained euhedral pyrite, G: massive cemented aggregates of anhedral pyrites, H: clustered euhedral to subhedral pyrite with varying grain size. Visible inner ring in euhedral pyrite. I: clusters of tabular pyrite (DGR-4-733.12); J: disseminated sub-euhedral pyrite grains with irregular boundaries (DGR-4-768.13); K: disseminated aggregates consisting of irregular tabular and framboids and L: a small cluster of framboidal pyrite with varying grain size. (DGR-4-819.24).

4.4.1 $\delta^{34}S$ signatures in anhydrite and gypsum

Gypsum and anhydrite were identified in core samples and were drilled to create powders that were used for analysis on the EA-IRMS. The average $\delta^{34}S$ values of sulfate bearing minerals and the STDs are summarized in Table 4.1 while the different sampling spots are illustrated in Figure 4.5 and the corresponding $\delta^{34}S$ values associated with the marked sampling spots are presented in Table 4.2. Most core samples were sampled at least in two different spots, some samples had twelve replicates (DGR-5-378.16) in order to check for homogeneity. However, samples: DGR-3-580.7 and DGR-3-559.95 did not have replicates due to the lack of sample availability.

Table 4. 1 $\delta^{34}S$ signatures of anhydrite and gypsum

Borehole	Corrected mBGS	Average $\delta^{34}S$ Anhydrite and Gypsum	Standard Deviation
DGR-3	207.94	27.50	0.28
DGR-4	243.44	29.72	0.67
DGR-3	248.47	29.43	0.22
DGR-3	274.38	28.01	0.54
DGR-3	298.73	30.08	0.66
DGR-5	344.59	35.89	0.89
DGR-4	469.13	20.28	1.13
DGR-3	559.95	31.84	-
DGR-3	574.93	22.72	0.60
DGR-3	580.70	23.90	-
DGR-6	686.11	37.67	0.16
DGR-6	773.65	-0.88	-

**Samples with no standard deviation value indicates there was not enough sample for more than one analysis.*

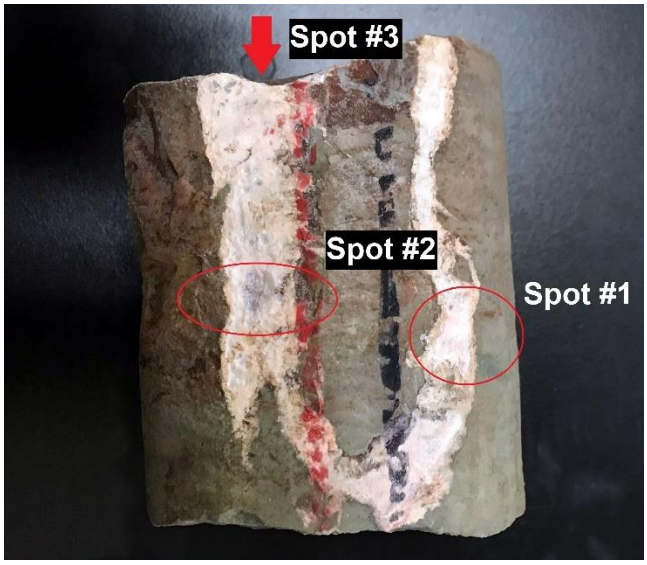

Figure 4. 5: Sampling sites of a gypsum vein for DGR-3-274.38
Three different sampling of gypsum to check for homogeneity. Spot 1 and 2 are on the side of the core while spot 3 is on the upper surface of the core.

Table 4. 2 Homogeneity of gypsum vein for DGR-3-274.38

Sampling Spot	Sample ID	$\delta^{34}S$ of Gypsum	Standard Deviation
1	DGR-3-274.38	28.85	0.5375
1	DGR-3-274.38	28.36	
2	DGR-3-274.38	27.95	
2	DGR-3-274.38	27.30	
3	DGR-3-274.38	27.69	

The STD from $\delta^{34}S$ of the Ca-sulfate minerals ranged between 0.16 to 1.13. Therefore, these veins are relatively homogenous in terms of $\delta^{34}S$ signatures. Also, these values were consistent with the values found in literature where Silurian-Devonian seawater ranged from +17 to +30 ‰ (Claypool et al., 1980; Kampschulte and Strauss, 2004; Wu et al., 2014) while Ordovician seawater ranged from +24 to +31‰ (Thode, 1970; Claypool et al., 1980; Strauss, 2004; Fike et al., 2015).

4.5 *Anaerobic chamber breach*

The four samples (DGR-4-501.76, DGR-4-819.24, DGR-4-787.78 and DGR-4-667.66), were analyzed for $\delta^{34}S$ signatures in order to check for the possible oxidation of the whole

crushed inventory. The results fell within the normal STD range when compared to previous $\delta^{34}S$ values from the same sample depth.

4.6 $\delta^{34}S$ of various sulfur species and $\delta^{18}O$ of porewater sulfate

In this section, porewater sulfate from DGR-4 core samples were analyzed for $\delta^{34}S$ and $\delta^{18}O$ signatures. The $\delta^{34}S$ of sulfur-bearing marine evaporite minerals, porewater sulfate and bulk sulfide (Jautzy et al. in prep.) are all presented together below in Figure 4.6: A. While the $\delta^{18}O$ signatures of porewater sulfate are presented in Figure 4.6: B and the porewater sulfate concentrations are presented in Figure 4.6: C.

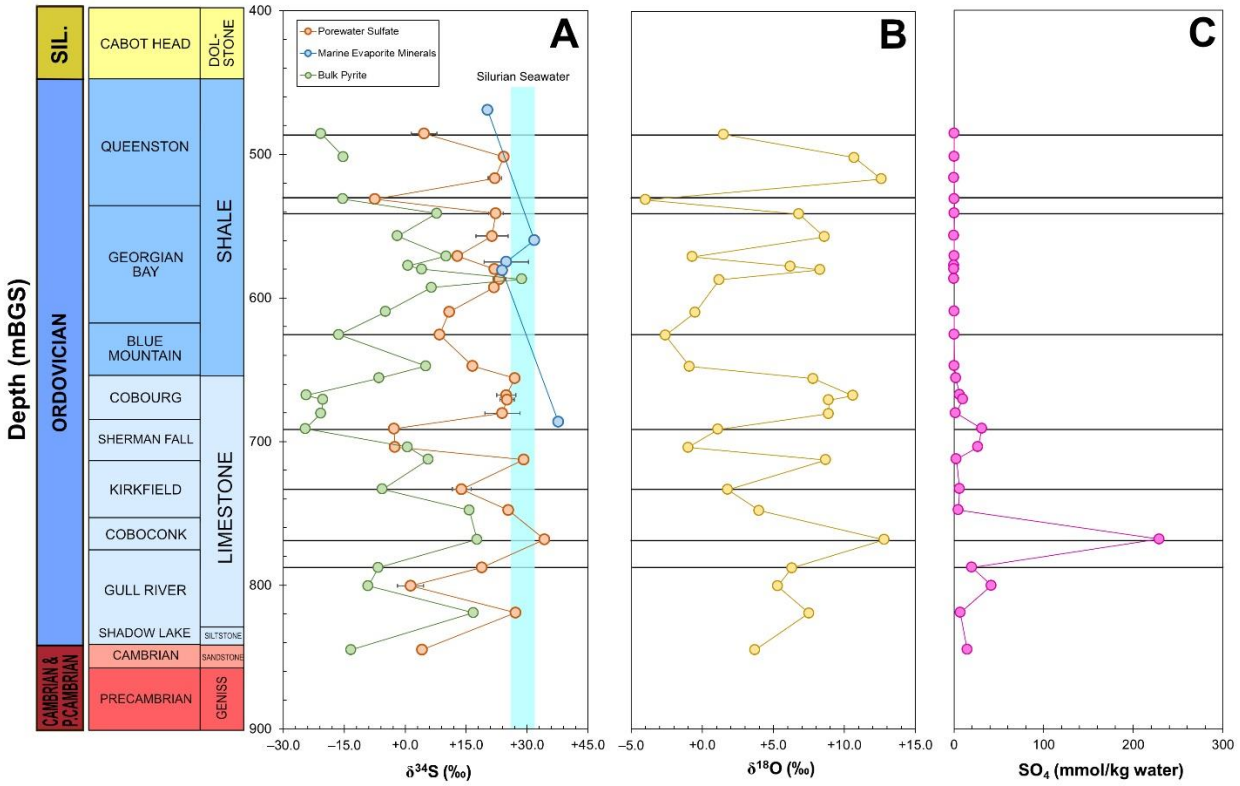

Figure 4. 6: $\delta^{34}S$ of sulfate, sulfide, marine evaporite, sulfate concentration and $\delta^{18}O$ of porewater sulfate. A: $\delta^{34}S$ of porewater sulfate and $\delta^{34}S$ of marine evaporite as a function of depth. These are average values obtained from the analysis of multiple batches of the sample. The Silurian seawater range in blue ranges from +26 to +32‰.; B: $\delta^{18}O$ of porewater sulfate; and C: sulfate concentrations are obtained from a single sample. $\delta^{34}S$ of bulk pyrite data is provided by Jautzy, et al. (in prep).

In Figure 4.6: A, the average $\delta^{34}S$ porewater sulfate values were obtained from two to five methodological replicates. Overall, both the $\delta^{34}S$ of porewater sulfate and the $\delta^{34}S$ of bulk

pyrite values fell below the marine evaporite $\delta^{34}S$ values, while generally porewater sulfate $\delta^{34}S$ values were more enriched compared to the $\delta^{34}S$ bulk sulfide. Apart from the sample DGR-4-586.93 where $\delta^{34}S$ of all three sulfur components converged close to one value and for DGR-4-703.92, the $\delta^{34}S$ of porewater was depleted with respect to the $\delta^{34}S$ of bulk sulfide. From a depth of 667.66 to 680.32 mBGS, the bulk sulfide and the porewater sulfate showed similarly mirrored curve. At depth in the Gull River formation starting at the depth of 787.78 mBGS, the curve of $\delta^{34}S$ of sulfate followed the trend of $\delta^{34}S$ bulk sulfide. However, the $\delta^{34}S$ of porewater sulfate was still relatively more enriched with respect to the $\delta^{34}S$ of the bulk sulfide.

The oxygen isotope composition of sulfate is illustrated by Figure 4.6: B. The most depleted signature occurred at the depth of 531.19 mBGS with a $\delta^{18}O$ value of −4.0 ‰ while the most enriched value occurred at the depth of 768.13 mBGS with a value of +12.8 ‰. No distinct trends were seen in the $\delta^{18}O$ porewater sulfate profile. Generally, the values of $\delta^{18}O$ porewater sulfate values tended to fluctuate from enriched values to depleted values, which ranged between −4.0 ‰ and +12.8 ‰.

The $\delta^{34}S$ of sulfate and of sulfide, along with the $\delta^{18}O$ of sulfate, generally all behaved coherently. Thus, when $\delta^{18}O$ of sulfate is enriched, it is also associated with the enriched values of $\delta^{34}S$ of sulfate and sulfide. On the other hand, when the $\delta^{18}O$ of sulfate is depleted, both $\delta^{34}S$ of sulfate and sulfide are also depleted with respect to the other values.

In Figure 4.6:C, the porewater sulfate concentrations was around 0.05 to 0.5 mmol/kgw in the Ordovician shales and porewater sulfate concentrations started to increase in the Ordovician limestones at depth of 655.83 mBGS. The highest concentration of 228.88 mmol/kgw occurred at the depth of 768.13 mBGS and eventually the porewater sulfate concentrations started to decrease with the increase in depth within the Gull River Formation.

4.6.1 The difference between $\delta^{34}S$ of porewater sulfate and $\delta^{34}S$ of bulk pyrite

The $\Delta\delta^{34}S_{SO4\text{-}pyrite}$ is illustrated in Figure 4.6.1. This was compared to the range of fractionation factors associated with bacterial SRB activity seen in sediments. This value ranged between +18 and +50 ‰ according to the studies (Canfield and Teske, 1996; Habicht and Canfield, 2001; Wortmann et al., 2001; Strauss, 2004; Pellerin et al., 2015).

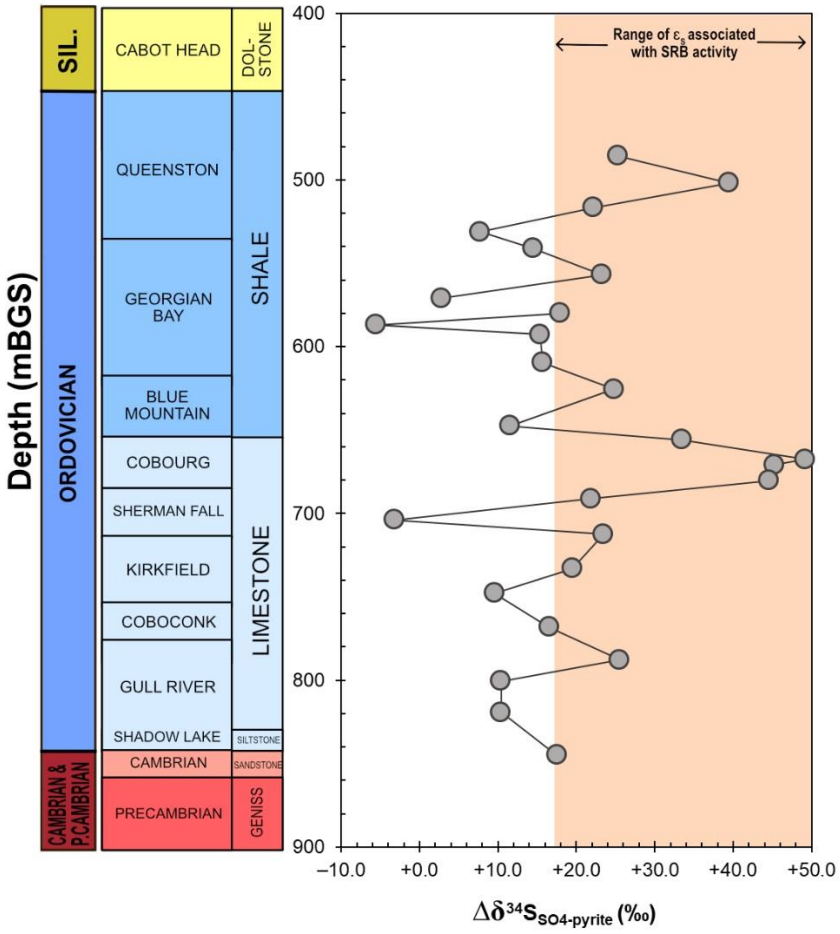

Figure 4.6. 1: The difference between $\delta^{34}S$ of porewater sulfate and $\delta^{34}S$ of bulk pyrite
$\Delta\delta^{34}S_{SO4\text{-}pyrite}$ as a function of depth. The range of the fractionation factor associated with SRBs in sediments is illustrated by the orange bar.

The biggest difference in $\delta^{34}S$ values occurred at the depth of 667.66 mBGS with a $\Delta\delta^{34}S$ value of +49.3‰. There were two samples that (DGR-4-586.92 and DGR-4-703.84) had a negative $\Delta\delta^{34}S$ values of −5.5 and −3.2 ‰. Fifteen out of twenty-seven samples were within the range of fractionation factor associated SRB activity. However, the four samples DGR-4-501.76,

DGR-4-667.77, DGR-4-670.76 and DGR-4-680.32 were the only samples that had a $\Delta\delta^{34}S$ value of around +40 ‰ while most fell within the +10 and +20 ‰ range.

4.6.2 The relationship between $\delta^{34}S$ and $\delta^{18}O$ of porewater sulfate

The $\delta^{34}S$ of porewater sulfate was plotted against the $\delta^{18}O$ of porewater sulfate in Figure 4.7 below while the different geological formation of these samples were grouped in the same color.

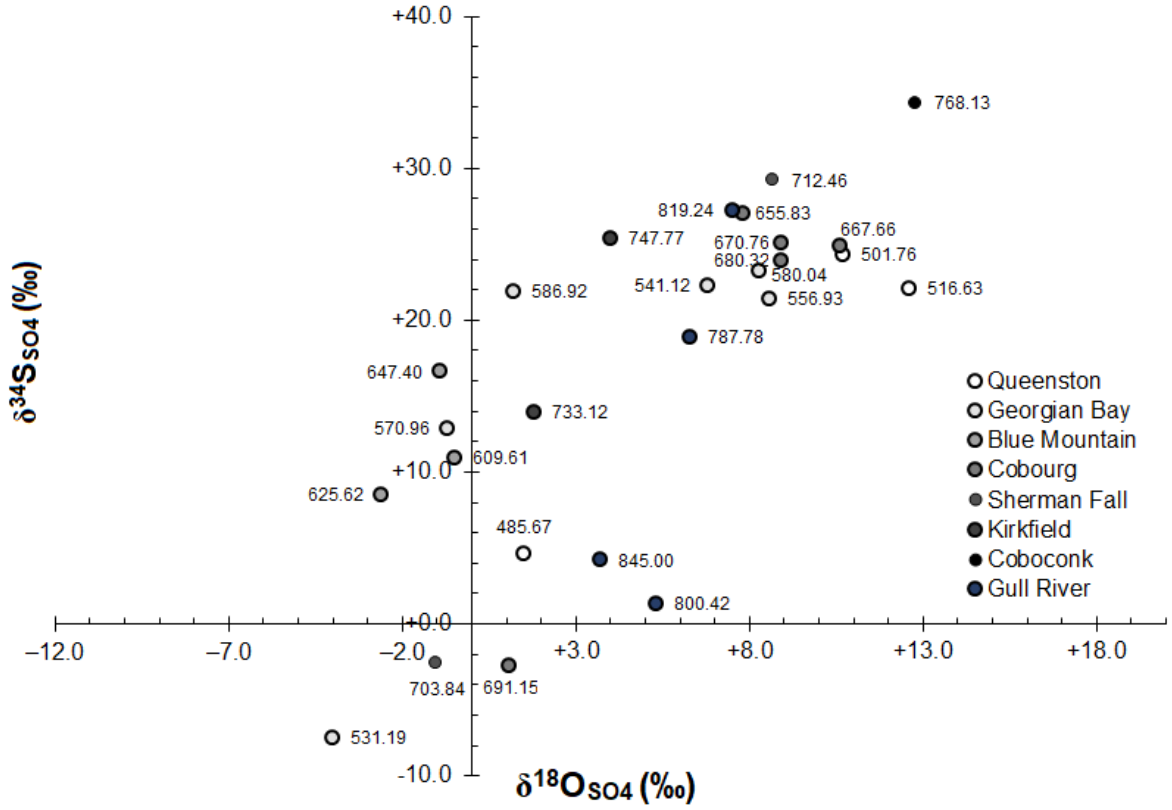

Figure 4. 7: $\delta^{34}S$ versus $\delta^{18}O$ of porewater sulfate.
The increase in depth is represented by the increased darkening of the points. The $\delta^{34}S$ values are averaged values produced as a methodological replicate. While $\delta^{18}O$ values do not contain any replicates.

At first glance, two clusters of points can be seen. The cluster on the top right and the cluster on the bottom left. Since none of the formations were clustered together, this indicated that the $\delta^{34}S$ and $\delta^{18}O$ signatures of porewater sulfate are not distinguished by the different geological formations.

4.7 *Porewater geochemistry*

Porewater was analyzed for major cations and anions. Cations (Na^+, Ca^{2+}, Sr^{2+}, total Fe and total Mn) were presented in Figure 4.8 and Figure 4.8.2 below. Anions ($Cl^-$and SO_4^{2-}) are illustrated in Figure 4.8.1. The anions Br^-, NO_3^- , NO_2^- and PO_4^{3-} were also analyzed but were below the detection limit of the DIONEX.

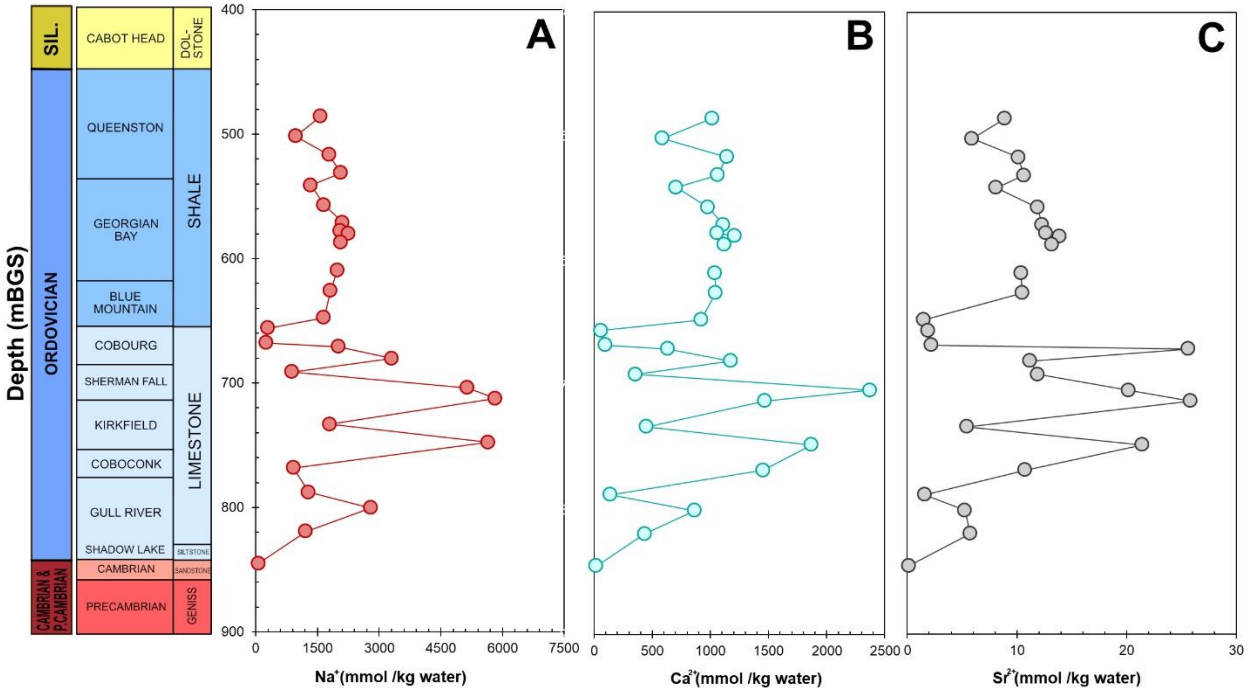

Figure 4. 8: Stratigraphic profile of various cation concentrations of the porewater.
The major cation concentrations are plotted as a function of depth. The concentration is normalized to the amount of porewater present in these layers based on porosity and wet rock density

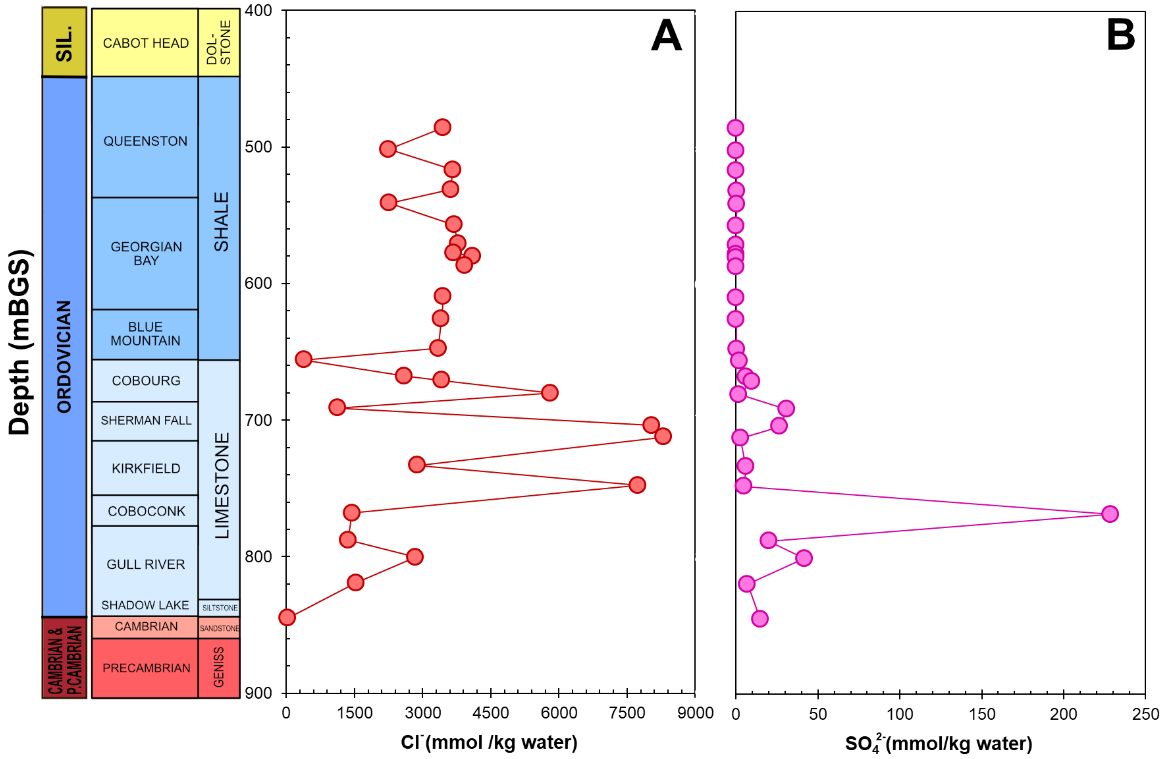

Figure 4.8. 1: Stratigraphic profile of anion concentrations of the porewater.
The two major anion concentrations are plotted as a function of depth. The concentration is normalized to the amount of porewater present in these layers based on porosity and wet rock density.

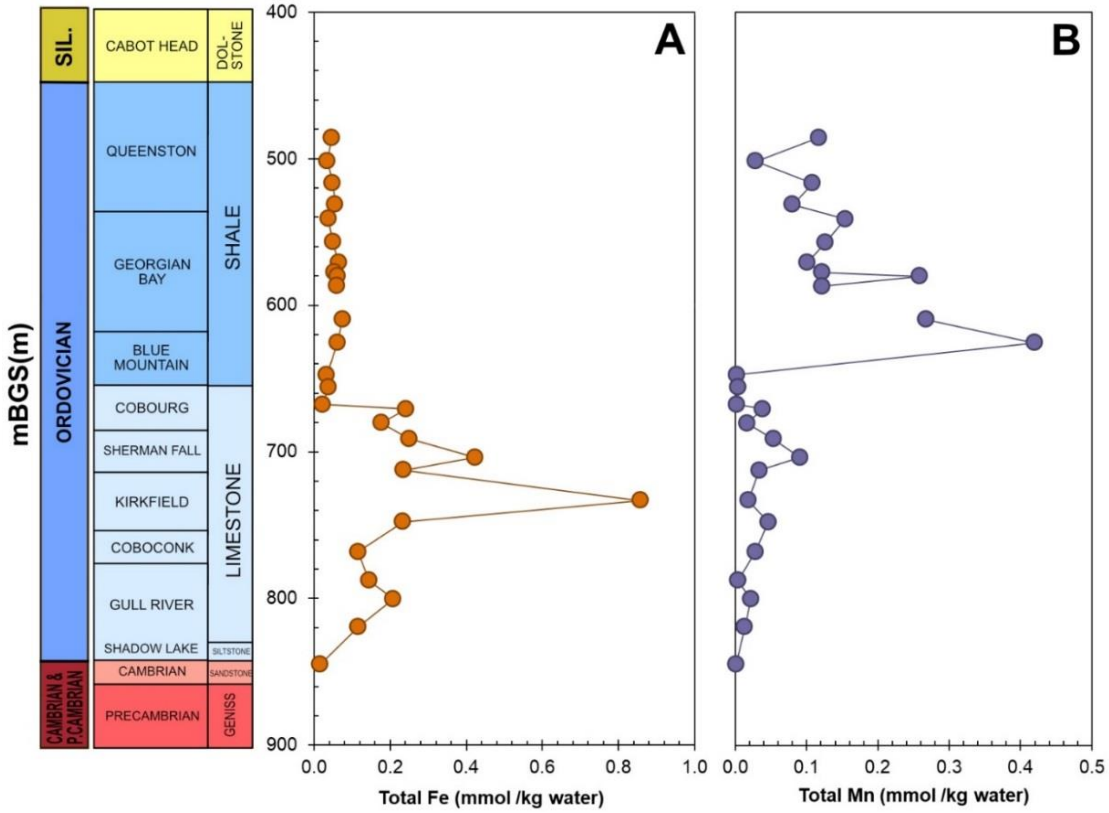

Figure 4.8. 2: Stratigraphic profile of total Fe and total Mn
The concentration is normalized to the amount of porewater present in these layers based on porosity and wet rock density.

Overall, there was an increase in concentration at a depth around the depth of 700 mBGS and a decrease in concentration around the depth of 760 mBGS for Na^{+}, Ca^{2+}, Sr^{2+}, and Cl^{-}. Total Fe increased at around the depth of 670 mBGS and decreased around the depth of 768 mBGS. Elevated concentrations of total Mn were observed from the depth of 580 to 640 mBGS.

4.7.1 Fe (III) and Mn (IV) porewater concentrations

In an attempt to visualize the stratigraphic distribution of Fe (III) and Mn (IV) in the Ordovician layers, the stratigraphic distribution of Fe (III) and Mn (IV) were presented in Figure 4.8.3. The % wt of Fe_2O_3 and MnO_2 were obtained from DGR-2 sample cores reported in previous studies by Raven et al., (2011) and Activation Laboratories Ltd., (2009).

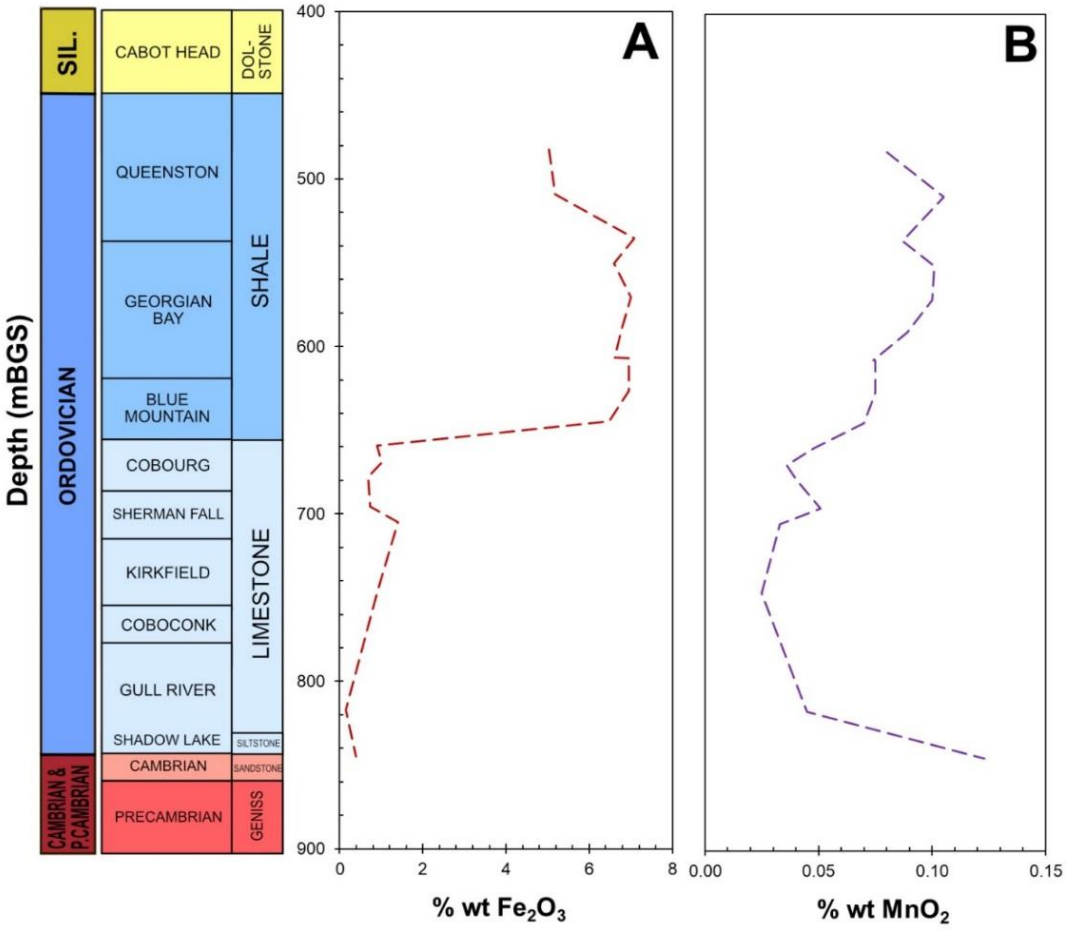

Figure 4.8. 3: % weight of Fe_2O_3 and MnO_2 in DGR-2 and DGR-2 cores
%wt of Fe_2O_3 and MnO_2 from DGR-1 and DGR-2 cores. Fe_2O_3 data is obtained from (Raven et al., 2011) and MnO_2 data is obtained from (Activation Laboratories Ltd., 2009).

The % weight (wt) of Fe_2O_3 was the highest around the depth of 480 to 660 mBGS. In contrast, the % wt of MnO_2 was the highest at around the depth of 520 mBGS, which was followed by an overall decrease until a depth of 750 mBGS. Finally, there was an increase in concentration from the depth of 760 mBGS.

5. Discussion

5.1 Oxic Porewater Sulfate Samples

In Figure 4.1, the samples at the depth of 161.63 and 311.79 mBGS have enriched values close to +30 ‰ because hydraulic conductivity is very high at these two depths. This is consistent with the presence of aquifers at those depths (Al et al., 2015).

Additionally, in Figure 4.1, contribution from pyrite oxidation during the oxic crush-and-leach method can be illustrated by the curves in the Ordovician limestones. At shallow depths in the Devonian formation (above 430 mBGS), pyrite is not as abundant as in the Ordovician, therefore pyrite oxidation has less of a contribution toward the porewater $\delta^{34}S$ signatures. With respect to the Salina Formation, anhydrite is the dominant mineral at shallow depths, this would contribute to the porewater $\delta^{34}S$ signature since the majority of the sulfate in the porewater would be from anhydrite dissolution during leaching. Therefore, the $\delta^{34}S$ values are expected to fall closer to the marine evaporite range at around +30 ‰, which is reported in Table 4.1 (Raven et al., 2011). At lower depths in the Cambrian sandstones, the $\delta^{34}S$ signatures of porewater sulfate is more difficult to interpret due to the multiple fluid events that have occurred as the original $\delta^{34}S$ porewater signatures are likely to be altered and overprinted by the last fluid event (Petts et al., 2017). Furthermore, the $\delta^{34}S$ signatures could also be affected by the heterogeneity of the large pyrite grains present in the Cambrian. During leaching, the outermost surface of the grain is captured by the fluid that comes in contact with the mineral surface. This outermost surface might have recorded only the last pyrite formation event within the altered porewater fluid.

In conclusion, the oxic graph provides a solid evidence supporting the idea that pyrite oxidation during crush-and-leach method is a major contributing factor to the $\delta^{34}S$ composition

of porewater sulfate. Since pyrite oxidation by atmospheric oxygen is a relatively fast process, core samples must be crushed and leached in an anaerobic chamber to prevent the oxidization of pyrite. Another process to be cautious of during leaching is the dissolution of Ca-sulfate minerals, which can drive the $\delta^{34}S$ signature of porewater sulfate closer to the marine evaporite values at +30 ‰.

5.2 *Filter testing for EA-IRMS*

Illustrated in Figure 4.2, the powdered $BaSO_4$ laboratory standard (n=10) had a mean $\delta^{34}S$ value of 15.9 ‰. The nylon filter (n=5) had the highest STD of 2.0 while the quartz filter had the lowest STD of 0.2. The values from the nitrocellulose filter were within the range of the $BaSO_4$ standard, excluding the one outlier out of five replicates. The quartz and glass filters contained delicate fibers that washed away during rinsing and filtering resulting in an overall negative percent recovery. In contrast, the silver filters had a layer of oxidized material after being in contact with water during filtration, which contributed percent recovery of over 100%.

Finally, nitrocellulose filters were selected to be used for the whole-filter combustion method for sulfur isotope analysis because combusting the filter with the $BaSO_4$ standard did not cause fractionation during analysis, the filters are widely available. In addition, the filters did not break down during multiple filtrations, which allowed the mass of $BaSO_4$ to be estimated prior to isotopic analysis.

5.3 *The effect of grain size during leaching on the $\delta^{34}S$ of porewater sulfate*

The sample DGR-4-541.12, was analyzed for $\delta^{34}S$ signatures from three different grain sizes (Figure 4.3). As a result, the $\delta^{34}S$ value of +23.7, +21.4 and +20.6 ‰ was obtained. An STD of 1.8 was obtained from three of these values. This falls within the range of normal STD values as a result of heterogeneity of samples. The other three samples DGR-4-501.76, DGR-4-

580.04 and DGR-4-625.62 had an STD of less than 1.0. Within the same grain size, there is minor isotopic variation in the $\delta^{34}S$ values due to the heterogeneity of the core samples. This is apparent in the sample DGR-4-712.46, which had an STD of 1.0.

In addition, the concentrations of sulfate in leachates did not vary significantly between powdered and granular samples. This could be because the 24-hour leach of these rocks had sufficient time to ensure all of the ions have been leached into solution. Therefore, the variation in grain size during leaching does not alter the $\delta^{34}S$ isotopic composition of porewater sulfate.

5.3.1 Anaerobic chamber breach

Four samples were analyzed for $\delta^{34}S$ signatures and compared to previous obtained values from the same samples. As a result, the values obtained fell within the normal range of STD of less than 2.0. This indicates that the traces of oxygen that potentially accumulated in the anaerobic chamber were not able to contaminate the crushed samples that were kept in closed amber jars.

5.4 *Petrography of sulfur-bearing minerals*

The presence of anhydrite, gypsum, celestine and pyrite has been confirmed by previous studies (Koroleva et al., 2009; Whitney and Lee, 2010; Hobbs et al., 2011; Raven et al., 2011; Petts et al., 2017). Based on images of anhydrite taken by petrographic microscope in Figure 4.7.1 anhydrite can be seen to precipitate as an infill after the formation of secondary calcite and saddle dolomite under a petrographic microscope. Saddle dolomite is shown to be lining veins and vugs within Trenton Group, while secondary calcite can be seen in Blue Mountain. Petts et al., (2017) identified six paleofluid based on petrography and stable isotopes and concluded; dolomite was formed in stage 1, calcite was formed in stage 2, anhydrite was formed in stage 3 and finally, secondary inclusions composed of mostly calcite was formed during stage four and

five. Large euhedral pyrites were formed during stage three to five at depths below the Shadow Lake Formation.

Additionally, Figure 4.4.1 presents a summary of pyrite morphologies that were identified on the SEM. Euhedral and framboidal pyrite with varying grain sizes can be seen throughout the sedimentary strata. According to the literature, there is no correlation between pyrite size distribution with respect to burial depth. In a single nucleation event, pyrite microcrystals grow at the same rate, producing crystals with the same size. Therefore, separate nucleation events occurring at different times will unlikely to produce equivalent sized microcrystals (Wilkin et al., 1996). The mixture of different grain sizes suggests that pyrite was formed during a different point in time instead of during one single event. Framboidal pyrite is likely to be formed first in highly saturated marine environments in the water column or below the sediment-water interface, while euhedral pyrite was likely to be formed at a much slower rate (Raiswell, 1982).

Framboidal pyrite with overgrowth was also identified at depth of 531.19 and 586.92 mBGS, which was also found in euxinic sediments of Green Lake (Suits and Wilkin, 1998) and also in salt marshes (Wilkin et al., 1996). Since these are texturally distinctive, it is believed to be a distinguishing feature of diagenetic pyrite (Suits and Wilkin, 1998). As framboidal aggregates settle in the sediments under the sediment-water interface, further growth can occur as overgrowths while being buried (Wilkin et al., 1996).

The presence of overgrowths, infillings, pyritic masses, large euhedral crystals are what is considered to be secondary pyrite formation. Overgrowth tend to increase with depth, the growth will continue as pyrite surfaces are exposed to a solution containing the solutes required for pyrite formation (Wilkin et al., 1996).

5.5 *Porewater geochemistry*

The geochemical profile was constructed from the porewater leachates. Cations (Na^+, Ca^{2+}, total Fe, Sr^{2+} and total Mn) and anions (SO_4^{2-} and Cl^-) concentrations were analyzed. Concentrations of Br^-, NO_3^-, NO_2^- and PO_4^{3-} were also examined but these were under the detection limit of the DIONEX. Overall, there is an increase in concentration at 700 mBGS and decrease in concentration at a depth of 760 mBGS for Na^+, Ca^{2+}, Sr^{2+}, and Cl^-. This could be from the infiltration of evaporated Silurian seawater, which brought the influx of dissolved ions into the Ordovician layers.

Porewater concentrations of anions and cations were compared with previous studies on the porewater geochemistry by Koroleva et al., (2009), Hobbs et al., (2011), Raven et al., (2011) and Murseli et al., (2017). The total Fe, and total Mn were not presented in all three studies. Na^+, Ca^{2+} and Cl^- concentrations are consistent with all three studies except Koroleva et al., (2009) reported higher Na^+ and lower Ca^{2+} concentrations. The concentration of Sr^{2+} and SO_4^{2-} are within the range of Hobbs et al., (2011) and Koroleva et al., (2009), which is likely due to similar porewater extraction methods; where samples were leached anaerobically with solid to liquid ratio of 1:1. In addition, the study by Murseli et al., (2017) reported concentrations Sr^{2+} in similar range. However, the SO_4^{2-} concentrations were higher than the concentrations reported here possibly due to the dissolution of anhydrite and gypsum as their samples were all powdered, but had different solid to liquid ratio of 1:4. The concentrations of Sr^{2+} and SO_4^{2-} were much lower than the concentrations reported by Raven et al., (2011). The differences in geochemical concentrations are mainly due to the difference in the extraction method used. In the study by Koroleva et al., (2009), they leached granular samples for 48 hours, while most of the other studies leached samples for 24 hours or less. In addition, the studies also used a different grain

size and a different solid to liquid ratio. The difference in grain size affects the surface area on the grains that are available for the displacement of ions. Meanwhile, the solid to liquid ratio influences the concentration gradient created by the aqueous solution, which is associated with the change in ionic strength within the fluid.

Divalent cations such as Ca^{2+} tend to displace monovalent cations such as Na^{+} and K^{+} from exchange sites on the surface of the clay minerals as the ionic strength is decreased in the DI solution during leaching (Koroleva et al., 2009; Celejewski et al., 2014). Therefore, some of the Na^{+} in the leachates may be from the exchange sites leading to increased concentrations of Na^{+}. However, the cation exchange capacity tends to be low in these rocks (2 to 40 meq/kg rock), thus the increase in the concentration of divalent cation concentrations tend to be negligible (Koroleva et al., 2009).

Although total Mn concentration was not presented in previous studies, typical seawater and groundwater concentrations for total Mn are 0.015 and 0.0002 ppm, therefore the concentrations presented here are higher than typical values (Clark, 2015a). The potential cause for elevated ion concentrations could be due to the infiltration of the Silurian sea which brought down an influx of evaporated seawater into the Ordovician shale and limestone.

5.6 S-isotope of porewater sulfate

There are three general sources of sulfate that contribute to the $\delta^{34}S$ porewater sulfate signatures. Anhydrite and gypsum dissolution (celestine at lower depth), residual sulfate after partial reduction and recycled sulfate from the re-oxidization. This can occur abiotically or biotically in the presence of Fe (III) and Mn (IV) dissolved in solution (Nordstrom et al., 2007). Our initial hypothesis is illustrated in Figure 5.1 below. This was based on pyrite morphology, the $\delta^{34}S$ of bulk pyrite (Jautzy et al., in prep.) and fractionation factor associated with microbial

sulfate reduction in natural populations ranges from +18 to +45 ‰ (Strauss, 2004), assuming that the $\delta^{34}S$ isotopic signatures of porewater sulfate and sulfide was preserved after the closure of the sedimentary system.

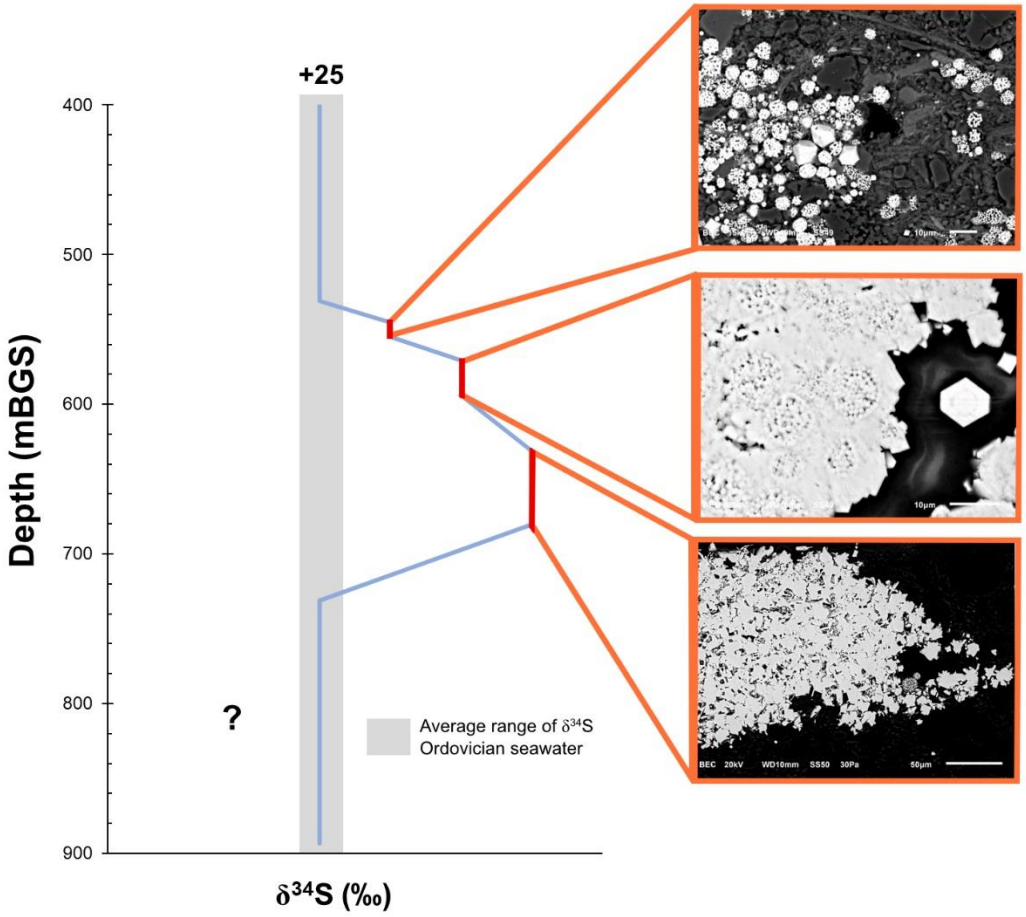

Figure 5. 1: Expected values for $\delta^{34}S$ porewater sulfate

Bulk sulfide pyrite at the depth of 531.19 mBGS was moderately depleted in $\delta^{34}S$ signatures relative to Ordovician seawater. Just below that depth, at 586.92 mBGS, the framboidal pyrite with euhedral overgrowth are associated with $\delta^{34}S$ signatures similar to Ordovician seawater. Finally, the tabular pyrite that can be seen at a depth of 670 mBGS had the most depleted $\delta^{34}S$ values. At the depth of the Cambrian sandstones, it is harder to predict the $\delta^{34}S$ value because multiple fluid events have occurred at this depth, which has potentially

overprinted the $\delta^{34}S$ records through the different fluid event. As the $\delta^{34}S$ signature is a result of a mixture of different fluids, it proves to be challenging when identifying the source of the porewater sulfate.

It was speculated that the $\delta^{34}S$ porewater sulfate and $\delta^{34}S$ of pyrite could be correlated to some extent as these two are linked in the sulfur cycle. Based on whether the system was either closed or open at the time of pyrite formation. The $\delta^{34}S$ of porewater sulfate is expected to be more enriched with respect to marine evaporite $\delta^{34}S$ signatures if bacterial sulfate reduction has occurred in a closed system. On the other hand, if bacterial sulfate reduction occurred in an open system, the $\delta^{34}S$ of porewater sulfate would fall closer to the $\delta^{34}S$ marine evaporite value because a constant supply of sulfate acts as an unlimited reservoir. In contrast, the sulfide is generally expected to be depleted in $\delta^{34}S$ with respect to the sulfate pool and the seawater in both open and closed systems. Sulfide is only expected to be enriched in $\delta^{34}S$ in the case of a closed system where it becomes increasingly enriched due to Rayleigh-type fractionation.

With sulfur isotope data alone (Figure 4.6: A), two potential conclusions can be drawn. First, bacterial sulfate reduction occurred at the depth of 586.92 mBGS as all the values converges toward marine seawater indicative of a late possible closed system. The sulfate pool is isotopically altered towards heavier $\delta^{34}S$ signatures inducing the formation of pyrite with heavier $\delta^{34}S$ signatures as well.

Second, according to Figure 4.6.1 the difference between $\delta^{34}S$ of porewater sulfate and $\delta^{34}S$ bulk pyrite at depth of 667.67 to 680.32 mBGS are between +44.6 to +49.3 ‰. This depletion in sulfide $\delta^{34}S$ values is associated with a mirrored enrichment in sulfate $\delta^{34}S$ values lower than the marine evaporite values. These values are also not associated with an elevated

concentration of sulfate (Figure 4.6) or total sulfur (Figure 5.1) and do not have a Ca: SO_4 ratio of 0.6 to 1.1 (Figure 5.2.2), meaning that the Ca-sulfate mineral dissolution is not the main contributor to the porewater sulfate at these depths. While, this could suggest possible evidence of bacterial sulfate reduction that may have occurred during an open system below the sediment-water interface, the unusual tabular morphology of the pyrite aggregates requires more investigation to support this interpretation.

Additionally, at the depth of 501.76 mBGS, the difference between porewater sulfate and bulk sulfide is +39.5 ‰ and are associated with the presence of framboidal pyrite, potentially suggesting a microbial signature.

Although examining the $\delta^{34}S$ porewater sulfate values together with the $\delta^{34}S$ bulk sulfide values can provide some information, the complexity of a time transgressive system such as the Ordovician aquiclude must be recognized. The porewater sulfate and sulfide isotopic signatures compared in this study may not be recording the same process as initially predicted. The porewater sulfate may be recording the $\delta^{34}S$ composition after it was modified by the Silurian evaporated brines that infiltrated these layers. The wide range of pyrite morphology further suggest that there is a wide range of geochemical reactions that have occurred over the geological time.

While the interpretation of the $\delta^{34}S$ porewater sulfate values together with the $\delta^{34}S$ can provide information, one has to keep in mind of the complexity of a time transgressive system such as this aquiclude. Concurrent sulfates and sulfides isotopic signatures may not be recording the same processes. The sulfate in porewaters may be recording the $\delta^{34}S$ composition after it was overprinted by the infiltration of Silurian brines. The range of pyrite morphology seen

throughout the sedimentary strata is also another indicator that there are a wide range of geochemical reactions that have occurred over geological time.

In terms of variation within the same core samples, there are minor variations in the $\delta^{34}S$ values. This is illustrated by the error bars in Figure 4.6, likely due to the heterogeneity of the samples. The $\delta^{34}S$ may differ due to the variation in mineral composition within these rocks and the possibility of microenvironments in these layers. Each sample had at least two methodological replicates to ensure the reliability of the method. Separate aliquots of leachates were produced from at least two portions of 30 g samples. Therefore, the $\delta^{34}S$ signatures presented in this study are represented by at least 60 g of samples produced from separate batches of the sample.

5.6.1 *$\delta^{34}S$ signatures marine evaporites*

Figure 4.5 illustrates the areas that were sampled on sample DGR-3-274.38 while Table 4.2 reports the $\delta^{34}S$ values obtained from each sample. The results indicate the veins of sulfate-bearing minerals are homogenous in terms of $\delta^{34}S$ signatures as average STD of 0.57. Also, the $\delta^{34}S$ of marine evaporite minerals are within the reported range of +24 to +31 ‰ (Claypool et al., 1980; Strauss, 1997; Fike et al., 2015) supporting their usefulness as S-isotopic proxy of past marine conditions.

5.6.2 Ca-sulfate mineral dissolution

Based on the $\delta^{34}S$ profile alone, it was initially hypothesized that porewater $\delta^{34}S$ signatures are highly affected by the $\delta^{34}S$ of anhydrite and gypsum because the sulfate concentrations obtained from anoxic porewater extraction were higher than what was expected. Anhydrite and gypsum dissolution was a prominent issue encountered during leaching in previous studies of DGR-2 (Koroleva et al., 2009), DGR-3 and DGR-4 (Hobbs et al., 2011) and

DGR-8 core samples (Murseli et al., 2017). During porewater extraction, the equilibrium between the minerals phase and porewater is disrupted when the DI water creates a high concentration gradient between the mineral phases and the liquid phase during leaching, which in turn is extracting not only porewater solutes but also creating artefacts during leaching from mineral dissolution.

The solubility of gypsum in pure water follows first order kinetic equation at 20°C and is 1.531g/L, which is 140 times lower than NaCl. Anhydrite follows second-order kinetic equation at 3.5 g/L (Klimchouk, 1996). Additionally, James and Lupton, (1978) investigated the solubility of gypsum and anhydrite where the dissolution rate of gypsum plateaus at 2.5 kg/m^3 after just one hour, while anhydrite's concentrations increased to 1.5 kg/m^3 after four hours, indicating a steady increase in concentration over time. Because these are kinetic reactions, the composition of the leachate will depend on the amount of time the rock is in contact with the water (Koroleva et al., 2009). The rate of dissolution of these two minerals is also affected by grain size. The solubility increases with a decrease in grain size due to the increased surface area in contact with water. The diffusion gradient created by solid to liquid ratio will also affect the solubility due to the decreased ionic strength of the solution.

The overall average water to rock ratio during leaching in this study is 1.043, with ratios ranging from 0.80 to 1.3. The gradient was kept relatively constant during leaching, which eliminates the possibility of leaching certain samples faster than others. Koroleva et al., (2009) tested various solid to liquid ratios during 48-hour leach and have determined that a 1:1 ratio yields the most consistent results in terms of geochemical concentration. In addition, they have also examined the saturation indices (SI) of various minerals shown in Figure 5.2. In general, the

SI of gypsum and celestite falls below 0 indicating mineral dissolution, aside from gypsum being saturated at the depth of 523.05 to 562.92 mBGS.

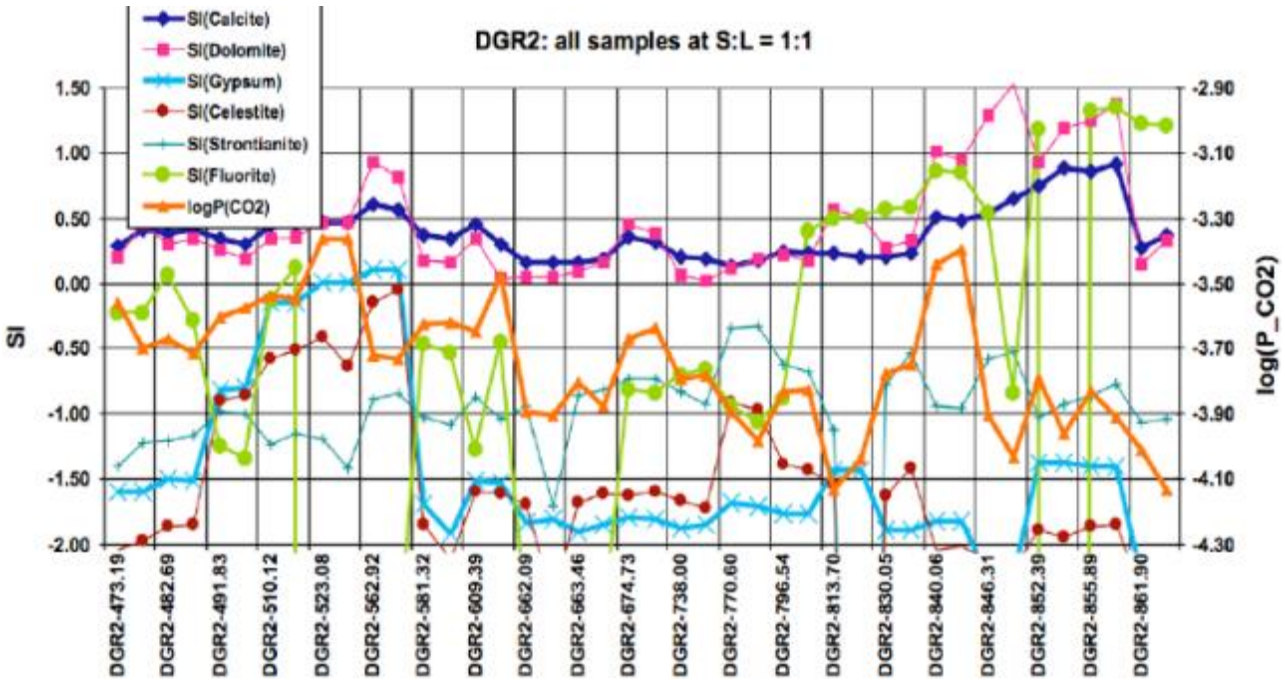

Figure 5. 2: Calculated saturation indices of various minerals.
Modified from Koroleva et al., (2009), saturation index was calculated from PHREEQC for 1:1 solid to liquid aqueous extraction of porewaters.

If the soluble Ca-sulfates are contributing to the porewater sulfate, the $\delta^{34}S$ and $\delta^{18}O$ composition of these minerals must be understood. Figure 2.3, modified from (Clark and Fritz, 1997), illustrates the $\delta^{34}S$ and $\delta^{18}O$ composition of marine sulfate throughout geological time. The $\delta^{34}S$ of marine sulfate ranges between +26 to +32 ‰ for Ordovician while Silurian ranges from +27 to +31 ‰. Typical $\delta^{18}O$ of marine sulfate ranges from about +11 to +17.5 ‰ for Ordovician and Silurian ranges from +12 to +18 ‰. This information defines the range of $\delta^{34}S$ and $\delta^{18}O$ values that are likely to be affected by the mineral dissolution of anhydrite and gypsum. If the majority of the sulfate in the porewaters came from marine evaporites, then we would expect the $\delta^{18}O$ of sulfate to be close to +10 to +16 ‰ uniformly throughout the depth. However, this is not the case as some values are low as −4.0 ‰ at depth of 531.19 mBGS in Figure 4.6.

The solid to liquid ratio is calculated from dividing the amount of DI water used for leaching by the amount of dry rock used in order to further identify samples that may have been affected by Ca-sulfate mineral dissolution. The trend line intercepting at zero illustrates the linear relationship between sulfate concentration and the solid to liquid ratio during leaching. If the sole source of sulfate originates from the porewater then a linear relationship can be seen. This is because if the amount of crushed sample is used during leaching increases, a subsequent increase in porewater sulfate concentration should be seen in the leachates.

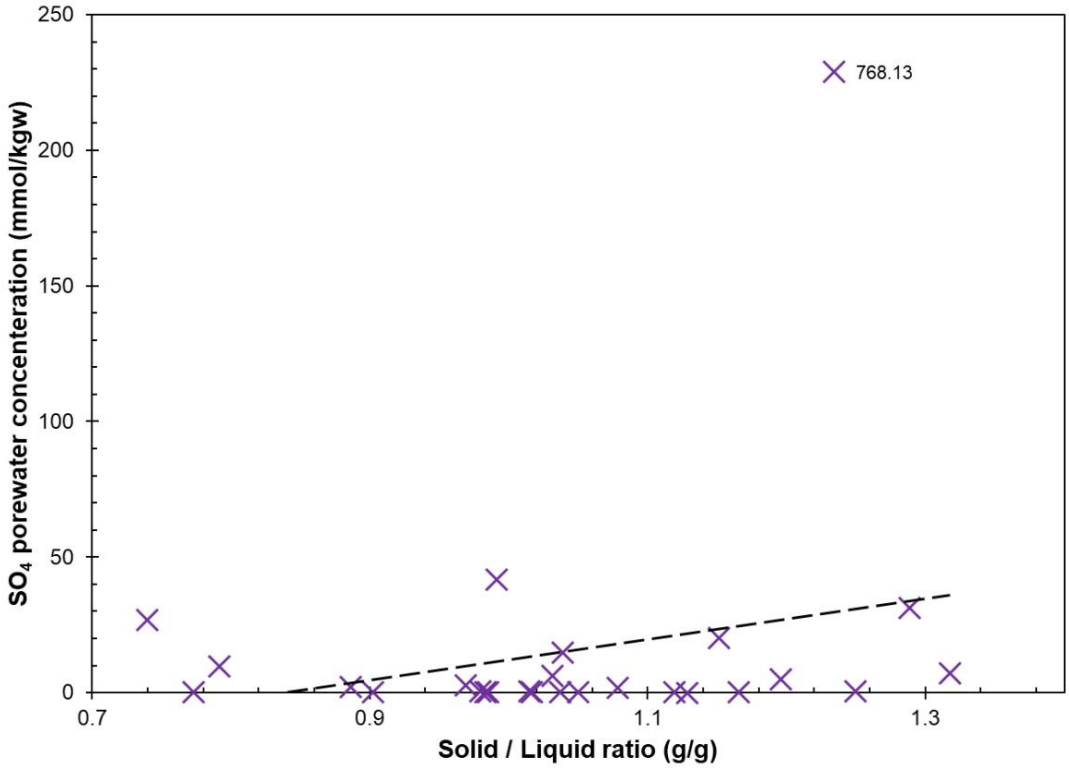

Figure 5.2. 1: Solid to liquid ratio as a function of porewater SO_4 concentrations

No linear trends can be seen between porewater sulfate concentrations and solid to liquid ratio indicating that there may be more than one source of sulfate contributing to these porewaters. The sample DGR-4-768.13 can be seen plotting very far away from the rest of the points

The millimolar ratio of Ca: SO_4 is calculated and plotted against the 1:1 line for Ca: SO_4 in Figure 5.2.2 and Figure 5.2.3 below to identify samples that may have been affected by Ca-sulfate mineral dissolution.

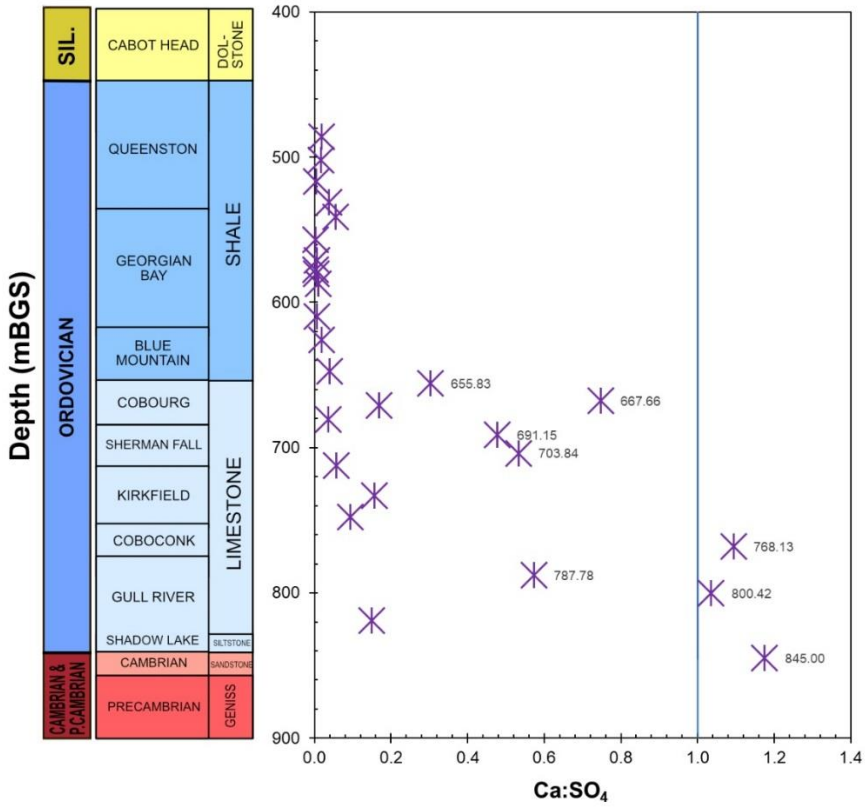

Figure 5.2. 2: Ca: SO_4 versus depth
Ca:SO_4 of 1:1 are expected if anhydrite or gypsum dissolution has occurred during leaching (Nordstrom et al., 2007; Hobbs et al., 2011). The 1:1 ratio is indicated by the blue line.

There are two factors that may have influenced the ratio of Ca and SO_4. First, the dolomitization that occurred in later stages within Ordovician layers (Raven et al., 2011; Petts et al., 2017) and may be the cause for the increase in Ca: SO_4 ratios that are seen in Figure 5.2.2, pushing values towards the right of the graph. During this process, Ca^{2+} is displaced into the porewater because dolomite ($MgCa(CO_3)_2$), is formed with two moles of calcite ($CaCO_3$) and one mole of Mg^{2+}. The Mg^{2+} replaces one if the Ca^{2+} present in calcite. As a result, one mole of Ca^{2+} is released into the porewater. This could explain the elevated Ca^{2+} concentrations within the porewater when compared to sulfate concentrations. Therefore, Ca-sulfate mineral

dissolution might not be contributing to porewater sulfate as expected, because the elevated Ca^{2+} concentration from dolomitization might be pushing some of the Ca: SO_4 ratios values closer to 1.

Second, the concentration of the various ions in the porewater leachate is affected by the final ionic strength of the leachate during leaching. The ionic strength of the leachate cannot be simplified to the ionic strength of the DI water, as the high ionic strength (highly saline, evaporated Silurian seawater) of the *in-situ* must also be considered. Therefore, the final ionic strength after equilibrium in the leachate is a mixture of the porewater plus the ionic strength of the DI water, which will depend on the ionic strength of the two solutions and the volumes of each solution.

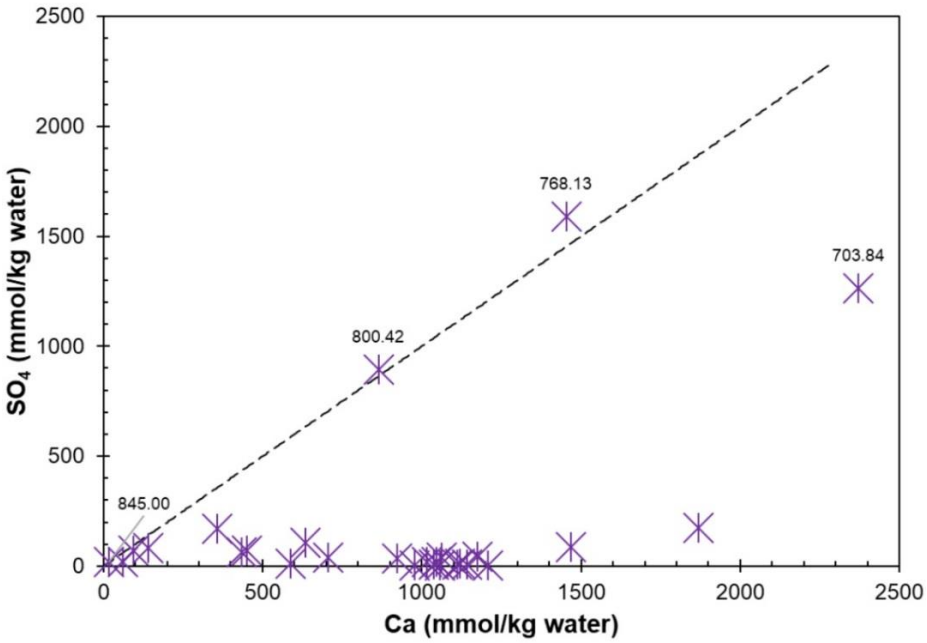

Figure 5.2. 3: Sulfate concentration plotted against calcium concentration
Concentration of SO_4^{2-} plotted against Ca^{2+} in mmol/kgw compared to a 1:1 ratio illustrated by the dashed line. Ca:SO_4 of 1:1 are expected if anhydrite or gypsum dissolution has occurred during leaching (Nordstrom et al., 2007; Hobbs et al., 2011).

Samples that plotted between Ca:SO_4 millimolar ratio of 0.6 to 1.0 suggest potential Ca-sulfate mineral dissolution. The ratios increase at around a depth of 655.83 mBGS, similar to the

increase in other major ions. According to Figure 5.2.2, Gull River samples have generally high $Ca:SO_4$ ratio while most samples from the Ordovician shales have relatively low ratios of around 0.005. The sample DGR-4-768.13 especially, had elevated porewater sulfate concentrations that was consistent with previous studies (Koroleva et al., 2009; Hobbs et al., 2011). This sample has a sulfate concentration of 9.33 mmol /kgw with an associated $\delta^{34}S$ value of +34.26 ‰, very close to the $\delta^{34}S$ marine evaporite range. In addition, the same sample plots close to the 1:1 ratio line. The samples of Gull River are also associated with elevated Ca: SO_4 ratios because anhydrite and celestine was found in the Cambrian formations (Petts et al., 2017). The highest Ca: SO_4 ratio is demonstrated by the sample within the Gull River formation, DGR-4-845.00 mBGS with a ratio of 1.18.

In an effort to further identify samples that are potentially affected by calcite dissolution, the $\delta^{34}S$ of porewater sulfate are compared to the Ca: SO_4 ratio millimolar ratio similar to what was done in Nordstrom et al., (2007) in Figure 5.2.4 below.

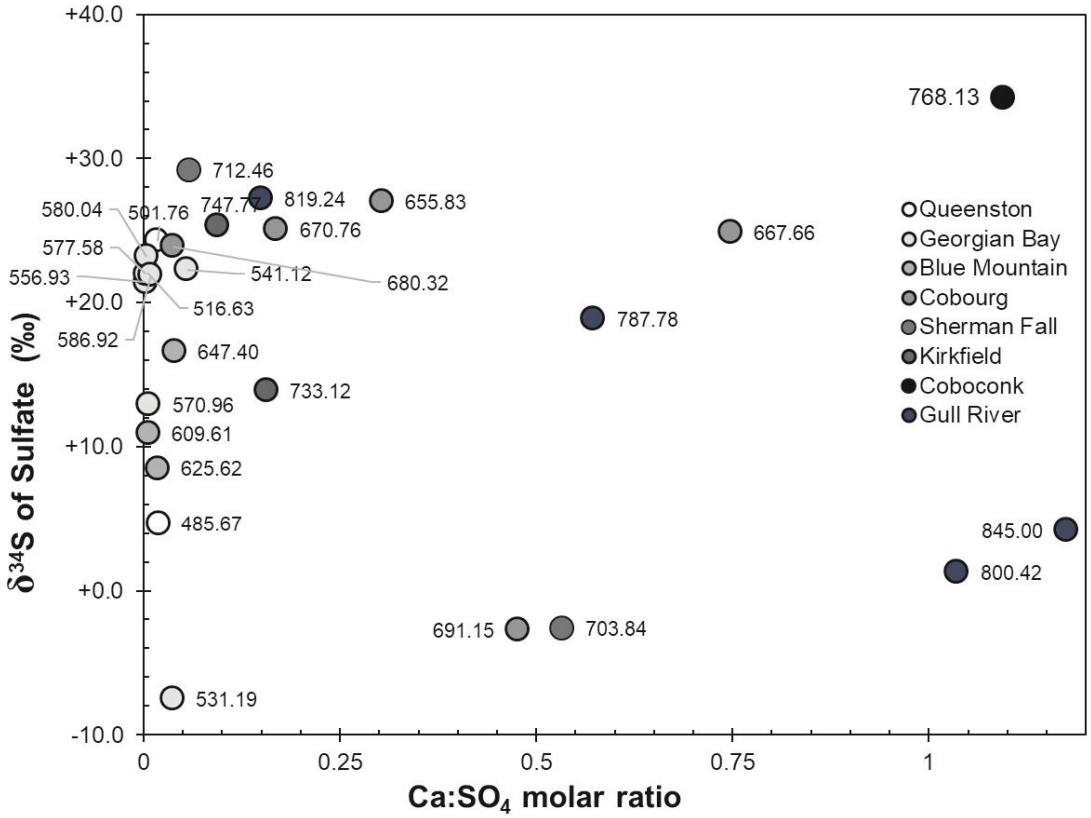

Figure 5.2. 4:$\delta^{34}S_{SO4}$ plotted against the Ca:SO_4 millimolar ratio

In this study, there is a wider range in $\delta^{34}S$ values, and no values plotted beyond the Ca: SO_4 ratio of 1.17 compared to a similar graph presented in Nordstrom et al., (2007). The wide range of values is observed because the Michigan Basin is significantly more mature system compared to their study site. Due to the maturity of the Michigan Basin, a wider range of events may have occurred during the hundreds of million years, which have likely produced varying $\delta^{34}S$ values depending on the evolutionary history within each layer. There are no values beyond the ratio of 1.5, therefore indicates calcite dissolution did not occur in these samples according to their study.

Samples that are affected by Ca-sulfate mineral dissolution will likely be plotting near the top right of Figure 5.2.4 because those samples would be associated with elevated Ca: SO_4 ratios and $\delta^{34}S$ values around +30 ‰ are associated with marine evaporite mineral $\delta^{34}S$ values.

Although majority of the samples are enriched at around +30 ‰ in Figure 5.2.4, their Ca: SO_4 ratios are close to zero. This means the enriched $\delta^{34}S$ signatures are not as a result of Ca-sulfate minerals dissolution.

5.7 *O-isotope of porewater sulfate*

To fully understand the oxygen isotope results, the various reactions that affect the porewater sulfate oxygen isotope composition from either experimental procedures or *in-situ* during the evolution of the sedimentary system must be differentiated. The three reactions that may have had a potential effect on the $\delta^{18}O$ of porewater sulfate signatures during the experimental procedure are; 1) anhydrite and gypsum dissolution and, 2) sulfide oxidation during leaching and 3) equilibrium between water and sulfate during the acidification step.

In contrast, the two *in-situ* potential reactions from the environment are: 1) dissolution of anhydrite and gypsum in the porewaters; 2) *in-situ* oxidation of sulfide minerals. The first reaction is the dissolution of anhydrite and gypsum that occurs within the *in-situ* porewater in the Michigan Basin. The second reaction, *in-situ* sulfide oxidation is a more complex reaction that is affected by multiple parameters such as the different sources of oxygen from the surrounding environment, pH, biotic or abiotic pathways, and the presence of Fe (III) or Mn (IV). Details of these reactions will be explained in the subsections below.

Figure 5.3 below presents $\delta^{34}S_{SO4}$ and $\delta^{18}O_{SO4}$ values and ranges of values in an attempt to visualize any potential trends. If the samples were affected by pyrite oxidation by atmospheric oxygen during sample analysis, the $\delta^{18}O_{SO4}$ would be close to the −11 ‰. Whereas, if equilibrium between sulfate and the surrounding water has been established during the acidification step, the $\delta^{18}O_{SO4}$ would be around +17 ‰ as the fractionation factor between

$\delta^{18}O_{SO4}$ and $\delta^{18}O_{H2O}$ is +28.7 ‰ at 25℃ (Clark, 2015b) and the DI water at University of Ottawa has a $\delta^{18}O$ of −11 ‰.

The range of bulk $\delta^{34}S$ pyrite values are obtained from Jautzy et al. (in prep.), where the highest value of +28.7 ‰ is omitted as this value is from pyrite a sample with heterogeneous pyrite morphologies likely recording a mixture of different events. The $\delta^{34}S$ range of marine evaporate minerals are obtained from the values from Table 4.1.

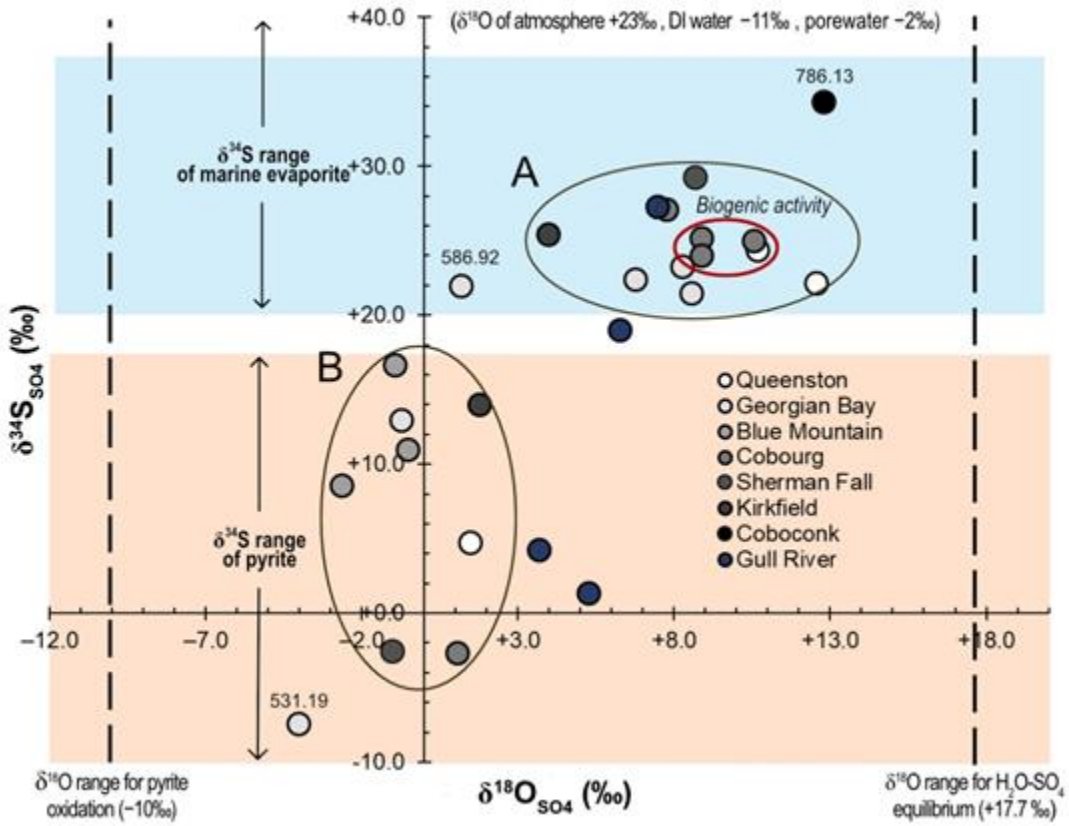

Figure 5. 3: Relationship between $\delta^{34}S_{SO4}$ and $\delta^{18}O_{SO4}$
The increased in depth can be visualized by the darkening of the circles. The range of $\delta^{34}S$ of bulk pyrite is from data provided by Jautzy et al. (in prep). The range omits the highest value of +28.7 ‰ due to the complex formation history at this depth. The $\delta^{34}S$ range of marine evaporites are determined from evaporite mineral signatures reported from this study ranges from +20.3 to +37.7 ‰. The red circle suggests the four samples that capture biogenic sulfate reduction activity.

Two distinct groups of values can be seen denoted by group A and B in Figure 5.3. Group A is within the $\delta^{34}S$ range of marine evaporate minerals and group B is within the $\delta^{34}S$ range of pyrite obtained from Jautzy et al. (in prep.). The samples that are outside of the two

distinct groups are; sample DGR-4-531.19, that had the most depleted value in terms of both $\delta^{34}S$ and $\delta^{18}O$ porewater sulfate values; sample DGR-4-786.13 had the most enriched $\delta^{34}S$ and $\delta^{18}O$ porewater sulfate values and; sample DGR-4-586.92 plots in an area between group A and B. Meanwhile the two Gull River samples stratigraphically just above the Cambrian sandstones generally do not follow the trends of other Ordovician samples.

5.7.1 Experimental factors affecting the $\delta^{18}O_{SO4}$ composition

The three possible reactions that may have occurred during sample preparation are: 1) Ca-sulfate dissolution; 2) pyrite oxidation; and 3) equilibrium between H_2O and SO_4^{2-} Reaction 1 and 2 are reactions that may take place during leaching, while reaction 3 may occur during the precipitation step. Ca-sulfate dissolution was already discussed in previous section; therefore, it will not be discussed in this section.

5.7.1.1 Sulfide oxidation during sample preparation

The separation of group A and B in Figure 4.5 indicate that not all samples are affected by the same process. If sulfide oxidation was the dominant reaction that occurred during leaching, then all samples would appear to be clustered together. According to Figure 5.3, if all the oxygen participated in the oxidation of sulfides came from atmospheric oxygen instead of the oxygen from the surrounding water, the resulting $\delta^{18}O_{SO4}$ would be around −10 ‰. Whereas $\delta^{34}S$ of porewater sulfate would have $\delta^{34}S$ values mirroring closely the $\delta^{34}S$ pyrite values seen in Figure 4.1 produced from previous oxic porewater samples.

By plotting the theoretical values in Figure 5.3, the range of expected values from the full atmospheric oxidation of sulfide can be seen plotted on the far-left side of the y-axis. All of the $\delta^{18}O_{SO4}$ values presented in this study are above −4 ‰.

In addition, to further support the idea that sulfide oxidation did not occur during sample preparation, % sulfide is compared to % sulfate. If sulfide oxidation occurred during sample analysis, then % sulfate would be expected to be greater than % sulfide. In other words, the majority of the sulfide would have been converted into sulfate during oxidation of sulfide minerals. The % S Total, % sulfide and % sulfate is illustrated by Figure 5.3.1 below.

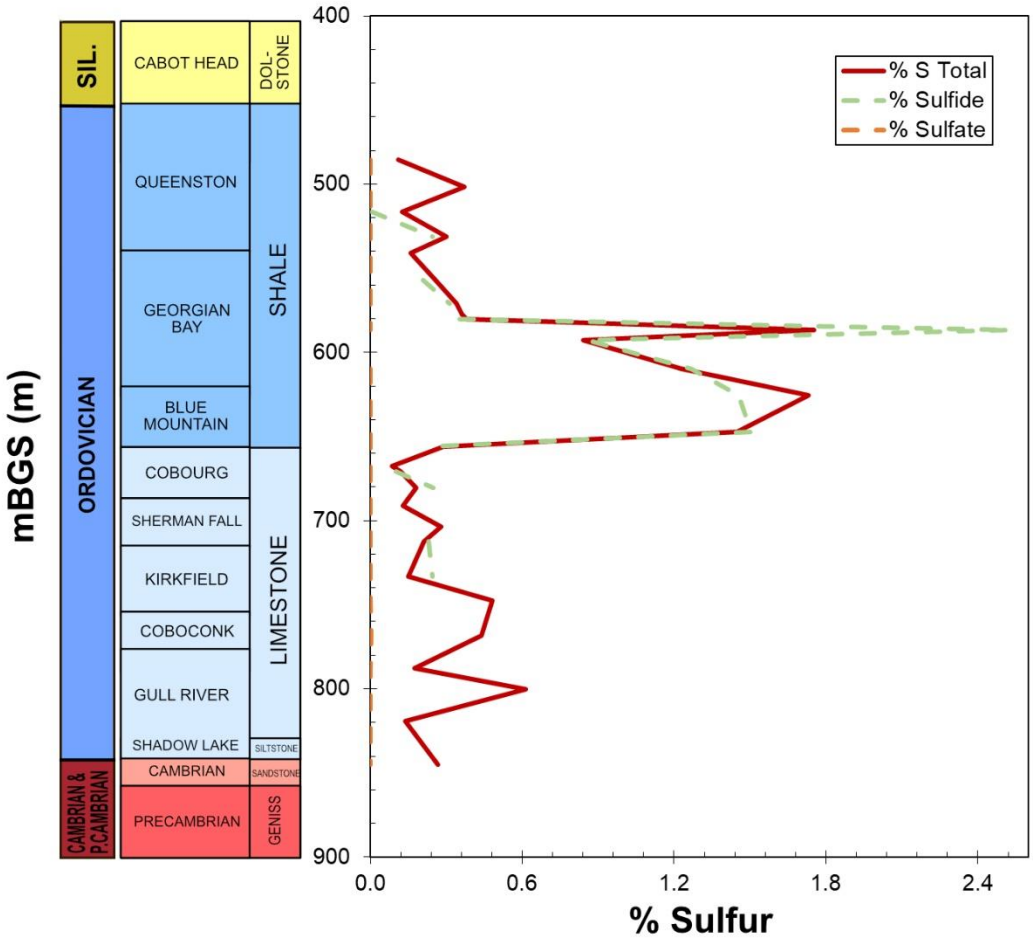

Figure 5.3. 1: The % S total, % sulfide and % sulfate for per gram of rock

The % S total and % sulfide is obtained from Jautzy et al. (in prep). The % sulfide is greater than % total S in some parts of the graph because of material loss during the acidification step according to their study. The % sulfate is significantly lower (indicated by the orange

dashed line) compared to both % sulfide and % S total. Therefore, sulfide oxidation during porewater extraction can be ruled out as a potential effect on the oxygen isotope signatures.

5.7.1.2 Equilibrium between $\delta^{18}O_{SO4}$ and $\delta^{18}O_{H2O}$

As stated previously, under normal environmental conditions (neutral pH and 25℃), the oxygen in sulfate undergo extremely slow isotopic exchange with ^{18}O of water, unless extremely high temperatures or extremely low pH are reached (Turchyn and Schrag, 2004; Antler et al., 2013; Müller et al., 2013b; Markovic et al., 2016). However, during the acidifications step prior to the precipitation of $BaSO_4$, it may have been possible for the oxygen isotope to exchange with the surrounding water as the pH was brought down to 3 to 4. Assuming this phenomenon has occurred, the fractionation factor between $\delta^{18}O_{SO4}$ and $\delta^{18}O_{H2O}$ is +28.7 ‰ at 25℃ (Clark, 2015b) and the DI water at University of Ottawa has a $\delta^{18}O$ of −11 ‰ therefore, the $\delta^{18}O$ of sulfate would be expected to be around +17.7 ‰. This assumed range is illustrated in Figure 5.3 by the dashed lines and consequently, none of the values obtained from this study are within the range of the theoretical values. Thus, it is also unlikely that this reaction took place during sample preparation.

5.7.2.1. in-situ Ca-sulfate mineral dissolution

The increased ionic strength due to the high salinity of the *in-situ* porewater would decrease the solubility of minerals such as anhydrite and gypsum. In addition, presence of dissolved species such as calcium or sulfate present in the porewater would further decrease the solubility of these minerals since the common ion effect pushes the chemical equilibrium toward the reactants, forming mineral precipitates. If we assume that the measured porewater high salinity and concentration of major ions is representative of the evaporated Silurian seawater that

infiltrated the sedimentary strata, *in-situ* dissolution of Ca-sulfate minerals would be highly unlikely (Koroleva et al., 2009).

5.7.2.2. in-situ sulfide oxidation

The presence of iron and manganese within Ordovician bedrocks is shown in Figure 4.8.3. Although the concentration of Fe (III) and Mn (IV) has not been properly quantified, the data obtained previously is sufficient to support the presence of these species. As mentioned above, pyrite can also be oxidized by Fe (III) or Mn (IV) in the absence of oxygen via surface adsorption reaction. However, this would only occur either at a very slow rate, as the solubility of Fe_2O_3 and MnO_2 is very low or if these minerals were in contact for surface reactions to occur (Schipper and Jorgenson, 2001). Since the Michigan Basin is a very ancient system, sulfide oxidation could have occurred at a very slow rate over the hundreds of million years.

The oxygen that participates in this reaction originates from water rather than dissolved oxygen (Heidel and Tichomirowa, 2011). The source of iron in these layers may originate from chalcopyrite and sphalerite in minor amounts, but also pyrite with the help of MnO_2 via surface reactions (Raven et al., 2011).

While most of the studies conducted on sulfide oxidation focus on low pH conditions associated with acid mine drainage (Taylor et al., 1984; Nordstrom et al., 2007), sulfide oxidation can also occur at circumneutral pH (Moses and Herman, 1991). The pH of the porewaters is estimated from DGR-1 and DGR-2 (Raven et al., 2011) are between 5 and 6. Although the solubility of Fe (III) decreases with increasing pH due to the precipitation of Fe (III) hydroxide species, even at low concentrations and pH between 3 to 9, Fe (III) can still oxidize pyrite without the presence of dissolved oxygen (Moses et al., 1987).

It is also possible for MnO_2 to anaerobically oxidize pyrite into sulfate at a pH of 8 in the absence of Fe (III) according to Schippers and Jorgensen, (2001), with its limitations explained in the previous section. According to Figure 4.8.3, the concentration of Mn (IV) and Fe (III) are the highest at the depth of 480 to 650 mBGS, while both Mn (IV) and Fe (III) concentrations decreases down the core, Mn (IV) starts to increase again at the depth of 800 mBGS in the Gull River Formation. In the case where there is Fe (III) in the system, Fe (III) is still the dominant oxidizing agent while MnO_2 indirectly oxidizes pyrite by converting Fe (II) to Fe (III) via electron shuttle system. This allows the continuation of sulfide oxidation in these layers when oxygen is absent.

The depth with high Fe (III) and Mn (IV) concentration seen in Figure 4.8.3 was not consistent with the grouping of A or B in Figure 5.3. Therefore, further investigation of these redox species may be required in future studies.

Sulfide oxidation can either occur abiotically or biotically via a multistep process, involving the transfer of seven electrons (Taylor et al., 1984; Van Stempvoort and Krouse, 1994). Where, one or more of the steps can be facilitated by microbial activity (Taylor et al., 1984). The oxygen isotopic composition of sulfate is a mixture of the oxygen from the water and the atmosphere and the range of $\delta\,^{18}O_{SO4}$ associated with sulfide oxidation is calculated from the isotope mass balance equation [3]. Where, fractionation factors of $\varepsilon^{18}O_{SO4\text{-}O2}$ and $\varepsilon^{18}O_{SO4\text{-}H2O}$ are considered. The calculated values are presented along with porewater $\delta^{18}O_{SO4}$ and $\delta^{18}O_{H2O}$ to potentially identify samples that are either affected by sulfide oxidation. Where, the $\delta^{18}O_{H2O}$ is a mixture of DI water (−11 ‰) and porewater (−2 ‰), with a mixing ratio from 0 to 100% for DI water. The $\varepsilon_{SO4\text{-}H2O}$ is +2.3 ‰ (Heidel and Tichomirowa, 2011) and $\varepsilon_{SO4\text{-}O2}$ is −10.8‰ (Balci et al., 2007). The fraction of water that participates during sulfide oxidation ranges 50 to 100%.

And finally, the $\delta^{18}O_{atmosphere}$ is +23 ‰ (Clark and Fritz, 1997). The range possible of $\delta^{18}O_{SO4}$ values is illustrated by the horizontal lines in Figure 5.4 below. The $\delta^{18}O_{H2O}$ of porewater values are obtained from the previous study by Murseli et al., (2017). The core samples from the previous study are from a different set of core samples so the $\delta^{18}O_{H2O}$ of porewater values were estimated based on the value at the closest depth obtained from the DGR-4 and DGR-3 cores.

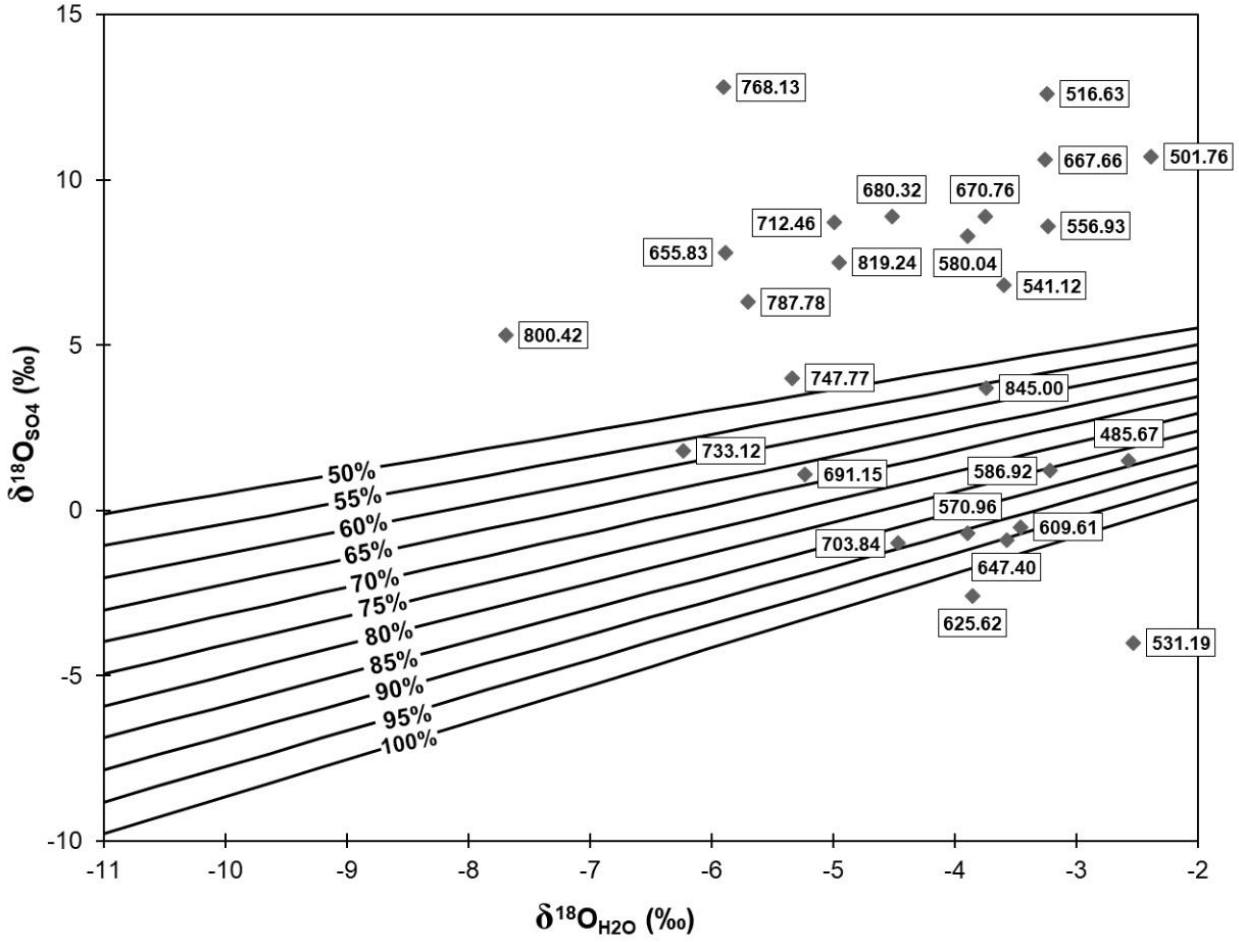

Figure 5. 4: $\delta^{18}O_{SO4}$ values plotted against $\delta^{18}O_{H2O}$ of porewater
$\delta^{18}O_{H2O}$ of porewater values are obtained from similar depth (Murseli et al., 2017). The range of sulfide oxidation is calculated from the equation [3] by Van Everdingen and Krouse, (1985).

The values obtained from abiotic and biotic sulfide oxidation from pre-existing studies resulted in similar $\delta^{18}O$ values because the fractionation factors $\varepsilon^{18}O_{SO4\text{-}O2}$ and $\varepsilon^{18}O_{SO4\text{-}H2O}$ do not vary greatly. As Table 2.1 summarizes the oxygen isotope fractionation during oxidation of sulfide minerals, the various studies have shown that it is nearly indistinguishable between

abiotic and biotic sulfide oxidation (Balci et al., 2007; Thurston et al., 2010). The range of porewater $\delta^{18}O_{H2O}$ reported by Murseli et al., (2017) is consistent with the range of $\delta^{18}O$ values of Ordovician seawater in Figure 2.3 (Clark and Fritz, 1997).

There are nine samples that are within the range of theoretical sulfide oxidation in Figure 5.4 and the samples DGR-4-625.62 and DGR-4-531.19 are the only two that fall below the sulfide oxidation range. The rest of the sample plots above the 50% line on the upper right portion graph. Although DGR-4-800.42 is significantly more depleted (−7.7 ‰) in terms of $\delta^{18}O_{H2O}$ porewater signatures, none of the values are close to the $\delta^{18}O_{H2O}$ of DI water (−11 ‰).

The samples that fall within and below the calculated $\delta^{18}O_{SO4}$ sulfide oxidation range are highlighted in Figure 5.4.1 below, to illustrate potential trends in the $\delta^{34}S$ and $\delta^{18}O$ of porewater sulfate graph from Figure 4.6.

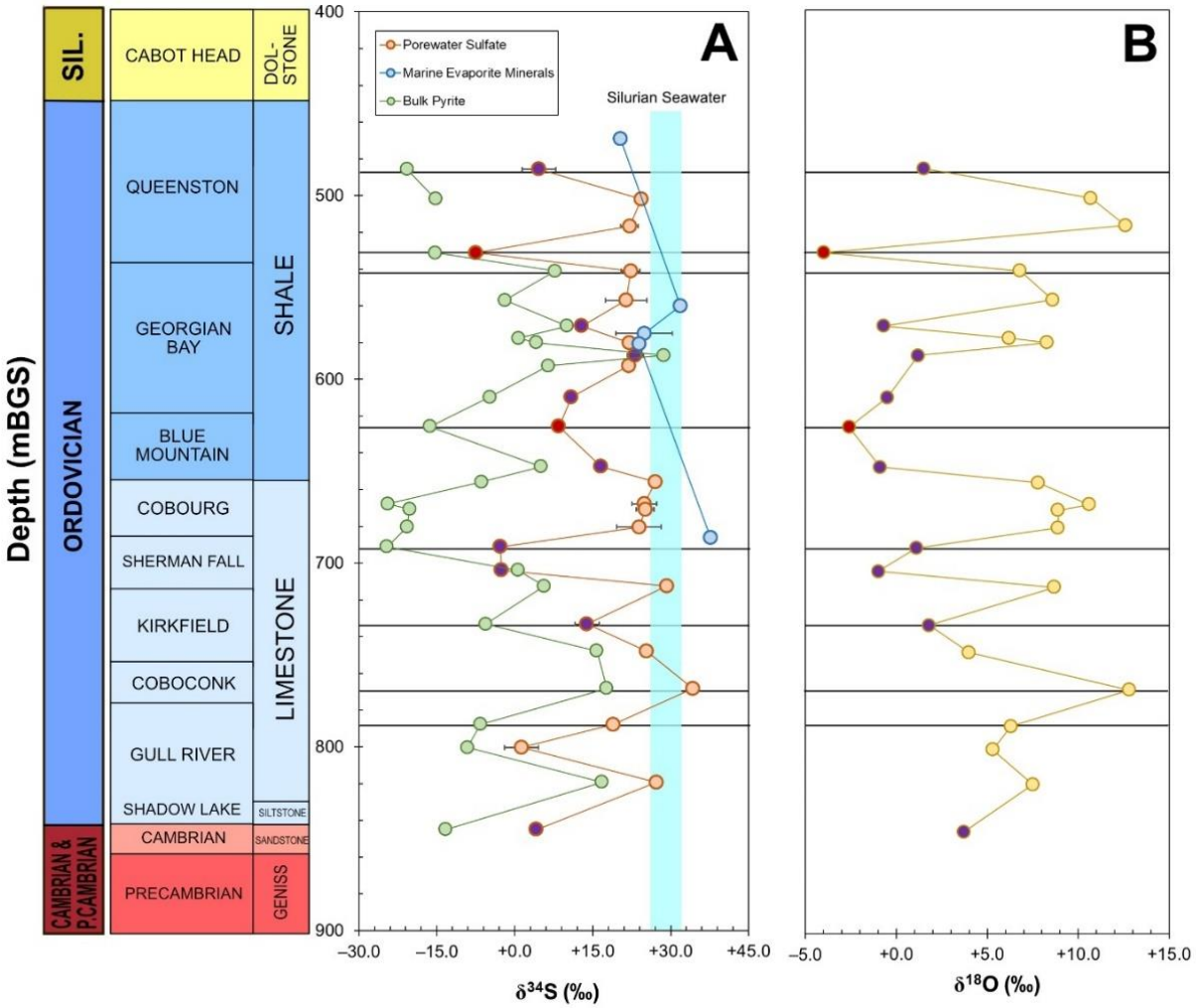

Figure 5.4. 1: $\delta^{34}S$ and $\delta^{18}O$ of porewater sulfate samples that are affected by sulfide oxidation
The samples in purple are the samples that plot within the range of sulfide oxidation in Figure 5.4 while the red samples are the two samples that plot below the sulfide oxidation range. A: presents $\delta^{34}S$ of porewater sulfate, bulk sulfide (Jautzy et al. in prep.) and marine evaporites; and B: presents the $\delta^{18}O$ of porewater sulfate.

Looking at the nine samples more closely, some of these are also within group B in Figure 5.3, suggesting that sulfide oxidation potentially occurred at these depths. This can be explained by the combination of Figure 5.3 and Figure 5.4. Seven of the nine samples (DGR-4-485.67, DGR-4-570.96, DGR-4-609.40, DGR-4-647.40, DGR-4-691.15, DGR-4-703.84 and DGR-4-733.12) fit within group B in Figure 5.3. In addition, these samples are the porewater sulfate samples with more depleted $\delta^{34}S$ and $\delta^{18}O$ signatures highlighted by the purple and red values in Figure 5.4.1. The sample DGR-4-800.42 is the only sample that has relatively depleted

$\delta^{34}S$ and $\delta^{18}O$ signatures but did not fall within the calculated sulfide oxidation range in Figure 5.4.

Examining Figure 5.3 from the previous section, although the sample DGR-4-845.00 falls within the sulfide oxidation range, it does not fall within group B in Figure 5.3 but rather, is close to the sample DGR-4-800.42. This is because the samples within the Gull River are more challenging to interpret since they are subjected to multiple fluid events that caused extensive mixing in these depths. In addition, the pyrite grains at this depth are larger while the anhydrite present at this depth is formed from secondary precipitation as a result of mixed fluids (Petts et al., 2017).

The two samples that were below the calculated range in Figure 5.4 are DGR-4-625.62 and DGR-4-531.19. This could be due to the fact that, sample DGR-4-625.62 had elevated total sulfur at this depth according to Jautzy et al. (in prep.), where high amount of pyrite would be available for sulfide oxidation. On the other hand, DGR-4-513.19 had the most depleted in both sulfur and oxygen isotopic signature. This could be due to the dominant oxidation agent being Fe (III) or if enzymatic electron shuttle transport mechanism was present on the surface of the sulfide mineral (Kelly, 1982) and all the oxygen was likely to be originated from water (Van Stempvoort and Krouse, 1994). According to Figure 4.8.3, the % wt of Fe_2O_3 is the highest at 7.09% at the depth of 535.56 mBGS while the wt% of MnO_2 is 0.087% at the depth of 535.56 mBGS. This suggests Fe (III) was most abundant and it would be the dominant oxidizing agent present at this depth.

On the other hand, the samples within Group A that plotted above the sulfide oxidation range in Figure 5.4 are likely to be samples that are overwritten by Silurian seawater isotopic signatures and are not altered by *in-situ* sulfide oxidation. These samples have $\delta^{34}S$ values

plotting just below the Silurian seawater $\delta^{34}S$ range also in Figure 5.4.1. Previous evidence revealed that these samples are not likely to be affected by sulfate mineral dissolution during leaching because they are associated with very low Ca: SO_4 ratios in Figure 5.4.2 (with the exception of DGR-4-768.13).

In summary, previous sections ruled out the possibility of unintended sulfide oxidation during experimental procedures. Thus, the oxygen isotope data of porewater sulfate and the presence of Fe (III) and Mn (IV) containing minerals suggests the possibility of *in-situ* sulfide oxidation in one third of twenty six core samples. This would have occurred at a very slow rate over hundreds of millions of years due to the low solubility of Fe_2O_3 in non-acidic conditions. In contrast, the rest of the twenty six samples (with the exception of Gull River samples) are likely to be capturing the isotopic composition of the Silurian seawater sulfate. After the evaporated Silurian seawater infiltrated the Ordovician layers, is likely that the isotopic signatures of porewater are overprinted by the Silurian seawater sulfate. The combination of sulfur and oxygen isotope shows that the porewater $\delta^{34}S_{SO4}$ values are close to the $\delta^{34}S$ range of Silurian seawater, while the porewater $\delta^{18}O_{SO4}$ values deviate from the calculated range of $\delta^{18}O_{SO4}$ due to sulfide oxidation presented in Figure 5.4.

5.8 Future improvements on porewater extraction of sulfate

To limit the dissolution of Ca-sulfate minerals during leaching is to create conditions where the solubility of these minerals is decreased. The increased salinity of *in-situ* porewater prevents mineral dissolution as high ionic strength is maintained from addition of NaCl. Thus, during porewater extraction, the leachates should mimic the salinity of the *in-situ* porewater, to maintain high ionic strength during leaching. In addition, reducing the leach time from 24 hours to 10 minutes may prove to be beneficial, as this would limit the amount of the time these

soluble minerals are exposed to water. This would also effectively reduce the overall time of sample preparation and analysis.

5.9 Implications for future research

Previous studies indicated that the Michigan Basin is currently under reduced conditions because the majority of the sulfur species present is in the form of sulfide (Raven et al., 2011). However, the oxygen isotope of sulfate in this study suggests potential sulfide oxidation that had occurred previously. Therefore, it may be important to fully understand the redox conditions within these layers by examining the various redox species that are present in these formations. This is important in terms of nuclear waste storage because oxidized conditions tend to increase the mobility of contaminants. The current state of the system is within a reduced state as majority of the sulfur species exist as pyrite and amount of oxygen is very limited within the strata.

In addition, an improved method for determining the pH, P_{O2} and P_{CO2} of porewater may prove useful as pH is an important factor for various geochemical reactions. These two factors will also prove to be useful when modeling various geochemical conditions with PHREEQC in order to understand contaminant transport. Currently, there is no proper method for measuring pH, P_{O2} and P_{CO2}.

6. Conclusions

The mass and stable isotopes of sulfate in the Ordovician strata of the Michigan Basin at the Bruce DGR site in western Ontario provided important insights into the origin and transformations of porewater sulfate, along with pyrite and sulfate mineralization, with important implications for past and current redox conditions. This study also provided a reliable method for analyzing sulfur and oxygen isotope by extracting sufficient amount of sample from rock cores

with low sulfate porewater content. Analysis of $\delta^{34}S$ and the identification of framboidal pyrite morphologies from earlier work on the Ordovician strata (Jautzy et al., in prep.) provides strong evidence for diagenetic sulfate reduction in the Ordovician shale sequences. However, no residual sulfate with diagnostic enriched $\delta^{34}S$ and $\delta^{18}O$ remains, suggesting that this original seawater sulfate was quantitatively converted to sulfide. Rather, the isotopic analysis of porewater sulfate shows to have a Silurian origin, as most of the samples have $\delta^{34}S$ signatures that are close to the Silurian $\delta^{34}S$ seawater range.

One third of the twenty-six samples showed potential evidence of sulfate contributions from *in-situ* sulfide oxidation, based on relative depletion of the seawater range for both $\delta^{34}S_{SO4}$ and $\delta^{18}O_{SO4}$ porewater sulfate. The mechanism of *in-situ* sulfide oxidation, taking place over geological time is likely proceeding with the major participation of oxygen from the porewater in the presence of Fe (III) and Mn (IV) bearing minerals within the sedimentary strata as electron acceptors. However, the exact pathway of sulfide oxidation, whether biotic or abiotic is unknown as these values cannot be differentiated according to current literature. Moreover, sulfide oxidation largely depends on a range of physicochemical conditions such as pH, temperature, the presence and absence of various oxidizing agents.

The bulk of porewater sulfate appears to be largely derived from the incursions of evaporated Silurian brine, with the evolution of this system summarized as follows:

1. During the Ordovician, framboidal pyrite was formed as a result of sulfate reduction that occurred either anoxically below the sediment water interface or within an anoxic water column. At this time, the sulfate pool reflected the isotopic composition of the Ordovician seawater.

2. In the Silurian, high evaporative rates led to the precipitation of some marine evaporite minerals as the basin was near the equator. Infiltration of evaporated and hypersaline Silurian seawater down into the Ordovician layers likely halted bacterial activity and brought in a new source of sulfate into the Ordovician strata.
3. With infiltration of the Silurian brine, some precipitation of sulfate minerals may have occurred due to the dolomitization which, released Ca^{2+} as well as, from cation exchange promoted the release of Ca^{2+} and Sr^{2+} from the sediments.
4. The more enriched porewater sulfate $\delta^{34}S$ signatures recorded by this study are likely to be a result of Silurian seawater with little to no sulfate derived from pyrite oxidation. While the more depleted porewater sulfate $\delta^{34}S$ signatures are likely from *in-situ* sulfide oxidation that may have occurred after isolation from Ordovician seawater and/or after Silurian seawater infiltration.

In order to fully understand the redox conditions within the Michigan Basin, an inventory of electron acceptor species in these formations is required, as well as their capacity for inorganic sulfate reduction. This may prove to be important in terms of predicting the mobilization of contaminants from any future nuclear waste repository under enhanced oxidizing conditions in the far field.

7. References

Activation Laboratories Ltd., 2009. TR-08-02: XRD Mineralogical Analysis of DGR-1 and DGR-2 Core. Ancaster, Ontario.

Al, T.A., Clark, I.D., Kennell, L., Jensen, M., Raven, K.G., 2015. Geochemical evolution and residence time of porewater in low-permeability rocks of the Michigan Basin, Southwest Ontario. Chemical Geology 404, 1–17.

Alonso-Azcárate, J., Rodas, M., Fernández-Díaz, L., Bottrell, S.H., Mas, J.R., López-Andrés, S., 2001. Causes of variation in crystal morphology in metamorphogenic pyrite deposits of the Cameros Basin (N Spain). Geological Journal 36, 159–170.

Antler, G., Pellerin, A., 2018. A critical look at the combined use of sulfur and oxygen isotopes to study microbial metabolisms in methane-rich environments. Frontiers in Microbiology 9, 1–7.

Antler, G., Turchyn, A. V., Herut, B., Davies, A., Rennie, V.C.F., Sivan, O., 2014. Sulfur and oxygen isotope tracing of sulfate driven anaerobic methane oxidation in estuarine sediments. Estuarine, Coastal and Shelf Science 142, 4–11.

Antler, G., Turchyn, A. V., Rennie, V., Herut, B., Sivan, O., 2013. Coupled sulfur and oxygen isotope insight into bacterial sulfate reduction in the natural environment. Geochimica et Cosmochimica Acta 118, 98–117.

Balci, N., Shanks, W.C., Mayer, B., Mandernack, K.W., 2007. Oxygen and sulfur isotope systematics of sulfate produced by bacterial and abiotic oxidation of pyrite. Geochimica et Cosmochimica Acta 71, 3796–3811.

Berner, R.A., 1969. The synthesis of framboidal pyrite. Economic Geology 64, 383–384.

Berner, R.A., 1984. Sedimentary pyrite formation: An update. Geochimica et Cosmochimica Acta 48, 605–615.

Bonev, I.K., Garcia-Ruiz, J.M., Atanassova, R., Otalora, F., Petrussenko, S., 2005. Genesis of filamentary pyrite associated with calcite crystals. European Journal of Mineralogy 17, 905–913.

Böttcher, M.E., Thamdrup, B., Vennemann, T.W., 2001. Anaerobic sulfide oxidation and stable isotope fractionation associated with bacterial sulfur disproportionation in the presence of MnO2. Geochimica et Cosmochimica Acta 65, 1573–1581.

Bottrell, S., Raiswell, R., 2000. Sulphur isotopes and microbial sulphur cycling in sediments, in: Microbial Sediments. pp. 96–104.

Brunner, B., Bernasconi, S.M., Kleikemper, J., Schroth, M.H., 2005. A model for oxygen and sulfur isotope fractionation in sulfate during bacterial sulfate reduction processes. Geochimica et Cosmochimica Acta 69, 4773–4785.

Brunner, B., Yu, J.Y., Mielke, R.E., MacAskill, J.A., Madzunkov, S., McGenity, T.J., Coleman, M., 2008. Different isotope and chemical patterns of pyrite oxidation related to lag and exponential growth phases of Acidithiobacillus ferrooxidans reveal a microbial growth strategy. Earth and Planetary Science Letters 270, 63–72.

Canfield, D.E., 2001. Biogeochemistry of Sulfur Isotopes. Reviews in Mineralogy and Geochemistry 43, 607–636.

Canfield, D.E., Teske, A., 1996. Late proterozoic rise in atmospheric oxygen concentration inferred from phylogenetic and sulphur-isotope studies. Nature 382, 127–132.

Celejewski, M., Scott, L., Al, T., 2014. An absorption method for extraction and characterization of porewater from low-permeability rocks using cellulosic sheets. Applied Geochemistry 49, 22–30.

Chambers, L.A., Trudinger, P.A., Smith, J.W., Burns, M.S., 1975. Fractionation of sulfur isotopes by continuous cultures of *Desulfovibrio desulfuricans*. Canadian Journal of Microbiology 21, 1602–1607.

Clark, I., 2015a. Water, Rocks, Solutes and Isotopes, in: Groundwater Geochemistry and Isotopes. CRC Press Taylor & Fancis Group, p. 22.

Clark, I., 2015b. Isotope Reactions, in: Groundwater Geochemistry and Isotopes. CRC Press Taylor & Fancis Group, p. 105.

Clark, I., Fritz, P., 1997a. Groundwater Quality, in: Starkweather, A.W. (Ed.), Environmental Isotopes in Hydrogeology. Lewis Publisher, New York, pp. 138–148.

Clark, I., Fritz, P., 1997b. Tracing the Carbon Cycle, in: Starkweather, A.W. (Ed.), Environmental Isotopes in Hydrogeology. Lewis Publisher, New York, pp. 112–118.

Clark, I.D., Al, T.A., Jensen, M., Kennell, L., Mazurek, M., Mohapatra, R., Raven, K.G., 2013. Paleozoic-aged brine and authigenic helium preserved in an Ordovician shale aquiclude. Geology 41, 951–954.

Clark, I.D., Ilin, D., Jackson, R.E., Jensen, M., Kennell, L., Mohammadzadeh, H., Poulain, A., Xing, Y.P., Raven, K.G., 2015. Paleozoic-aged microbial methane in an Ordovician shale and carbonate aquiclude of the michigan basin, southwestern ontario. Organic Geochemistry 83–84, 118–126.

Claypool, G.E., Holser, W.T., Kaplan, I.R., Sakai, H., Zak, I., 1980. The age curves of sulfur and oxygen isotopes in marine sulfate and their mutual interpretation. Chemical Geology 28, 199–260.

Colquhoun, I., 1991. Paragenetic History of the Ordovician Trenton Group Carbonates, Southwestern Ontario. Brock University, Canada.

Cullum, J., Stevens, D.P., Joshi, M.M., 2016. Importance of ocean salinity for climate and habitability. Proceedings of the National Academy of Sciences 113, 4278–4283.

Deusner, C., Holler, T., Arnold, G.L., Bernasconi, S.M., Formolo, M.J., Brunner, B., 2014. Sulfur and oxygen isotope fractionation during sulfate reduction coupled to anaerobic oxidation of methane is dependent on methane concentration. Earth and Planetary Science Letters 399, 61–73.

England, B.M., Ostwald, J., 1993. Framboid-derived structures in some Tasman fold belt base-metal sulphide deposits, New South Wales, Australia. Ore Geology Reviews 7, 381–412.

Fike, D.A., Bradley, A.S., Rose, C. V., 2015. Rethinking the Ancient Sulfur Cycle. Annual Review of Earth and Planetary Sciences 43, 593–622.

Fritz, P., Basharmal, G.M., Drimmie, R.J., Ibsen, J., Qureshi, R.M., 1989. Oxygen isotope exchange between sulphate and water during bacterial reduction of sulphate. Chemical Geology: Isotope Geoscience Section 79, 99–105.

Gallego-Torres, D., Reolid, M., Nieto-Moreno, V., Martínez-Casado, F.J., 2015. Pyrite framboid size distribution as a record for relative variations in sedimentation rate: An example on the Toarcian Oceanic Anoxic Event in Southiberian Palaeomargin. Sedimentary Geology 330, 59–73.

Gao, S., Huang, F., Gu, X., Chen, Z., Xing, M., Li, Y., 2017. Research on the growth orientation of pyrite grains in the colloform textures in Baiyunpu Pb–Zn polymetallic deposit, Hunan, China. Mineralogy and Petrology 111, 69–79.

Gleisner, M., Herbert, R.B., 2002. Sulfide mineral oxidation in freshly processed tailings: Batch experiments. Journal of Geochemical Exploration 76, 139–153.

Goldhaber, M.B., 2003. Sulfur-rich Sediments, in: Holland, H., Turekian, K. (Eds.), Treatise on Geochemistry. pp. 257–288.

Graham, U.M., Ohmoto, H., 1994. Experimental study of formation mechanisms of hydrothermal pyrite. Geochimica et Cosmochimica Acta 58, 2187–2202.

Habicht, K.S., Canfield, D.E., 1997. Sulfur isotope fractionation during bacterial sulfate reduction in organic-rich sediments. Geochimica et Cosmochimica Acta 61, 5351–5361.

Habicht, K.S., Canfield, D.E., 2001. Isotope fractionation by sulfate-reducing natural populations and the isotopic composition of sulfide in marine sediments. Geology 29, 555–558.

Heidel, C., Tichomirowa, M., 2010. The role of dissolved molecular oxygen in abiotic pyrite oxidation under acid pH conditions - Experiments with ^{18}O-enriched molecular oxygen. Applied Geochemistry 25, 1664–1675.

Heidel, C., Tichomirowa, M., 2011. The isotopic composition of sulfate from anaerobic and low oxygen pyrite oxidation experiments with ferric iron - New insights into oxidation mechanisms. Chemical Geology 281, 305–316.

Heidel, C., Tichomirowa, M., Junghans, M., 2009. The influence of pyrite grain size on the final oxygen isotope difference between sulphate and water in aerobic pyrite oxidation experiments. Isotopes in environmental and health studies 45, 321–342.

Hobbs, M., De Haller, A., Koroleva, M., Mazurek, M., Spangenberg, J., Mäder, U., Meier, D., 2011. TR-08-40: Borehole DGR-3 and DGR-4 Porewater Investigations.

Ilin, D., 2011. Characterization of bacterial community structure in deep subsurface sedimentary core samples from Michigan Basin, Ontario.

International Atomic Energy Agency, 1990. IAEA-TECDOC-563: Siting, Design and Construction of a Deep Geological Repository for the Disposal of High Level. Vienna.

International Atomic Energy Agency, 2009. Geological Disposal of Radioactive Waste: Technological Implications for Retrievability. IAEA Nuclear Energy Series NP-T-3, 1–57.

James, A.N., Lupton, A.R.R., 1978. Gypsum and anhydrite in foundations of hydraulic structures. Géotechnique 28, 249–272.

Jautzy, J.J., Ahad, J.M.E., Jensen, M., Clark, I.D., 2018. Molecular and isotopic evaluation of the maturation history of the organic matter in an Ordovician aquiclude (Michigan Basin): Evidence for late diagenetic biodegradation. Organic Geochemistry 125, 129–141.

Jautzy, J.J., Petts, D., Clark, I.D., Al, T.A., Stern, R.A., Jensen, M., in prep. Disentangling diagenetic evolution of an Ordovician aquiclude-- (Michigan Basin): insights from bulk and in situ S-isotope analysis of pyrite.

Jørgensen, B.B., 1978. A Theoretical Model of the Stable Sulfur Isotope Distribution in Marine sediments. Geochemistry Geophysics Geosystems 43, 363–374.

Kalliokoski, J., Cathles, L., 1969. Morphology, mode of formation, and diagenetic changes in framboids. Bulletin of the Geological Society of Finland 41, 125–133.

Kampschulte, A., Strauss, H., 2004. The sulfur isotopic evolution of Phanerozoic seawater based on the analysis of structurally substituted sulfate in carbonates. Chemical Geology 204, 255–286.

Kaplan, I.R., Rittenberg, S.C., 1964. Microbiological Fractionation of Sulphur Isotopes. Journal of General Microbiology 34, 195–212.

Kelly, D.P., 1982. Biochemistry of the chemolithotrophic oxidation of inorganic sulphur. Philosophical transactions of the Royal Society of London. Series B, Biological sciences 298, 499–528.

Kendall, C., Caldwell, E., Snyder, D., 2004. Periodic Table--Oxygen. United States Geological Survey. URL https://wwwrcamnl.wr.usgs.gov/isoig/period/o_iig.html (accessed 10.22.18).

Kendall, C., Snyder, D., 2004. Periodic Table--Sulfur. United States Geological Survey. URL https://wwwrcamnl.wr.usgs.gov/isoig/period/s_iig.html

Klimchouk, A., 1996. The Dissolution and Conversion of Gypsum and Anhydrite. International Journal of Speleology 25, 21–36.

Kohl, I., Bao, H., 2011. Triple-oxygen-isotope determination of molecular oxygen incorporation in sulfate produced during abiotic pyrite oxidation (pH=2-11). Geochimica et Cosmochimica Acta 75, 1785–1798.

Kohl, I.E., 2010. Oxidation of Reduced Sulfur Compounds: A Triple-oxygen-isotope Perspective. Louisiana State University and Agricultural and Mechanical College.

Kohn, M.J., Riciputi, L.R., Stakes, D., Orange, D.L., 1998. Sulfur isotope variability in biogenic pyrite: Reflections of heterogeneous bacterial colonization? American Mineralogist 83, 1454–1468.

Koroleva, M., Haller, A., Urs, M., Waber, H., Mazurek, M., 2009. TR-08-06: Borehole DGR-2: Porewater Investigations.

Kortenski, J., Kostova, I., 1996. Occurance and morphology of pyrite in Bulgarian coals. International Journal of Coal Geology 29, 273–290.

Krouse, H.R., Coplen, T.B., 1997. Reporting of relative sulfur isotope-ratio data (Technical Report). Pure and Applied Chemistry 69, 293–296.

Lord, C.J., Church, T.M., 1983. The geochemistry of salt marshes: Sedimentary ion diffusion, sulfate reduction, and pyritization. Geochimica et Cosmochimica Acta 47, 1381–1391.

Marenco, P.J., Corsetti, F.A., Hammond, D.E., Kaufman, A.J., Bottjer, D.J., 2008. Oxidation of pyrite during extraction of carbonate associated sulfate. Chemical Geology 247, 124–132.

Markovic, S., Paytan, A., Li, H., Wortmann, U.G., 2016. A revised seawater sulfate oxygen isotope record for the last 4Myr. Geochimica et Cosmochimica Acta 175, 239–251.

Mitterer, R.M., 2010. Methanogenesis and sulfate reduction in marine sediments: A new model. Earth and Planetary Science Letters 295, 358–366.

Moses, C.O., Herman, J.S., 1991. Pyrite oxidation at circumneutral pH. Geochimica et Cosmochimica Acta 55, 471–482.

Moses, C.O., Kirk Nordstrom, D., Herman, J.S., Mills, A.L., 1987. Aqueous pyrite oxidation by dissolved oxygen and by ferric iron. Geochimica et Cosmochimica Acta 51, 1561–1571.

Müller, I.A., Brunner, B., Breuer, C., Coleman, M., Bach, W., 2013a. The oxygen isotope equilibrium fractionation between sulfite species and water. Geochimica et Cosmochimica Acta 120, 562–581.

Müller, I.A., Brunner, B., Coleman, M., 2013b. Isotopic evidence of the pivotal role of sulfite oxidation in shaping the oxygen isotope signature of sulfate. Chemical Geology 354, 183–202.

Murowchick, J.B., Barnes, H.L., 1987. Effects of temperature and degree of supersaturation on pyrite morphology. American Mineralogist 72, 24–1250.

Murseli, S., Clark, I., St-jean, G., Mohapatra, R., Zuliani, D., Mclellan, M., Lagacé, F., 2017. DGR-8 Pore Fluid and Gas Analysis.

Nordstrom, B.D.K., Wright, W.G., Mast, M.A., Bove, D.J., Rye, R.O., 2007. Aqueous-Sulfate Stable Isotopes — A Study of Mining-Affected and Undisturbed Acidic Drainage Mining in the Animas River Watershed, San Juan County, Colorado Professional Paper 1651, in: Church, S., von Guerard, P., Finger, S. (Eds.), Integrated Investigations of Environmental Effects of Historical Mining in the Animas River Watershed, San Juan County, Colorado. U.S. Geological Survey, pp. 387–416.

Ohfuji, H., Rickard, D., 2005. Experimental syntheses of framboids - A review. Earth-Science Reviews 71, 147–170.

Oren, A., 2006. Life at High Salt Concentrations. The Prokaryotes 2, 263–282.

Oren, A., 2011. Thermodynamic limits to microbial life at high salt concentrations. Environmental Microbiology 13, 1908–1923.

Paytan, A., Mearon, S., Cobb, K., Kastner, M., 2002. Origin of marine barite deposits: Sr and S isotope characterization. Geology 30, 747–750.

Peiffer, S., Stubert, I., 1999. The oxidation of pyrite at pH 7 in the presence of reducing and nonreducing Fe(III)-chelators. Geochimica et Cosmochimica Acta 63, 3171–3182.

Pellerin, A., Anderson-Trocmé, L., Whyte, L.G., Zane, G.M., Wall, J.D., Wing, B.A., 2015. Sulfur isotope fractionation during the evolutionary adaptation of a sulfate-reducing bacterium. Applied and Environmental Microbiology 81, 2676–2689.

Petts, D.C., Saso, J.K., Diamond, L.W., Aschwanden, L., Al, T.A., Jensen, M., 2017. The source and evolution of paleofluids responsible for secondary minerals in low-permeability Ordovician limestones of the Michigan Basin. Applied Geochemistry 86, 121–137.

Pisapia, C., Chaussidon, M., Mustin, C., Humbert, B., 2007. O and S isotopic composition of dissolved and attached oxidation products of pyrite by Acidithiobacillus ferrooxidans: Comparison with abiotic oxidations. Geochimica et Cosmochimica Acta 71, 2474–2490.

Prol-Ledesma, R.M., Canet, C., Villanueva-Estrada, R.E., Ortega-Osorio, A., 2010. Morphology of pyrite in particulate matter from shallow submarine hydrothermal vents. American Mineralogist 95, 1500–1507.

Qureshi, R.M., 1986. The isotopic composition of aqueous sulfate (a laboratory investigation). University of Waterloo.

Raiswell, R., 1982. Pyrite texture, isotopic composition and the availability of iron. American Journal of Science 282, 1244–1263.

Raven, K., McCreath, D., Jackson, R., Clark, I., Heagle, D., Sterling, S., Melaney, M., 2011. Descriptive Geosphere Site Model (NWMO DGR-TR-2011-24).

Reedy, B.J., Beattie, J.K., Lowson, R.T., 1991. A vibrational spectroscopic 18O tracer study of pyrite oxidation. Geochimica et Cosmochimica Acta 55, 1609–1614.

Rees, C.E., 1973. A steady-state model for sulphur isotope fractionation in bacterial reduction processes. Geochimica et Cosmochimica Acta 37, 1141–1162.

Rickard, D.T., 1970. The origin of framboids. Lithos 3, 269–293.

Rust, G.W., 1935. Colloidal Primary Copper Ores at Cornwall Mines, Southeastern Missouri. The Journal of Geology 43, 398–426.

Sassano, G.P., Schrijver, K., 1989. Framboidal pyrite: early-diagenetic, late-diagenetic, and hydrothermal occurrences from the Acton Vale quarry, Cambro- Ordovician, Quebec. American Journal of Science 289, 167–179.

Schallreuter, R., 1984. Framboidal pyrite in deep-sea sediments. Initial Reports Deep Sea Drilling Project 530, 875–891.

Schippers, A., Jorgensen, B.B., 2001. Oxidation of pyrite and iron sulfide by manganese dioxide in marine sediments. Geochimica et Cosmochimica Acta 65, 915–922.

Schwarcz, H.P., Cortecci, G., 1974. Isotopic analyses of spring and stream water sulfate from the Italian Alps and Apennines. Chemical Geology 13, 285–294.

Shen, W., Lin, Y., Xu, L., Li, J., Wu, Y., Sun, Y., 2007. Pyrite framboids in the Permian-Triassic boundary section at Meishan, China: Evidence for dysoxic deposition. Palaeogeography, Palaeoclimatology, Palaeoecology 253, 323–331.

Slater, G.F., Moser, D.P., Sherwood Lollar, B., 2013. TR-2013-17: Development of Microbial Characterization Techniques for Low-Permeability Sedimentary Rocks.

Soliman, M.F., El Goresy, A., 2012. Framboidal and idiomorphic pyrite in the upper Maastrichtian sedimentary rocks at Gabal Oweina, Nile Valley, Egypt: Formation processes,

oxidation products and genetic implications to the origin of framboidal pyrite. Geochimica et Cosmochimica Acta 90, 195–220.

Strauss, H., 1997. The isotopic composition of sedimentary sulfur through time. Palaeogeogr. Palaeoclimatol. Palaeoecol. 132, 97–118.

Strauss, H., 2004. 4 Ga of seawater evolution: Evidence from the sulfur isotopic composition of sulfate. Geological Society of America Special Papers 379, 195–205.

Suits, N.S., Wilkin, R.T., 1998. Pyrite formation in the water column and sediments of a meromictic lake. Geology 26, 1099–1102.

Sweeney, R.E., Kaplan, I.R., 1973. Pyrite framboid formation: Laboratory synthesis and marine sediments. Economic Geology 68, 618–634.

Sweeney, R.E., Kaplan, I.R., 1980. Diagenetic sulfate reduction in marine sediments. Marine Chemistry 9, 165–174.

Taylor, B., Wheeler, M., Nordstrom, D., 1984. Stable isotope geochemistry of acid mine drainage: experimental oxidation of pyrite. Geochimica et Cosmochimica Acta 48, 2669–2678.

Thode, H.G., 1970. Sulfur Isotope Geochemistry and Fractionation Between Coexisting Sulfide Minerals. Mineral. Soc. Amer. Spec. Pap 3, 133–144.

Thode, H.G., Monster, J., 1965. Sulfur-isotope geochemistry of petroleum, evaporites, and ancient seas. Fluids in Subsurface Environments 367–377.

Thurston, R.S., Mandernack, K.W., Shanks, W.C., 2010. Laboratory chalcopyrite oxidation by Acidithiobacillus ferrooxidans: Oxygen and sulfur isotope fractionation. Chemical Geology 269, 252–261.

Tichomirowa, M., Junghans, M., 2009. Oxygen isotope evidence for sorption of molecular oxygen to pyrite surface sites and incorporation into sulfate in oxidation experiments. Applied Geochemistry 24, 2072–2092.

Toran, L., Harris, R.F., 1989. Interpretation of sulfur and oxygen isotopes in biological and abiological sulfide oxidation. Geochimica et Cosmochimica Acta 53, 2341–2348.

Turchyn, A. V., Brüchert, V., Lyons, T.W., Engel, G.S., Balci, N., Schrag, D.P., Brunner, B., 2010. Kinetic oxygen isotope effects during dissimilatory sulfate reduction: A combined theoretical and experimental approach. Geochimica et Cosmochimica Acta 74, 2011–2024.

Turchyn, A. V., Sivan, O., Schrag, D.P., 2006. Oxygen isotopic composition of sulfate in deep sea pore fluid: evidence for rapid sulfur cycling. Geobiology 4, 191–201.

Turchyn, A. V, Schrag, D.P., 2004. Oxygen isotope constraints on the sulfur cycle over the past 10 million years. Science (New York, N.Y.) 303, 2004–2007.

Tuttle, M.L., Goldhaber, M.B., 1993. Sedimentary sulfur geochemistry of the Paleogene Green River Formation, western USA: Implications for interpreting depositional and diagenetic processes in saline alkaline lakes. Geochimica et Cosmochimica Acta 57, 3023–3039.

Van Everdingen, R.O., Krouse, H.R., 1985. Isotope composition of sulphates generated by bacterial and abiological oxidation. Nature 315, 395–396.

Van Stempvoort, D.., Krouse, H.., 1994. Controls of $\delta^{18}O$ in sulfate: Review of Experimental Data and Application to Specific Environments. Environmental Geochemistry of Sulfide Oxidation 550, 446–480.

Vanwonterghem, I., Evans, P.N., Parks, D.H., Jensen, P.D., Woodcroft, B.J., Hugenholtz, P., Tyson, G.W., 2016. Methylotrophic methanogenesis discovered in the archaeal phylum Verstraetearchaeota. Nature Microbiology 1, 1–9.

Veizer, J., Bruckschen, P., Pawellek, F., Diener, A., Podlaha, O.G., Carden, G.A.F., Jasper, T., Korte, C., Strauss, H., Azmy, K., Ala, D., 1997. Oxygen isotope evolution of Phanerozoic seawater. Palaeogeography, Palaeoclimatology, Palaeoecology 132, 159–172.

Wang, Q., Morse, J.W., 1996. Pyrite formation under conditions approximating those in anoxic sediments: I. Pathway and morphology. Marine Chemistry 52, 99–121.

Whiticar, M.J., 1999. Carbon and hydrogen isotope systematics of bacterial formation and oxidation of methane. Chemical Geology 161, 291–314.

Whitney, C., Lee, R., 2010. Laboratory Petrophysical Testing of DGR-2 Core, Quality. Houston, Texas.

Wilkin, R.T., Barnes, H.L., 1997. Formation processes of framboidal pyrite. Geochimica et Cosmochimica Acta 61, 323–339.

Wilkin, R.T., Barnes, H.L., Brantley, S.L., 1996. The size distribution of framboidal pyrite in modern sediments: An indicator of redox conditions. Geochimica et Cosmochimica Acta 60, 3897–3912.

Wortmann, U.G., Bernasconi, S.M., Böttcher, M.E., 2001. Hypersulfidic deep biosphere indicates extreme sulfur isotope fractionation during single-step microbial sulfate reduction. Geology 29, 647–650.

Wortmann, U.G., Chernyavsky, B., Bernasconi, S.M., Brunner, B., Böttcher, M.E., Swart, P.K., 2007. Oxygen isotope biogeochemistry of pore water sulfate in the deep biosphere: Dominance of isotope exchange reactions with ambient water during microbial sulfate reduction (ODP Site 1130). Geochimica et Cosmochimica Acta 71, 4221–4232.

Wotte, T., Shields-Zhou, G.A., Strauss, H., 2012. Carbonate-associated sulfate: Experimental comparisons of common extraction methods and recommendations toward a standard analytical protocol. Chemical Geology 326–327, 132–144.

Wu, N., Farquhar, J., Strauss, H., 2014. $\delta^{34}S$ and $\delta^{33}S$ records of Paleozoic seawater sulfate based on the analysis of carbonate associated sulfate. Earth and Planetary Science Letters 399, 44–51.

Zhang, M., Konishi, H., Xu, H., Sun, X., Lu, H., Wu, D., Wu, N., 2014. Morphology and formation mechanism of pyrite induced by the anaerobic oxidation of methane from the continental slope of the NE South China Sea. Journal of Asian Earth Sciences 92, 293–301.